Exploring the strangeness enhancement and collectivity in pp and Pb-Pb collisions at the LHC using event shape engineering

A THESIS

Submitted in partial fulfilment of the requirements

for the award of the degree

of

DOCTOR OF PHILOSOPHY

by

Suraj Prasad

DEPARTMENT OF PHYSICS

INDIAN INSTITUTE OF TECHNOLOGY INDORE

July 2025

INDIAN INSTITUTE OF TECHNOLOGY INDORE

I hereby certify that the work which is being presented in the thesis entitled **Exploring the strangeness enhancement and collectivity in pp and Pb-Pb collisions at the LHC using event shape engineering** in the partial fulfillment of the requirements for the award of the degree of **DOCTOR OF PHILOSOPHY** and submitted in the **DEPARTMENT OF PHYSICS, Indian Institute of Technology Indore**, is an authentic record of my own work carried out during the time period from August 2020 to July 2025 under the supervision of Prof. Raghunath Sahoo, Professor, Department of Physics, Indian Institute of Technology Indore.

The matter presented in this thesis has not been submitted by me for the award of any other degree of this or any other institute.

Suraj Prasad 06/10/2025

Signature of the student

(Suraj Prasad)

This is to certify that the above statement made by the candidate is correct to the best of my knowledge.

Sahoo 06.10.25

Signature of Thesis Supervisor

(Prof. Raghunath Sahoo)

Mr. Suraj Prasad has successfully given his Ph.D. Oral Examination held on ...06 october 2025

Sahoo 06.10.25

Signature of Thesis Supervisor

(Prof. Raghunath Sahoo)

To my parents:

Thank you for the love and support,
this thesis is dedicated to you.

ACKNOWLEDGEMENTS

This thesis would not have been possible without the support and blessings of many people who have been part of my life. The work presented here is the outcome of their good wishes, love, and guidance, which motivated me to overcome every obstacle along the way. Although I have tried my best to recall everyone who played a role in this journey, I humbly beg forgiveness if I have failed to acknowledge anyone. I am truly thankful to all who have contributed in any way.

First and foremost, I express my heartfelt gratitude to my thesis supervisor, Prof. Raghunath Sahoo, for his invaluable guidance and unwavering support throughout my PhD journey. He has been the paragon of patience, dedication, and steady mentorship, consistently offering both academic and personal guidance whenever needed. His insights, and constructive criticisms have been instrumental in shaping this thesis. I deeply appreciate his willingness to engage in physics discussions, even during holidays and late hours, which greatly enriched my understanding and motivation. He not only provided the necessary resources and opportunities for my research, but also created an environment that encouraged independent thinking. His unique balance of friendliness and firmness has helped me grow both as a researcher and an individual. No words can truly capture the depth of my appreciation for him. I feel fortunate and grateful to have him as my supervisor.

I feel privileged to have participated in one of the largest collider experiments, ALICE at the Large Hadron Collider, the most powerful accelerator on Earth. I sincerely thank DST, DAE, Government of India, and IIT Indore for providing me the platform to contribute to the experimental analysis and data-taking operations at CERN. I express my sincere gratitude to the conveners of the Strangeness Physics Analysis Group (PAG-Strangeness), Dr. Chiara De Martin and Dr. Francesca Ercolessi, and the conveners of the Light Flavour Physics Working Group (PWG-LF), Dr. Nicolo Jacazio and Dr. Sourav Kundu, for their suggestions and constructive comments that shaped my analysis. I also appreciate the helpful discussions with Dr. Antonio Ortiz, Dr. Arvind Khuntia, Dr. Omar Vázquez Rueda, and Dr. Gyula Bencedi, and thank Dr. Sushanta Tripathy and Dr. Antonio Ortiz for their comments on my analysis note.

I extend my heartfelt gratitude to Prof. Gergely Gábor Barnaföldi for inviting me mul-

tiple times to the HUN-REN Wigner Research Center for Physics, Budapest, Hungary, and giving me the opportunity to work with him. His guidance and input during physics discussions were highly valuable, and his support made my stay in Budapest enjoyable and productive. I gratefully acknowledge the MoU between Wigner RCP and IIT Indore, which facilitated these research visits. I also acknowledge the use of computational resources provided by the HUN-REN Wigner Scientific Computing Laboratory (WSCLAB). Special thanks to Dr. Neelkamal Mallick for his help and guidance during my first visit.

I thank my PSPC members, Dr. Manavendra Mahato and Prof. Vipul Singh, for their guidance and valuable suggestions on my research. I also extend my thanks to all the esteemed faculty members of the Department of Physics, IIT Indore. I am grateful to Mr. Vedprakash, Mr. Prashant, Mr. Rahul, and Mr. Sunny for managing administrative tasks at IIT Indore, which helped ease many challenges during my PhD. I gratefully acknowledge the doctoral fellowship from the University Grants Commission (UGC), Government of India, for supporting my research.

I feel fortunate to have worked closely with Prof. Raghunath Sahoo, Prof. Gergely Gábor Barnaföldi, and Prof. Gagan B. Mohanty. I also thank my collaborators: Dr. Sushanta Tripathy, Dr. Neelkamal Mallick, Dr. Arvind Khuntia, Dr. Aditya Nath Mishra, Aswathy Menon K. R., Bhagyarathi Sahoo, Debadatta Behera, Kangkan Goswami, Sarthak Tripathy, Dr. Antonio Ortiz, Dr. Omar Vázquez Rueda, Dr. Gyula Bencedi, and Dr. Feng Fan, from whom I have learned a great deal. I appreciate insightful physics discussions with Prof. Tapan Nayak and Prof. Anju Bhasin.

A special thanks to Neelkamal Bhai, Sushanta Bhai, Dushmanta Bhai, and Captain Bhaiya for their mentorship and support during my early days in the PhD program. I am deeply grateful to all my labmates—Rutuparna Didi, Suman Bhaiya, Captain Bhaiya, Dushmanta Bhai, Neelkamal Bhai, Girija Bhai, Jayanta Bhaiya, Ronald, Debadatta, Kshitish, Kamaljeet, Bhagyarathi, Aswathy, Kangkan, Purnima, Parul, Jeevan, Bhavin, Ben, Kanaka, Preet, Subham, Sarthak, and Rishabhs (Tiwari and Gupta)—who made these last five years enjoyable and memorable. The presence of Neelkamal Bhai and Sushanta Bhai in my life has been invaluable. I am forever indebted to them for their constant support and kindness.

A special thanks to Hemanta Giri Sir for his teaching, continuous inspiration, and for

showing me the path to higher education. I shall always remain grateful for his presence in my life. I would also like to thank Dr. Surya Nayak for his excellent teaching, without which I would not have been able to grasp the foundations of high energy particle physics.

This journey would not have been possible without the love and sacrifices of my beloved parents and siblings, whose support cannot be described in simple words. A heartfelt mention to my dear friends—Pilu, Silu, Debashish, Bitu, Pratima, Gajendra, Pritam, Pruthivi, and Divya—for always being there for me.

This thesis and PhD journey have been made meaningful and possible by the presence of all these individuals. I am forever thankful to them.

(Suraj Prasad)

ABSTRACT

Quark-Gluon Plasma (QGP) is a deconfined and thermalised medium of partons (quarks and gluons), which is believed to have formed in ultra-relativistic collisions at the Large Hadron Collider (LHC), CERN and Relativistic Heavy-Ion Collider (RHIC), BNL. QGP is transient in nature, having a lifetime of the order 10^{-23} seconds, which makes its direct observation nearly impossible. However, there are signatures that signify the formation of the QGP phase in heavy-ion collisions. These signatures include the enhanced production of strange hadrons, collectivity, jet quenching, quarkonia supression, thermal photon and dilepton production, etc. A few of these studies require proton-proton (pp) collisions as the baseline measurements where the formation of a QGP medium is usually not anticipated. However, high multiplicity pp collisions at the LHC show observations of nonzero elliptic flow coefficient, characteristic modifications of baryon to meson ratios, enhanced production of strange and multi-strange hadrons, etc., which are believed to be achievable in ultra-relativistic nuclear collisions. This indicates that a common underlying physics mechanism drives these observations throughout the collision systems. However, other signatures, such as quarkonia suppression, jet quenching, etc., are not observed in small collision systems. The Monte Carlo (MC) based event generators are thus unable to explain all the experimentally observed QGP signatures in small systems, which questions the existence of a QGP medium in small collision systems, and the true microscopic origin of these observed heavy-ion-like features is still unclear.

The perturbative quantum chromodynamics (p-QCD) based models such as PYTHIA8 with the implementation of multi-partonic interactions (MPI), color reconnection (CR) and rope hadronization (RH) is capable of explaining strangeness enhancement and radial-flow phenomena observed in pp collisions in LHC experiments. However, MPI can not be measured in experiments, and thus, often, the experimental measurements in pp collisions are performed as a function of charged particle multiplicity. The charged particle multiplicity has a strong correlation with the number of MPI (N_{mpi}). However, studies show that the measurements as a function of charged particle multiplicity are significantly biased and possess contributions from multi-jet topologies. Thus, it is important to find event shape classifiers that are sensitive to the intrinsic number of MPI (N_{mpi}) and can effectively separate events that possess contributions from multiple-jet topologies. Event

shape observables, such as transverse spherocity (S_0), transverse sphericity ($S_{\rm T}$), relative transverse activity classifier ($R_{\rm T}$), charged particle flattenicity ($\rho_{\rm ch}$), etc., are sensitive to $N_{\rm mpi}$ and are able to separate soft-QCD dominated isotropic events from the hard-QCD dominated jetty events. However, every event shape observable is intrinsically different, and thus, its usefulness may differ from one study to another. Part of this thesis focuses on exploring the production of strange and multi-strange hadrons as a function of different event classifiers. We study strange and multi-strange hadron production to pion ratio, and their self normalised yields with event selections based on different event shape classifiers. The study is performed using different tunes of PYTHIA8 including Color Ropes, Monash and Monash NoCR. The event classifiers based on multiplicity possess significant selection bias. Additionally, $S_{\rm T}$, S_0 and $S_0^{p_{\rm T}=1}$ possesses small correlation bias and thus unable to explain experimentally observed strangeness enhancement feature. The studies of strangeness enhancement using charged particle flattenicity are closest to that of $N_{\rm mpi}$ selections, which emphasizes its applicability for further studies in both theoretical and experimental fronts.

Moreover, the thesis extends the studies to study the neutral strange hadrons, such as $K^0_{\rm S}$ and $\Lambda + \bar{\Lambda}$ as a function of charged particle flattenicity in pp collisions at $\sqrt{s} = 13.6$ TeV with A Large Ion Collider Experiment (ALICE) with LHC Run3 data. The thesis follows the flattenicity dependent study of transverse momentum spectra of $K^0_{\rm S}$ and $\Lambda+\bar{\Lambda}$, their ratios and the ratio with respect to minimum bias. This study concludes that the radial flow like signals are enhanced for events with large values of $1-\rho$ (isotropic events). Moreover the isotropic event selection using charged particle flattenicity are not affected by auto-correlation biases and multi-jet topologies.

The event shape observables are not only used in small systems like pp collisions but have several applications in heavy-ion collisions. Specifically, in the measurements of anisotropic flow coefficients (v_n), which are the Fourier expansion coefficients of azimuthal distribution of particles in the final state and is related to the initial geometry of collision overlap region. Due to fluctuating geometry of the colliding nuclei, the collision overlap region fluctuates event-by-event which leads to fluctuations of measured anisotropic flow coefficients. Event shape observables are excellent tools that can be useful in making event classifications to reduce the event-by-event fluctuations of anisotropic flow coeffi-

cients. Traditionally, event classifiers, such as the reduced flow vectors, have been used to make such event classifications in heavy-ion collisions. However, they are limited by their applicability in events with large multiplicity, and the accuracy decreases as one moves towards the peripheral or low multiplicity events. To overcome the shortcomings of reduced flow vectors, transverse spherocity can be used, which is backed by its excellent capability to make event classifications even in small multiplicity environments. The second part of the thesis discusses the applicability of transverse spherocity to study anisotropic flow coefficients. Here, the thesis presents the study of initial eccentricities, final state anisotropic flow coefficients, their fluctuations, the interplay among them and the kinetic freezeout parameters including the average transverse radial flow velocity and kinetic freeze-out temperature in Pb-Pb collisions $\sqrt{s_{\rm NN}} = 5.02$ TeV using AMPT. This study establishes unique ways to reduce the contributions of elliptic flow from higher order harmonics and comments on system response to geometry versus fluctuation dominated events.

ACRONYMS

- **ACORDE** – ALICE Cosmic Rays Detector
- **ALICE** – A Large Ion Collider Experiment
- **AMPT** – A Multi-Phase Transport model
- **AMPT-SM** – AMPT String Melting version
- **AO2D** – Analysis Oriented O^2 Data
- **AOD** – Analysis Oriented Data
- **ART** – A Relativistic Transport model
- **ATLAS** – A Toroidal LHC Apparatus
- **BGBW** – Boltzmann-Gibbs Blast-Wave
- **CMS** – Compact Muon Solenoid
- **CR, CR0, CR1, CR2** – Color Reconnection models
- **EMCAL** – Electromagnetic Calorimeter
- **FDD** – Forward Diffractive Detector
- **FIT** – Fast Interaction Trigger
- **FT0** – Forward Time Zero detectors
- **FV0** – Forward VZERO Detector
- **GEM** – Gas Electron Multiplier
- **HIJING** – Heavy-Ion Jet INteraction Generator
- **HMPID** – High Momentum Particle Identification Detector
- **IB / OB** – Inner Barrel / Outer Barrel (of ITS)

- **ITS / ITS2** – Inner Tracking System / Upgraded ITS
- **LHC** – Large Hadron Collider
- **LEIR** – Low Energy Ion Ring
- **LINAC2 / LINAC3** – Linear Accelerators
- **MC** – Monte Carlo
- **MCH** – Muon Tracking Chambers
- **MID** – Muon Identifier
- **MFT** – Muon Forward Tracker
- **MONARC** – Models Of Network Analysis at Regional Centers
- **MPI** – Multi-Partonic Interactions
- N_{mpi} – Number of multi-partonic interactions
- $N_{\mathrm{ch}}^{\mathrm{fwd}}$ – Number of charged particles in the forward rapidity region
- $N_{\mathrm{ch}}^{\mathrm{mid}}$ – Number of charged particles in the mid-rapidity region
- **O2** – ALICE Online Offline computing framework
- **PHENIX** – Pioneering High Energy Nuclear Interaction eXperiment
- **PHOS** – Photon Spectrometer
- **PID** – Particle Identification
- **PS** – Proton Synchrotron
- **QGP** – Quark-Gluon Plasma
- **QCD** – Quantum Chromodynamics
- **RH** – Rope Hadronisation
- **ROOT** – CERN's data analysis framework

- **RHIC** – Relativistic Heavy-Ion Collider
- R_{T} – Relative transverse activity classifier
- **SPS** – Super Proton Synchrotron
- **STAR** – Solenoidal Tracker at RHIC
- S_{T} – Transverse sphericity
- S_0 – p_{T}-weighted transverse spherocity
- $S_0^{p_{\mathrm{T}}=1}$ – Unweighted transverse spherocity
- **TeV** – Tera Electron Volt
- **TPC** – Time Projection Chamber
- **TOF** – Time Of Flight detector
- **TRD** – Transition Radiation Detector
- **UE** – Underlying Event
- **V0** – V Zero detector
- **V0M** – Charged particle multiplicity in the V0 region
- **WLCG** – Worldwide LHC Computing Grid
- **ZDC** – Zero Degree Calorimeter
- ρ_{ch} **or** ρ – Charged particle flattenicity measured in ALICE V0 or FV0 region

PUBLICATIONS

- **Publications included in the Ph.D. thesis**

A. Published Articles

1. **S. Prasad**, N. Mallick, D. Behera, R. Sahoo and S. Tripathy, "Event topology and global observables in heavy-ion collisions at the Large Hadron Collider", Sci. Rep. 12, 3917 (2022).
2. **S. Prasad**, N. Mallick, S. Tripathy, and R. Sahoo, "Probing initial geometrical anisotropy and final azimuthal anisotropy in heavy-ion collisions at Large Hadron Collider energies through event-shape engineering", Phys. Rev. D 107, 074011 (2023).
3. **S. Prasad**, N. Mallick and R. Sahoo, "Inclusive, prompt and nonprompt J/ψ identification in proton-proton collisions at the Large Hadron Collider using machine learning", Phys. Rev. D 109, 014005 (2024).
4. **S. Prasad**, B. Sahoo, S. Tripathy, N. Mallick, and R. Sahoo, "Probing strangeness with event topology classifiers in pp collisions at energies available at the CERN Large Hadron Collider with the rope hadronization mechanism in PYTHIA", Phys. Rev. C 111, 044902 (2025).
5. **S. Prasad**, A. Menon. K. R, R. Sahoo, and N. Mallick, "Higher order flow coefficients – A Messenger of QCD medium formed in heavy-ion collisions at the Large Hadron Collider", Phys. Lett. B 868, 139753 (2025).

B. Other

1. **S. Prasad** and R. Sahoo, "Production of K^0_S and $\Lambda + \bar{\Lambda}$ as a function of charged particle flattenicity in proton-proton collisions at $\sqrt{s} = 13.6$ TeV with ALICE." Analysis Note ID number: ANA-1609 (ALICE Internal).

C. Conference Proceedings

1. S. Tripathy, **S. Prasad**, N. Mallick, B. Sahoo, R. Sahoo, "A review on event shape studies in ultra-relativistic collisions at the LHC energies", DAE Symp. Nucl. Phys. 67, 1135 (2024).

2. **S. Prasad**, N. Mallick, S. Tripathy, R. Sahoo, "Studying the dependence of transverse spherocity on the initial and final state anisotropies in heavy-ion collisions", DAE Symp. Nucl. Phys. 67, 1133 (2024).

3. **S. Prasad**, N. Mallick, R. Sahoo, "Segregating the topological productions of J/ψ at the Large Hadron Collider using machine learning", DAE Symp. Nucl. Phys. 67, 989 (2024).

4. **S. Prasad**, N. Mallick, D. Behera, R. Sahoo and S. Tripathy, "Transverse spherocity dependence of the global observables in heavy-ion collisions at the LHC", DAE Symp. Nucl. Phys. 66, 1016 (2023).

5. **S. Prasad**, B. Sahoo, S. Tripathy, N. Mallick and R. Sahoo, "Exploring strangeness enhancement in proton-proton collisions at the LHC with event shapes," DAE Symp. Nucl. Phys. 68, 987 (2025).

6. **S. Prasad**, N. Mallick, S. Tripathy, R. Sahoo, "A Study on Transverse Spherocity Dependent Initial and Final State Anisotropies in Heavy-ion Collisions", Springer Proc. Phys. 304, 731 (2024).

7. **S. Prasad**, N. Mallick, D. Behera, R. Sahoo, S. Tripathy, "Transverse spherocity dependence of global observables in heavy-ion collisions at the LHC using AMPT model", PoS LHCP2022, 331 (2023).

8. **S. Prasad**, N. Mallick, S. Tripathy, D. Behera, and R. Sahoo , "Event topology in heavy-ion collisions: The initial spatial anisotropy and final azimuthal anisotropy", J. Subatomic Part. Cosmol. 4, 100110 (2025).

• Other outcomes outside of the Ph.D. thesis work

A. Published Articles

1. D. Behera, N. Mallick, S. Tripathy, **S. Prasad**, A. N. Mishra and R. Sahoo, "Predictions on global properties in O+O collisions at the Large Hadron Collider using a multi-phase transport model", Eur. Phys. J. A 58, 175 (2022).
2. N. Mallick, **S. Prasad**, A. N. Mishra, R. Sahoo, and G. G. Barnafoldi, "Estimating elliptic flow coefficient in heavy ion collisions using deep learning", Phys. Rev. D 105, 114022 (2022).
3. D Behera, **S Prasad**, N Mallick and R Sahoo, "Effects of clustered nuclear geometry on the anisotropic flow in O-O collisions at the LHC within a multi-phase transport model framework", Phys. Rev. D 108, 054022 (2023).
4. N. Mallick, **S. Prasad**, A. N. Mishra, R. Sahoo, and G. G. Barnafoldi, "Deep learning predicted elliptic flow of identified particles in heavy-ion collisions at the RHIC and LHC energies", Phys. Rev. D 107, 094001 (2023).
5. A. Menon K R, **S. Prasad**, S. Tripathy, N. Mallick and R. Sahoo, "Investigating radial-flow-like effects via pseudorapidity and transverse spherocity dependence of particle production in pp collisions at the LHC", Eur. Phys. J. Plus 140, 110 (2025).
6. K. Goswami, **S. Prasad**, N. Mallick, R. Sahoo, and G. B. Mohanty, "A machine learning-based study of open-charm hadrons in proton-proton collisions at the Large Hadron Collider , Phys. Rev. D 110, 034017 (2024).
7. A. Menon KR, **S. Prasad**, N. Mallick, and R. Sahoo, "Role of clustered nuclear geometry in particle production through p-C and p-O collisions at the Large Hadron Collider", Eur. Phys. J. A 61, 134 (2025).
8. A. Ortiz, A. Khuntia, O. Vázquez-Rueda, S. Tripathy, G. Bencedi, **S. Prasad** and F. Fan, "Unveiling the effects of multiple soft partonic interactions in pp collisions at $\sqrt{s} = 13$ TeV using a new event classifier", Phys. Rev. D 107, 076012 (2023).
9. **S. Prasad**, N. Mallick, R. Sahoo, and B. B. Barnafoldi, "Anisotropic flow fluctuation as a possible signature of clustered nuclear geometry in O-O collisions at the Large Hadron Collider", Phys. Lett. B 860, 139145 (2025).

B. Communicated Articles

1. S. Tripathy, **S. Prasad**, and R. Sahoo, "Event shape dependence of symmetry plane correlations using the Gaussian estimator in Pb-Pb collisions at the LHC using AMPT", arXiv:2504.09275.

2. A. Menon. KR, **S. Prasad**, N. Mallick, R. Sahoo, and G. G. Barnaföldi, "Probing nuclear structure in relativistic p-O and O-O collisions at the LHC through the measurement of anisotropic flow coefficients", arXiv:2505.22367.

3. **S. Prasad**, S. Tripathy, B. Sahoo, and R. Sahoo, "Event Topology Classifiers at the Large Hadron Collider", arXiv:2506.03782.

4. R. Sahoo, K. Goswami, and **S. Prasad**, "Machine learning driven identification of heavy flavor decay leptons in proton-proton collisions at the Large Hadron Collider", arXiv:2509.00712.

C. Conference Proceedings

1. A. Menon K. R, **S. Prasad**, N. Mallick, S. Tripathy, R. Sahoo, "Pseudorapidity and transverse spherocity dependence of particle production in proton+proton collisions at the LHC", DAE Symp. Nucl. Phys. 67, 1029 (2024).

2. D. Behera, **S. Prasad**, N. Mallick, R. Sahoo, "Effects of α-cluster geometry on the azimuthal anisotropy in O-O collisions at the LHC", DAE Symp. Nucl. Phys. 67, 1043 (2024).

3. N. Mallick, **S. Prasad**, A. N. Mishra, R. Sahoo, G. G. Barnafoldi, "A machine learning approach in estimating the coefficient of azimuthal anisotropy in heavy-ion collisions", DAE Symp. Nucl. Phys. 67, 1091 (2024).

4. D. Behera, N. Mallick, S. Tripathy, **S. Prasad**, A. N. Mishra and R. Sahoo, "Global properties in O+O collisions at $\sqrt{s_{\rm NN}} = 7$ TeV using a multi-phase transport model", DAE Symp. Nucl. Phys. 65, 718 (2022).

5. S. K. Das, et al., "Dynamics of Hot QCD Matter — Current Status and Developments", Int. J. Mod. Phys. E 31, 12 (2022).

6. A. Menon. K. R, **S. Prasad**, N. Mallick and R. Sahoo, "Exploring the medium anisotropy in p–O and p–C collisions at the LHC energy with exotic α- clusters," DAE Symp. Nucl. Phys. 68, 977 (2025).

7. K. Goswami, **S. Prasad**, N. Mallick, R. Sahoo and G. B. Mohanty, "A study of open-charmed hadrons in p-p collisions using machine learning methods," DAE Symp. Nucl. Phys. 68, 945 (2025).

8. D. Behera, N. Mallick, S. Tripathy, **S. Prasad**, A. N. Mishra, "Sensitivity of Nuclear Density Profiles on Global Observables in O-O Collisions at the Large Hadron Collider Using AMPT Model", Springer Proc. Phys. 304, 925 (2024).

9. G. G. Barnafoldi, N. Mallick, **S. Prasad**, R. Sahoo and A. N. Mishra, "A Deep Learning Based Estimator for Light Flavour Elliptic Flow in Heavy Ion Collisions at LHC Energies," EPJ Web Conf. 316, 03004 (2025).

10. N. Mallick, **S. Prasad**, A. N. Mishra, R. Sahoo, G. G. Barnafoldi, "A Deep Learning Based Estimator for Elliptic Flow in heavy-ion Collisions", PoS LHCP2022, 259 (2023).

11. D. Behera, N. Mallick, S. Tripathy, **S. Prasad**, A. N. Mishra and R. Sahoo, "Global properties in O+O collisions at $\sqrt{s_{NN}} = 7$ TeV using AMPT model", PoS LHCP2022, 305 (2023).

12. R. Sahoo, **S. Prasad**, N. Mallick, K. Goswami and G. B. Mohanty, "Prompt and non-prompt production of charm hadrons in proton–proton collisions at the Large Hadron Collider using machine learning," J. Subatomic Part. Cosmol. 4, 100085 (2025).

13. **S. Prasad**, N. Mallick, R. Sahoo and G. G. Barnafoldi, "Exploring the effects of α-clustered structure of ^{16}O nuclei in anisotropic flow fluctuations in ^{16}O-^{16}O collisions at the LHC within a CGC+Hydro framework," arXiv:2504.10544.

Contents

Figures

Tables

Chapter 1

Introduction

What is the universe made of? How does it work? How did it come into existence? These are a few of the fundamental questions that lie at the bottom of human curiosity and drive the journey of scientific explorations. Specifically, the question "How does the universe work?" is the backbone that has navigated the physics research from Newtonian mechanics to quantum field theory to date. Starting from the discovery of gravity, to the so-called God particle, the Higgs boson, the research in physics has made innovations that have led to the present world full of engineering marvels. The theory of the Big Bang is one of the most accepted theories, which states that the universe started with an infinitely dense state of matter, which evolved through its different states to the present-day universe. A few microseconds after the Big Bang, a state of deconfined partons existed called the Quark Gluon Plasma (QGP). Interestingly, the theory of strong interaction, quantum chromodynamics (QCD), also predicts a similar state of matter. In this chapter, I shall discuss the necessary ingredients to understand QGP. The discussions will be followed by QGP in small systems, their signatures, and an introduction to different event-shape observables, which are important for studying QGP in small systems.

1.1 History of particle physics

In our daily life, we deal with solid, liquid or gaseous states of matter, which are thought to be made up of tiny particles known as atoms. The name 'atom' derives from the Greek word 'atomos', which means 'uncuttable' or 'indivisible' the idea of which is more

philosophically oriented than scientifically proven. In modern days, we know that an atom consists of a nucleus and electrons. The era of particle physics is believed to have started with the discovery of electrons in 1897 by J. J. Thomson during the cathode-ray tube experiment. Further, the famous gold foil experiment by Ernest Rutherford led to the discovery of an atomic nucleus consisting of electrically charged protons and neutral neutrons. Until the late 1960s, the major discoveries in particle physics were possible through cosmic rays, which were the only source of high-energy interactions then available. The discovery of a new number of elementary particles through cosmic rays stimulated the development of particle accelerators, providing an intense and controlled beam of particles with known energies. Finally, in the late 1960s, the Stanford Linear Accelerator Center (SLAC) experiments demonstrated the proton's substructure through deep inelastic scattering [1, 2]. This led to the discovery of quarks, a fundamental particle that is a constituent of all hadrons, and put the subject on a sound quantitative basis.

1.2 Standard Model of Particle Physics

With the advent of a number of fundamental particles, a theory was necessary to describe the interactions among them. The standard model of particle physics is one such theory that describes three of the four known fundamental interactions, namely, the electromagnetic interaction, the weak interaction and the strong interaction. The standard model of particle physics has $SU(3)_C \times SU(2)_L \times U(1)_Y$ Gauge symmetry. Here, the subscripts C, L and Y stand for color, left-handed and hypercharge, respectively. A simple depiction of the involved particles and their various quantum numbers in the Standard Model is shown in Fig. 1.1. The Standard Model incorporates twelve fermions, their antiparticles and five bosons. The fermion sector includes three generations of quarks and three generations of leptons. The leptons are divided into electrons (e), muons (μ), and tauon (τ) having unit negative charge along with corresponding neutrinos, such as ν_e, ν_μ and ν_τ. These neutrinos are chargeless, massless and are left-handed in the standard model. Similarly, the anti-neutrinos are right-handed. The quarks are up (u), down (d), charm (c), strange (s), top (t) and bottom (b). The quarks have fractional electric charge where the quarks

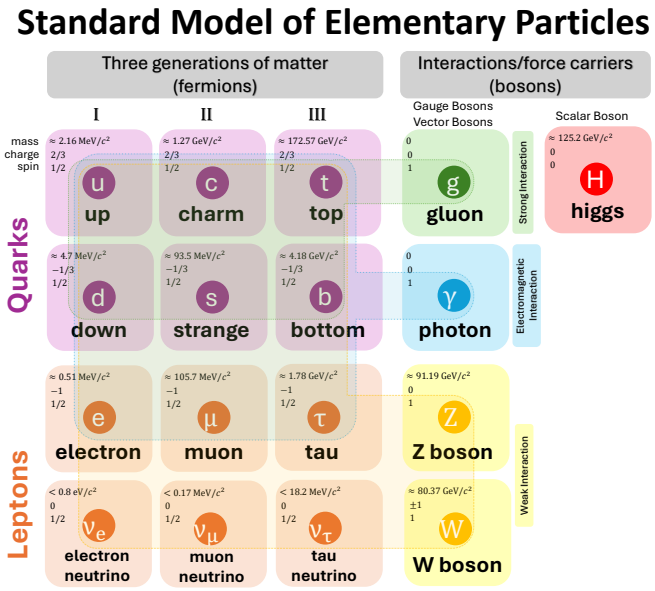

Figure 1.1: Representation of the Standard Model of elementary particles with corresponding quantum numbers.

u, c, t have the charge 2/3 times that of a positron [1] and d, s and b quarks have 1/3 times the charge of an electron. The quarks can possess one of the three color charges such, as red ($r = +1$), blue ($b = +1$) and green ($g = +1$) [2]. Similarly, the anti-quarks possess negative color charges, $r = -1$, $b = -1$, and $g = -1$. The vector gauge bosons, such as $W^{\pm}$ and Z, are mediators for the weak interaction. Photons (γ) are the mediators for the electromagnetic interaction. Finally, eight kinds of gluons are the mediators for the strong interactions [3]. Unlike photons, which are chargeless in electromagnetic interactions, the gluons are color-charged particles capable of self-interactions. This makes the study of strong interaction interesting, which is well understood by the theory of strong interaction given by QCD.

[1] Positrons are anti-particles of electrons having unit positive charge.

[2] These color charges are quantum numbers and have nothing to do with the actual colors of the same name.

[3] The color charges are responsible for strong interactions.

1.3 Quantum Chromodynamics (QCD)

Quantum Chromodynamics is the theory of strong interaction among the quarks and gluons, collectively known as partons. QCD is described by a non-abelian gauge theory having the symmetry group SU(3). The QCD Lagrangian is invariant under local gauge transformations. Similar to quantum electrodynamics (QED), the gauge quanta of QCD, gluons, are massless. Gluons carry a unit of both color and anti-color, and thus there should be a total of 9 gluons. However, the color singlet state $r\bar{r} + g\bar{g} + b\bar{b}$ is non-existant. Further, the presence of a color-less gluon is also ruled out, which would otherwise make the strong interactions long-range, which is not observed in experiments. Because of the color degrees of freedom of gluons, they can self-interact. QCD effective potential between partons is given as follows [3]:

$$V_{\mathrm{QCD}}(r) = -\frac{4\alpha_S}{3r} + kr. \tag{1.1}$$

Here, α_S is the coupling constant for strong interaction, also known as the running coupling constant, as it depends on the scale of momentum transfer. k is the color string constant, which is equal to 0.85 GeV/fm. It is important to note that V_{QCD} has two terms; at short distances the first term dominates, which is coulombic in nature. At large values of r, the second linear term dominates. The theory of strong interaction, QCD, possesses the following salient features.

1.3.1 Color Confinement

The color confinement is one of the striking features of QCD, which forbids the existence of isolated quarks or gluons (particles having color charges). As discussed, at short distances the Coulomb term in Eq. (1.1) dominates. However, as one moves to larger distances, the linear term dominates. Thus, infinite energy is required to separate two quarks in a bound state. As the distance between two quarks increases, because of the gluon self-coupling, the color lines of force are attracted to form a color string. In this scenario, the potential energy stored in the string becomes large enough to form new quark and anti-quark pairs, as demonstrated in Fig. 1.2. Thus, quarks are always confined within the hadrons and observation of isolated quarks is not possible [5].

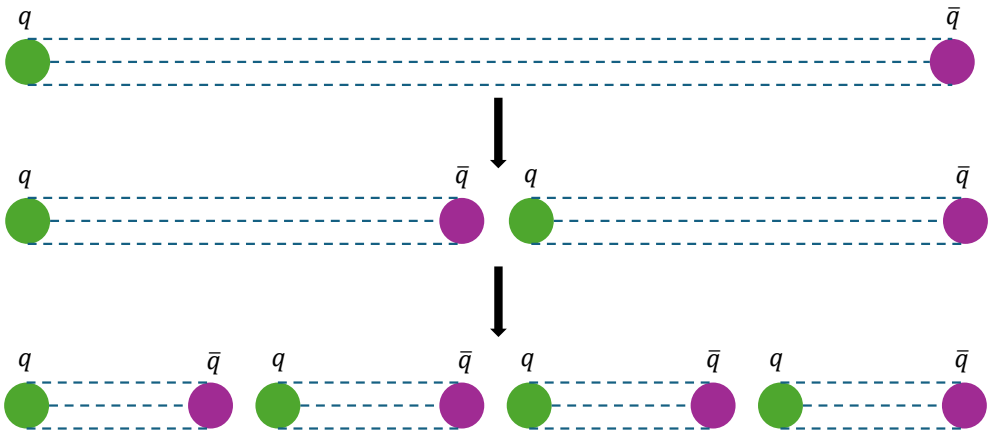

Figure 1.2: Pictorial representation of string breaking by quark-antiquark pair production. Figure is adopted from Ref. [4].

1.3.2 Asymptotic Freedom

Asymptotic freedom is another distinct feature of QCD [4]. It states that the strength of strong interaction among partons becomes weaker as the separation among them decreases or the energy density becomes higher. This comes as a consequence of the running coupling constant, α_s, in Eq. (1.1), which is a consequence of vacuum polarisation of quarks and gluons. Similar to electric charge screening in QED, the creation of quark-antiquark pairs in vacuum can be polarised by color charge, which screens the color charge. Unlike in QED, in QCD the gluons self-interact, which provides an anti-screening effect and makes the coupling constant running. The QCD coupling constant is mainly dependent on the momentum transfer. The coupling constant as a function of momentum transfer (Q^2) is given as follows [7].

$$\alpha_S(Q^2) = \frac{4\pi}{\beta_0 \ln(Q^2/\Lambda^2_{\rm QCD})} \tag{1.2}$$

Here, $\beta_0 = 1/(11-2n_f/3)$ is a constant, where n_f stands for the number of quark flavours. $\Lambda_{\rm QCD}$ ($\simeq$ 200 MeV) is the perturbative QCD (pQCD) scale parameter. As one moves towards smaller values of Q^2, α_S becomes higher and the pQCD breaks down. Similarly, at smaller distances or at large Q^2, α_S is smaller. At $Q^2 \to \infty$, the coupling strength becomes negligible and the partons behave like free particles in a QCD vacuum. This

[4]The discovery of asymptotic freedom was awarded with the Nobel Prize in Physics 2004 to David J. Gross, H. David Politzer and Frank Wilczek [6].

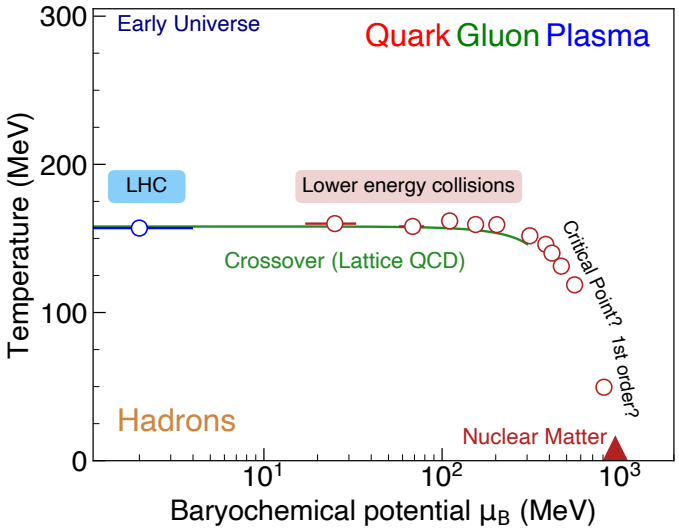

Figure 1.3: A schematic representation of the QCD phase diagram. Figure is taken from Ref. [8]. The accessible regions in μ_B for Lattice QCD calculations are shown in green line and band, which represent the pseudocritical temperature and half width of the crossover temperature, respectively [9]. The open markers show the experimental points for the chemical freeze-out parameters [10–12].

is known as asymptotic freedom. At larger Q^2 and smaller α_s, the pQCD is applicable. One of the consequences of these salient features of QCD hints at the formation of a thermalised QCD-medium, where the partons move freely within the nuclear shell, known as quark-gluon plasma – a case of high temperature QCD.

1.4 Heavy-ion collisions and Quark-Gluon Plasma

The Big Bang theory suggests that the primordial microsecond old universe existed in the form of QGP. The universe evolved through different states from forming primary hadrons to stars, planets and galaxies. Thus, it is crucial to understand the evolution of QGP matter or, more fundamentally, the QCD phase diagram. The heavy-ion collisions at the Relativistic Heavy-Ion Collider (RHIC) at the Brookhaven National Laboratory (BNL) and the Large Hadron Collider (LHC) have the facilities to produce QGP in laboratories. With these experiments, one can probe different regions of the QCD phase diagram illustrated in Fig. 1.3. Here, the y and x axes are represented as temperature (T)

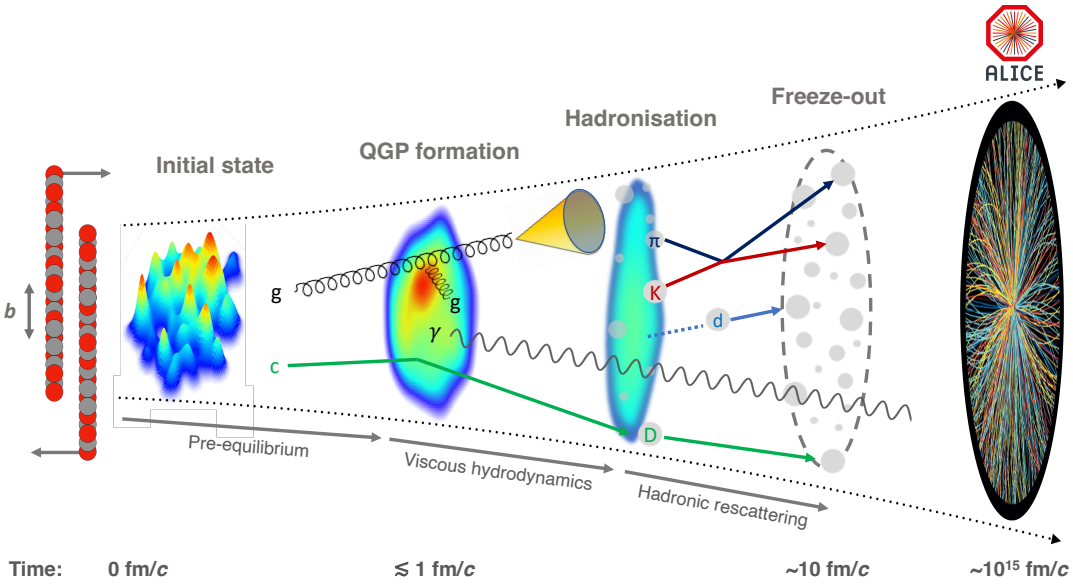

Figure 1.4: Illustration of the evolution of heavy-ion collisions. Figure is taken from Ref. [8].

and baryochemical potential (μ_{B}) [5], respectively. Hadronic matter or hadrons, composed of baryons and mesons, is a state where the quarks and gluons are confined as composite particles. The QCD theory suggests a phase transition from hadronic matter to a quark-gluon phase at high T and μ_{B}. The lattice QCD predicts that the phase transition from hadronic matter to the QGP state happens at around $T = 154$ MeV for $\mu_{\mathrm{B}} = 0$ MeV, achievable at the LHC energies. As one moves towards lower collision energies, the QGP phase starts with a lower temperature and a higher μ_{B} due to baryon stopping near $y_{\mathrm{CM}} = 0$. Although there have been many uncertainties in the understanding of QCD phase diagram from both theoretical and experimental frontiers, in this thesis we focus on the $\mu_{\mathrm{B}} = 0$ region achievable at the LHC energies.

Figure 1.4 shows the spacetime evolution of heavy-ion collisions on different timescales. The evolution of heavy-ion collisions is usually described in many stages, namely, the collision of Lorentz contracted heavy-ions, the pre-equilibrium phase, the QGP phase, the mixed phase, the chemical freeze-out, the hadronic rescattering phase and the kinetic freeze-out. When two heavy ions are accelerated at ultra-relativistic speeds, they acquire

[5]The energy necessary to increase the baryon number of the system by one unit at fixed volume and entropy is called baryochemical potential. It is proportional to the net baryon density of the system.

a disc-like structure when viewed from the Lab frame due to their motion along the beam axis (z-axis). At the time of collisions, due to excitation of a large number of partons in the collision overlap region, a large amount of energy is deposited and a system with large entropy is created. The size of the collision overlap region, and hence the energy and entropy disposition, usually varies with the impact parameter (b) [6]. The impact parameter also controls the number of nucleons participating in the inelastic scattering processes, often denoted as $N_{\rm part}$. Hence, the maximum value of $N_{\rm part}$ is the sum of the number of nucleons of the colliding nuclei. Similarly, the impact parameter of the collision is also proportional to the number of binary inelastic collisions among the nucleons ($N_{\rm coll}$). The maximum value of $N_{\rm coll}$ for A-A collisions can reach up to $A^{4/3}$. Additionally, the nucleons that do not participate in the collisions are termed as spectator nucleons. In the inelastic nuclear collisions, a number of QCD processes occur which involve a range of Q^2 momentum transfers among the interacting partons within the nuclei, where each range plays a distinct role[7]. The partonic interactions with small values of Q^2, largely driven by $N_{\rm part}$, decide the overall energy density in the initial state. Due to the fluctuations of the matter distribution of nuclear matter, small Q^2 interactions lead to the observed "bumpiness" in the initial energy density, as shown in Fig. 1.4 just after the collision. The small Q^2 interactions in the pre-equilibrium phase are followed by the formation of softer partons, and the interactions among them lead to the formation of a QGP state. In contrast, large-Q^2 interactions are driven by $N_{\rm coll}$ and lead to the formation of high-momentum partons and heavy quarks, shown in Fig. 1.4 with the charm quark and gluon trajectories. These heavy-mass quarks or high-momentum partons can provide information about the opaqueness of the QGP medium.

In the QGP state, the mean free path of the constituents is much smaller than the system size, where multiple interactions among the constituents drive the expansion of the QGP medium. The initial non-uniform energy density influences the expansion of the QGP, which leads to the creation of a pressure gradient in the system. The pressure gradients smooth out the bumps in energy density as time passes and cool the system due to expansion. A large pressure at the center as compared to the outskirts leads to a common velocity field directed radially outwards, known as radial flow. Similarly, a

[6] Impact parameter is the perpendicular distance between the centres of the colliding nuclei.

[7] Q^2 is the square of the four-momentum transferred.

directional dependence of these pressure gradients leads to the formation of anisotropic flow. The rate of QGP hydrodynamic expansion is governed by its bulk viscosity, which provides a resistance to an increase in volume. On the other hand, the shear viscosity of the fluid provides resistance to the fluid deformation.

As the system expands and cools down, the parts of QGP which has a temperature smaller than the transition temperature will start to hadronise. According to Lattice QCD, the transition from partonic matter to nuclear matter is a smooth crossover. The hard partons will hadronise via fragmentation [13], while the soft partons hadronise with a coalescence mechanism [14]. Once, pions (π), kaons (K) and protons (p) are produced from the partons, the energy density can be large enough for a consequent change in the chemical composition of the produced hadrons through inelastic scatterings. The deuteron (d), shown in Fig. 1.4, is especially sensitive to such interactions, which can be formed and destroyed easily in this phase. This phase, till the chemical composition of the hadrons is fixed, is characterised by a chemical freeze-out temperature ($T_{\rm chem}$). The elastic hadronic scatterings can still continue till the kinetic freeze-out is achieved, where the average mean free path becomes larger than the system size.. The kinetic freeze-out is characterised by a temperature, $T_{\rm kin}$, after which the hadrons freely stream towards the detectors and are detected.

Since the QGP phase produced in experiments is transient, with a lifetime of the order of a few femtoseconds, a direct observation of the QGP phase is not possible. However, the formation of QGP in experiments can be inferred by studying its signatures, discussed in the following sections.

1.5 Coordinate system

Before I proceed to further discuss the signature of quark-gluon plasma, it is necessary to introduce the coordinate system. In collider experiments, the direction of the incoming ions is the z-axis or the longitudinal axis, or usually called the beam-axis. One can define a transverse plane (x, y) which is perpendicular to the z-axis, as depicted in Fig. 1.5. After the collision, the particles are produced with four momentum, (E, p_x, p_y, p_z) and are detected in the detectors. One can determine their transverse momentum ($p_{\rm T}$ =

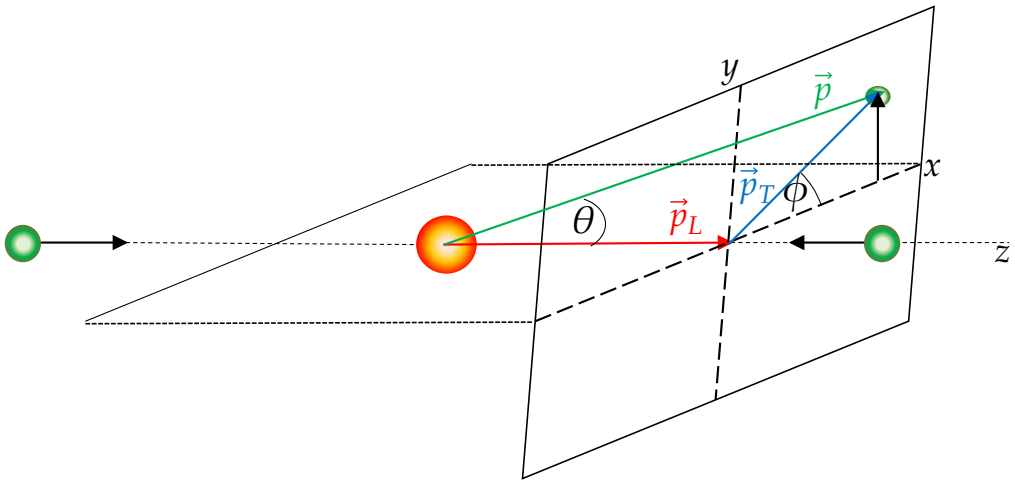

Figure 1.5: Pictorial representation of coordinate system in heavy-ion or hadronic collisions [15–17].

$\sqrt{p_x^2 + p_y^2}$), polar angle ($\theta = \tan^{-1}\left[\frac{|\vec{p}_T|}{p_z}\right]$), azimuthal angle ($\phi = \tan^{-1}\left[\frac{p_y}{p_x}\right]$), rapidity ($y = \frac{1}{2}\ln\left[\frac{E+p_z}{E-p_z}\right]$) and pseudorapidity ($\eta = -\ln[\tan(\theta/2)]$), etc. If a particle is emitted perpendicular to the beam axis, its $\eta = 0$, and η increases as one moves closer to the beam axis. Hence, the detector plane can be spanned by (η, ϕ).

1.6 Signatures of QGP

The are several proposed signatures of QGP formed in heavy-ion collisions. This includes the strangeness enhancement, jet quenching, collectivity, quarkonia suppression, etc., to name a few. In this thesis, I shall discuss the collectivity and strangeness enhancement as follows.

1.6.1 Collective Flow

The strongly interacting matter of deconfined partons exhibits a collective expansion. This collective expansion of the system is explained by hydrodynamic equations, as the mean free path of the constituents of the QCD plasma is very small compared to the size of the plasma itself. In Section 1.4, we saw that the pressure gradient is developed due to non-

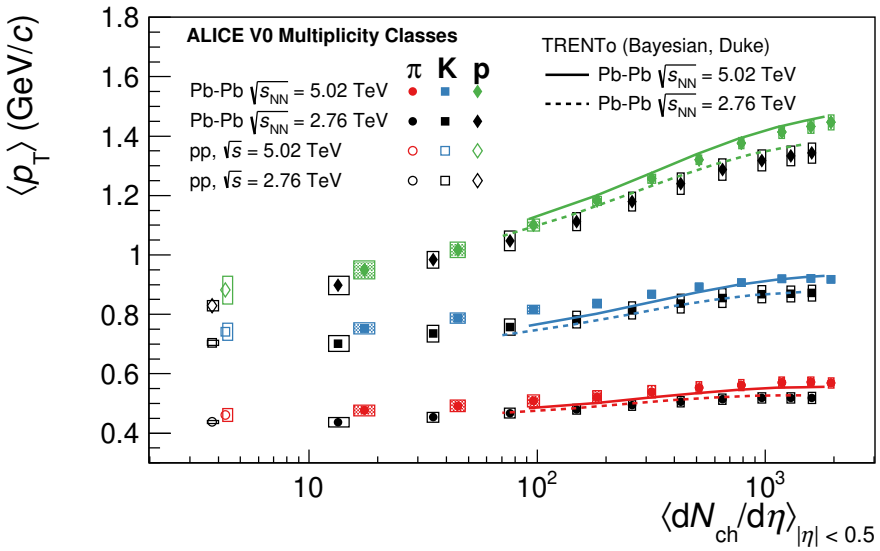

Figure 1.6: Charged particle multiplicity density dependence of $\langle p_{\mathrm{T}} \rangle$ for charged pions (π), kaons (K) and protons (p) in Pb–Pb collisions at $\sqrt{s_{\mathrm{NN}}} = 5.02$ and 2.76 TeV with ALICE [20].

uniform energy density. Further, the pressure at the core of the system is large compared to the periphery. This leads to a collective radial expansion of the system, known as radial flow. This radial flow is said to provide additional boost to the particles thermally produced, leading to a rise in their average transverse momentum ($\langle p_{\mathrm{T}} \rangle$) [18, 19]. A denser system tends to have a larger $\langle p_{\mathrm{T}} \rangle$ as compared to a less dense system. Additionally, the boost is higher for heavier particles as compared to lighter particles. This is shown in Fig. 1.6 where the average transverse momentum ($\langle p_{\mathrm{T}} \rangle$) for charged pions ($\pi$), kaons ($K$) and protons ($p$) is presented as a function of average charged particle multiplicity density ($\langle dN_{\mathrm{ch}}/d\eta \rangle$) measured at $|\eta| < 0.5$ in Pb–Pb collisions at $\sqrt{s_{\mathrm{NN}}} = 5.02$ and 2.76 TeV with ALICE [20]. With an increase in $\langle dN_{\mathrm{ch}}/d\eta \rangle$, a rise in $\langle p_{\mathrm{T}} \rangle$ is observed for all the particles, this indicates that as one moves towards the central collisions, where the energy density and $\langle dN_{\mathrm{ch}}/d\eta \rangle$ are the largest, a more radially boosted system is formed. Further, the rise is more prominent for the protons as compared to kaons and pions, which have the least slope for $\langle p_{\mathrm{T}} \rangle$ vs $\langle dN_{\mathrm{ch}}/d\eta \rangle$. This is a testimony that the particles with larger mass gain a higher boost from the radial flow.

In addition to radial flow, which develops due to the outward pressure of the strongly interacting plasma, the directional dependence of pressure gradients leads to the genera-

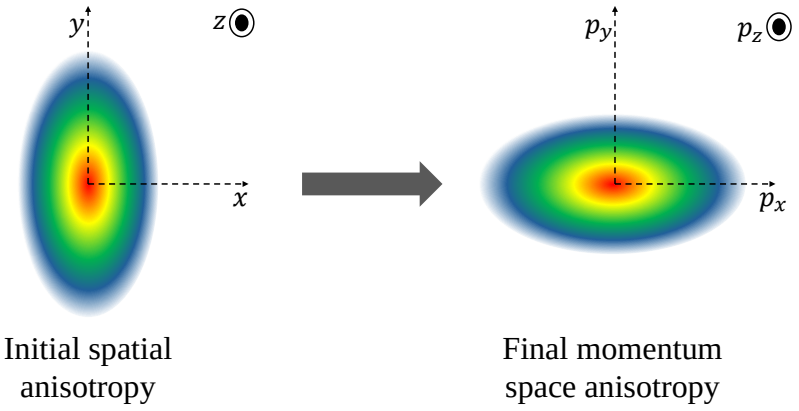

Figure 1.7: Pictorial representation of transformation of initial spatial anisotropy to final state azimuthal anisotropy in momentum space.

tion of anisotropic flow. In non-central heavy-ion collisions, the collision overlap region is almond-shaped having finite spatial anisotropy in the collision overlap region. Thus, the pressure gradient is higher in one direction and smaller in another, as depicted in Fig. 1.7. In addition to the initial almond-shaped structure in the non-central collisions, which gives rise to eccentricity (ϵ_2), the density fluctuations in the collision overlap region can give rise to higher-order spatial anisotropies such as triangularity (ϵ_3), quadrangularity (ϵ_4), etc. One can quantify the initial spatial anisotropy of order n using the following expression [21, 22].

$$\epsilon_n = \frac{\sqrt{\langle r^n \cos(n\phi_{\rm part})\rangle^2 + \langle r^n \sin(n\phi_{\rm part})\rangle^2}}{\langle r^n \rangle} \tag{1.3}$$

In Eq. (1.3), r and $\phi_{\rm part}$ are the polar coordinates of the participant nucleons in the collision overlap region. Thus, the pressure gradient drives the transformation of initial spatial anisotropy into final state momentum space anisotropy known as anisotropic flow. The anisotropic flow is quantified using the coefficients of the Fourier expansion of the azimuthal distribution of the particles, given as follows [23].

$$\frac{dN}{d\phi} \propto \left(1 + 2\sum_{n=1}^{\infty} v_n \cos\left[n(\phi - \psi_n)\right]\right) . \tag{1.4}$$

In Eq. (1.4), ϕ is the azimuthal angle of the produced particles, v_n is the nth harmonic anisotropic flow coefficient, ψ_n is the corresponding symmetry plane angle. The anisotropic flow is quantified with v_n, where $n = 1$ stands for directed flow, $n = 2$ for

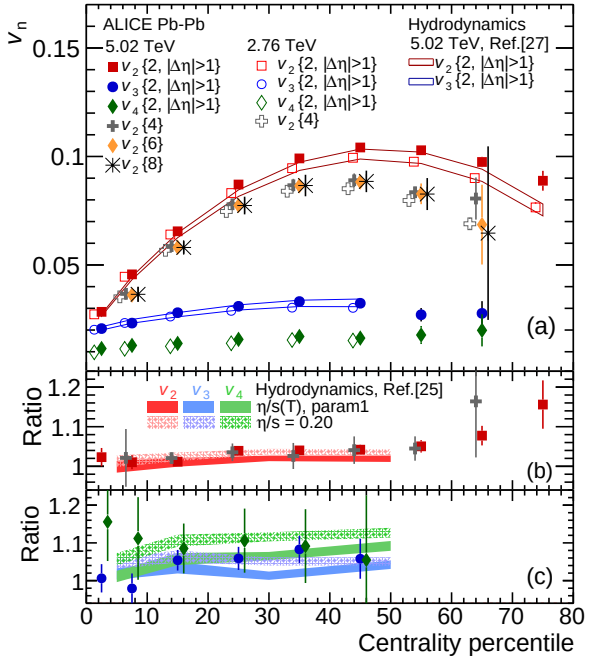

Figure 1.8: Centrality dependence of anisotropic flow coefficients in Pb-Pb collisions at the LHC energies with ALICE [24].

elliptic flow, $n = 3$ for triangular flow, etc. It is important to note that the anisotropic flow coefficients are highly influenced by the initial spatial anisotropy are depend upon the transport coefficients of the medium. Especially, the higher-order anisotropic flow coefficients are highly sensitive to the medium response.

Figure 1.8 shows the collision centrality dependence of anisotropic flow coefficients (v_n) in Pb-Pb collisions at $\sqrt{s_{\rm NN}} = 5.02$ and 2.76 TeV with ALICE. As one moves from the most central to the mid-central collisions, v_2 increases as the collision geometry becomes more and more elliptic. However, towards the peripheral collisions, v_2 starts to decrease, which is a consequence of the limited lifetime of the fireball that fails to transform the initial eccentricity into the final state. Interestingly, v_3 and v_4 show similar qualitative behaviour for different centrality classes as v_2. However, their centrality dependence is weaker. In fact, we observe $v_2 > v_3 > v_4$, which indicates that the higher-order coefficients have a smaller contribution to the overall anisotropy of the system formed. Further, one finds a higer v_n for $\sqrt{s_{\rm NN}} = 5.02$ TeV in comparison to 2.76 TeV which depicts that anisotropic flow coefficients also depend upon the center of mass energy of the collisions which is true as a system with higher $\sqrt{s_{\rm NN}}$ would possess a higher pressure gradient and fireball

lifetime which would faciliate the transformation of initial to final state anisotropies.

1.6.2 Strangeness Enhancement

The study of strange and multi-strange hadron production can also signify the formation of the QGP medium in heavy-ion collisions, known as strangeness enhancement [25–27]. The ions before the collisions consist of only up and down quarks, and the strange quarks are absent. During the initial stages of the collision, strange quarks are produced via hard perturbative processes such as flavour creation ($q\bar{q} \rightarrow s\bar{s}$), flavour excitation ($gs \rightarrow gs$, $qs \rightarrow qs$) and gluon fusion ($gg \rightarrow s\bar{s}$). In heavy-ion collisions, where a QGP medium is expected to be formed, the strange quark production via gluon fusion dominates over flavour creation. In contrast, in minimum bias pp collisions, the primary source of strangeness production is through flavour creation. One can measure the enhancement factor (E) of strange hadron production using the following relation.

$$E = \frac{2}{\langle N_{\rm part} \rangle} \left[\frac{dN^{AA}/dy\big|_{y=0}}{dN^{pp}/dy\big|_{y=0}} \right] \tag{1.5}$$

Here, $N_{\rm part}$ is the number of participant nucleons, $dN^{AA}/dy\big|_{y=0}$ and $dN^{pp}/dy\big|_{y=0}$ are the strange particle multiplicity density at midrapidity in AA and pp collisions, respectively. However, recent measurements show the enhancement feature of strange hadrons by scaling to the yield of non-strange hadrons such as pions. This is more practical as it avoids the requirement of a baseline measurement from different systems, such as proton-proton. Figure 1.9 shows the strange hadrons to pions ratios as a function of charged particle multiplicity density ($\langle dN_{\rm ch}/d\eta \rangle_{|\eta|<0.5}$) measured at mid-pseudorapidity with ALICE [28]. At first glance, one finds that as the strangeness quantum number of the strange hadron increases, the enhancement is stronger with an increase in $\langle dN_{\rm ch}/d\eta \rangle_{|\eta|<0.5}$. Interestingly, pp and p–Pb collisions show similar enhancement features as observed in Pb–Pb collisions. This hints towards a possible formation of QGP droplets in small systems.

1.7 QGP in small systems

As shown in Fig. 1.9, small systems like pp and p-Pb collisions at high-multiplicity show strangeness enhancement features similar to those observed in heavy-ion collisions. These

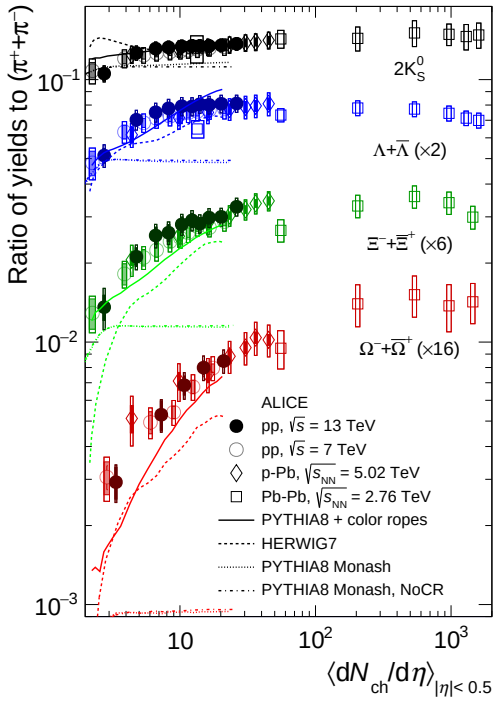

Figure 1.9: Multiplicity dependence of strange hadrons to pions ratios with ALICE at the LHC energies [28].

heavy-ion like signatures are not limited to strangeness ehancements, additional signatures like radial flow [28, 29], ridge-like structures [30, 31], and more recently, the elliptic flow [32] have also been observed in pp and p-Pb collisions, which hints towards the presence of collectivity of the system formed.

Traditionally, several studies of QGP signatures in heavy-ion collisions have been employing pp collisions as the baseline measurements. p–Pb collisions, on the other hand, serve as the baseline for cold nuclear matter effects. Thus, the observation of the QGP signatures in pp and p–Pb collisions has led the heavy-ion physics community to investigate small collision systems from different angles. One of the most useful methods to study these signatures is by separating the p-QCD dominated hard events from the soft events with the help of event classifiers such as transverse spherocity (S_0) [33, 34], transverse sphericity (S_T) [35, 36], relative transverse activity classifier (R_T) [37–39], charged particle flattenicity (ρ_{ch}) [40–42] etc.

1.8 Motivation

The observation of QGP-like signatures in high-multiplicity pp collisions has intrigued the scientific community, and dedicated efforts have been made to understand the small systems better. The traditional event classifier, charged particle multiplicity, has significant selection bias as the measurement of charged particle multiplicity and particle identification in similar rapidity regions. Although these biases can be reduced by measuring the multiplicity in different rapidity regions, the event classifiers based on multiplicity are still affected by the multi-jet topologies [43, 44]. Thus, in this thesis, the strangeness enhancement features of different strange hadrons in pp collisions are studied as a function of different event classifiers. Further, the charged particle flattenicity has been used to study the strangeness production in ALICE experiments in pp collisions. This thesis also discusses the applicability of transverse spherocity in heavy-ion collisions such as Pb-Pb at the LHC energies, to study global properties, anisotropic flow and their fluctuations.

1.9 Organisation of Chapters

The thesis is organised as follows. Chapter 1 starts with an introduction to heavy-ion collisions, quark-gluon plasma and its observations in small system collisions. In Chapter 2, I discuss the production of strange hadrons in pp collisions with different event shape observables. Chapter 3 is dedicated to a brief discussion on the ALICE experiment and its detector setup used for the contents of this thesis. Chapter 4 focuses on the production of neutral strange hadrons such as K^0_S and $\Lambda + \bar{\Lambda}$ as a function of charged particle flattenicity in pp collisions at $\sqrt{s} = 13.6$ TeV with ALICE. Chapter 5 shows the applicability of transverse spherocity in heavy-ion collisions at the LHC. Finally, I summarise the thesis in Chapter 6.

Chapter 2

Probing strangeness enhancement with event shape observables

Based on:

1. *S. Prasad, B. Sahoo, S. Tripathy, N. Mallick, and R. Sahoo, "Probing strangeness with event topology classifiers in pp collisions at energies available at the CERN Large Hadron Collider with the rope hadronization mechanism in PYTHIA", Phys. Rev. C 111, 044902 (2025).*

2. *S. Prasad, N. Mallick and R. Sahoo, "Inclusive, prompt and nonprompt J/ψ identification in proton-proton collisions at the Large Hadron Collider using machine learning", Phys. Rev. D 109, 014005 (2024).*

2.1 Introduction and Motivation

The strange hadron yield relative to pions in heavy-ion collisions increase with an increase in collision energy and from peripheral to central collisions [45, 46]. In string fragmentation-based models, the production of strange hadrons is significantly suppressed as compared to pions in elementary pp and e^++e^- collisions, where the thermal production of strange quarks is not possible due to their large mass ($m_s > T$). However, recent measurements in high multiplicity pp collisions at the LHC reveal observations of nonzero

elliptic flow coefficient [32, 47], long-range near-side angular correlation [48], characteristic modifications of baryon to meson ratios [49], and enhanced production of strange and multi-strange hadrons, which are believed to be achievable in ultra-relativistic nuclear collisions. This indicates that a common underlying physics mechanism drives these observations throughout the collision systems and energies. However, other indirect signatures of QGP, such as quarkonia suppression, jet quenching, etc., have not been observed in small collision systems [50]. The Monte Carlo (MC) based event generators thus fail to simultaneously reproduce all the experimentally observed features in pp and p–Pb collisions, which questions the existence of a QGP medium in small collision systems and the true microscopic origin of these observed heavy-ion-like features is still unclear.

On the other hand, p-QCD-based models such as PYTHIA 8 [51] with multipartonic interactions (MPI) and hadronisation based on color reconnection (CR) [52], rope hadronisation (RH) [53], and string shoving [54] are able to explain many of these heavy-ion-like features in pp collisions. However, MPI is not an experimentally measurable quantity, and thus, several experimental measurements are performed as a function of charged particle multiplicity in the final state, which shows a significant correlation with MPI. Studies show that the measurements as a function of charged particle multiplicity are significantly biased and are prone to contributions from multi-jet topologies [43]. Thus, it is important to find event shape classifiers that are sensitive to the intrinsic number of MPI ($N_{\rm mpi}$) and are less prone to contributions from multiple-jet topologies. Event shape observables, such as transverse spherocity (S_0) [33, 34], transverse sphericity ($S_{\rm T}$) [35, 36], relative transverse activity classifier ($R_{\rm T}$) [37–39], charged particle flattenicity ($\rho_{\rm ch}$) [40–42], etc., are sensitive to $N_{\rm mpi}$ and can separate soft-QCD dominated isotropic events from the hard-QCD dominated jetty events. However, every event shape observable is intrinsically different, and thus, its usefulness may differ from one study to another. In this chapter, we study the production of strange and multi-strange hadrons as a function of different event classifiers, including different event shape observables, to tell the experimentalists which one of these event shape observables is best suited to study strangeness production in pp collisions at the LHC. We use PYTHIA 8 to generate pp collisions at $\sqrt{s} = 13$ TeV to perform this study.

The chapter is organised as follows. We start with the motivation of the chapter in

Section 2.1. In Section 2.2, we discuss the data generation using PYTHIA 8 along with CR and RH. Section 2.3 is dedicated to the definition of different event classifiers used in this study. We discuss the results in Section 2.4. Finally, the chapter is summarised in Section 2.5.

2.2 Data generation using PYTHIA 8

PYTHIA 8 is a p-QCD-based Monte Carlo event generator to simulate hadronic, leptonic and nuclear collisions with a special focus on elementary collisions like pp and e^++e^- collisions [55]. It incorporates soft and hard QCD processes along with models for physical phenomena such as beam remnants, initial and final state parton showers, string fragmentations, and particle decays [56]. PYTHIA8, by default, uses a string fragmentation mechanism for the hadronisation. Additionally, it has color reconnection (CR) and rope hadronisation (RH) mechanisms that mimic some of the collective-like phenomena and enhanced production of strange hadrons and baryons in pp collisions. The physics mechanisms involved are discussed as follows.

2.2.1 Multi-Partonic Interactions

Elementary proton-proton collisions at the RHIC and LHC produce a multitude of particles in the final state. The current description of particle production in such systems is given by the QCD-inspired parton model, which assumes the composite nature of colliding protons (or any hadron in general) leading to multiple partonic scatterings or MPI which are usually soft in nature. Moreover, in a hard proton-proton collision, the hard scattered partons are sometimes accompanied by additional soft interactions known as underlying event (UE) activity. The non-perturbative nature, along with their large numbers and complex interplay between interactions, MPI can only be modelled in MC event generators, such as PYTHIA8 [57, 58].

MPIs are modelled as the sum of incoherent sub-collisions consisting of $2 \rightarrow 2$ partonic interactions [59]. As $p_{\mathrm{T}} \rightarrow 0$, the QCD cross-sections for the individual sub-collisions start to diverge and finally exceed the total cross-section. Thus, a regularization is necessary to avoid the unphysical cross sections at low-p_{T}. In PYTHIA8, a transverse momentum

cut-off value, p_{T_0}, is used to regularise the cross sections as follows [59]:

$$\frac{\mathrm{d}\hat{\sigma}}{\mathrm{d}p_{\mathrm{T}}^2} \propto \frac{\alpha_S^2(p_{\mathrm{T}}^2)}{p_{\mathrm{T}}^4} \rightarrow \frac{\alpha_S^2(p_{\mathrm{T}_0}^2 + p_{\mathrm{T}}^2)}{(p_{\mathrm{T}_0}^2 + p_{\mathrm{T}}^2)^2}, \tag{2.1}$$

where p_{T_0} depends upon the center of mass energy of the collision as follows:

$$p_{\mathrm{T}_0}(s) = p_{\mathrm{T}}^{\mathrm{ref}} \left(\frac{\sqrt{s}}{\sqrt{s_0}} \right)^{\epsilon}. \tag{2.2}$$

Here, $p_{\mathrm{T}}^{\mathrm{ref}}$ and ϵ are free parameters that can be tuned [59] to match the experimental data. It is interesting to note that p_{T_0} increases with an increase in collision energy, which is due to the increase in the low-x partons in the wavefunction of colliding protons. Additionally, in PYTHIA8, the number of MPI (N_{mpi}) also depends upon the impact parameter determined as the spatial overlap of the transverse profile of the colliding protons, which makes the MPI picture more realistic. The number of final state hadrons increases with an increase in N_{mpi}.

2.2.2 Color Reconnection

Once MPI has produced a colored final state, it is hadronised. In PYTHIA8, the hadronisation occurs via Lund string model [60]. In fragmentation-based models, the hadronisation can be conceived as a stretched color flux tube connecting two partons, which originate as a result of individual partonic scatterings and leads to a linear confinement through a massless relativistic string. As the potential energy of the strings increases, the pairs consisting of quarks and antiquarks move apart till a new quark-antiquark pair is formed. The combinations of the quarks and antiquarks lead to the formation of hadrons. Thus, the hadronisation through simple fragmentation-based models is independent in individual scatterings. Further, with the increase in N_{mpi}, the average number of charged particles in the final state also increase, and no rise in average transverse momentum, in contrast to experiments, would be observed due to jet universality. Thus, an intermediate step between MPI and hadronisation is necessary to break the incoherence introduced by MPI. With color reconnection, the partonic endpoints from individual scatterings can color reconnect [61]. In other words, CR adjusts the color flow among the partons from different scatterings to minimise the total string length, which can lead to a rise in their average transverse momentum at the cost of final state multiplicity. In PYTHIA8, the usual picture of color reconnection follows one of the following three models [62].

2.2.2.1 MPI based CR (CR0)

In this model, the probability of colored partons from MPI to reconnect is given as follows:

$$P_{\mathrm{rec}}(p_{\mathrm{T}}) = \frac{R_{\mathrm{rec}} \cdot p_{\mathrm{T}_0}}{R_{\mathrm{rec}} \cdot p_{\mathrm{T}_0} + p_{\mathrm{T}}^2}. \tag{2.3}$$

Here, R_{rec} is `ColorReconnection:range` and p_{T_0} is the `MultipartonInteractions:pT0Ref` parameters, which are tunable. For individual MPI that participate in CR, partons from lower p_{T} MPI are added to the dipoles defined by a high-p_{T} MPI in a way which leads to a smaller string length.

2.2.2.2 QCD based model (CR1)

This is an improved version of MPI based model, where a more complete treatment of the QCD multiplet structure is considered. Further, the reconnections of dipoles can produce structures of three color/anticolor indices/junctions, which can enhance the baryon production in general. In this model, only reconnections where the string length is lowered are performed.

2.2.2.3 Gluon-move model (CR2)

In this model, the reconnection mechanism is similar to the CR0 model. The main difference is that in the CR2 model, only gluons are considered for reconnection. Here, for each gluon, all the reconnections to all MPI systems are considered. In contrast, CR0 reconnections with only softer MPI systems are considered. Therefore, the color flow from hard scatterings can be affected more significantly in CR2 than in CR0.

2.2.3 Rope Hadronisation

The ultra-relativistic collisions at the RHIC and LHC can lead to a large number of N_{mpi} along with the production of several strings which connect the partonic endpoints in a smaller transverse region. In rope hadronisation, these strings can overlap and act coherently to form a color rope with a large effective string tension and possessing higher energy density than the nearby regions. This difference in the energy density leads to the formation of a pressure gradient, which pushes the strings in an outward direction, known

as string shoving. The string shoving mechanism in PYTHIA8 can effectively mimic the flow-like pattern similar to that observed in heavy-ion collisions. As the strings are pushed outward, the effective tension rises, the breaking of which leads to the production of strange quarks and diquarks and finally to the enhanced production of baryons and strange hadrons in events having large $N_{\rm mpi}$ in contrast to when RH is not active.

The results presented in this chapter are performed with PYTHIA8 (version 8.308), an advanced version of PYTHIA6 which includes improved multi-partonic interactions and color reconnection features. We have used Monash tune (`Tune::pp=14`) [63] of PYTHIA 8 to generate 6×10^7 minimum bias pp collisions at $\sqrt{s}$ = 13 TeV. Additionally, we include the inelastic sector of soft QCD processes (`softQCD:inelastic=on`), which allow single, double and central diffractive processes. MPI (`PartonLevel:MPI=on`) and mode 1 of color reconnection (`ColorReconnection:mode=1`) have also been implemented, which mimics the collective-like behaviour. To enhance the production of strange hadrons, we also implement the rope hadronisation through the production of color ropes; the specific details of the PYTHIA8 settings are given in Table 2.1. To set impact parameter plane vertices for parton production by ISR, FSR, MPI and beam remnants, the parton vertex flag is turned on (`PartonVertex:setVertex=on`). Further, we allow all the resonance hadrons to decay (`HadronLevel:Decay=on`) except for the ones that are used in this study.

In this chapter, the mention of Color Ropes would imply PYTHIA8 Monash 2013 tune with the inclusion of QCD-based CR and RH mechanisms. Further, Monash would imply PYTHIA8 default 2013 Monash tune and Monash NoCR would correspond to PYTHIA8 2013 Monash without color reconnection.

The left and right panels of Fig. 2.1 show the transverse momentum and pseudorapidity spectra of all charged hadrons, respectively, in pp collisions at $\sqrt{s} = 13$ TeV using PYTHIA8 color ropes and compared with that obtained from ALICE experiment. It is observed that PYTHIA8 provides a good qualitative agreement to the experimental measurements. Since, PYTHIA8 color ropes overestimate the experimental measurements, PYTHIA8 results are scaled to match the spectral shape of experimental results.

Rope Hadronization	Value
`Ropewalk:RopeHadronization`	`on`
`Ropewalk:doShoving`	`on`
`Ropewalk:doFlavour`	`on`
`Ropewalk:r0`	`0.5`
`Ropewalk:m0`	`0.2`
`Ropewalk:beta`	`1.0`
`Ropewalk:tInit`	`1.0`
`Ropewalk:deltat`	`0.05`
`Ropewalk:tShove`	`10.0`

Table 2.1: The parameter values of the rope hadronisation model used with color reconnection mechanism in PYTHIA8 [57].

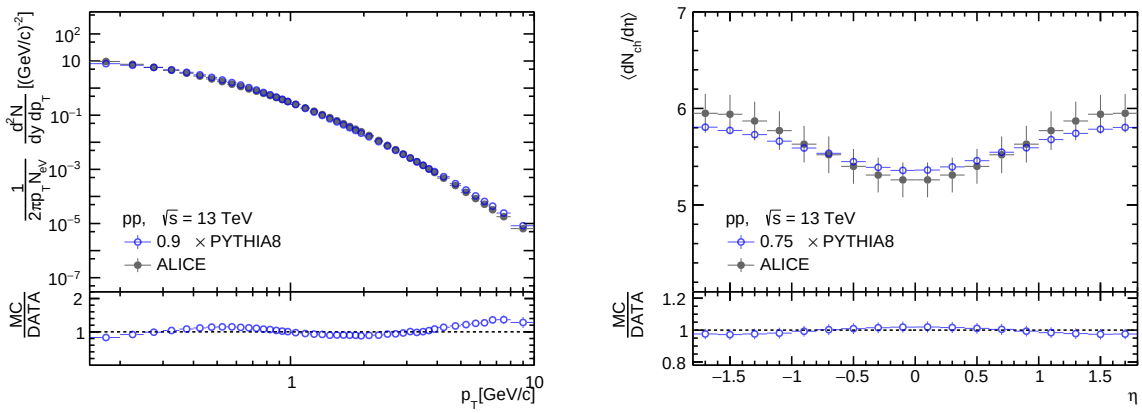

Figure 2.1: Comparison of transverse momentum spectra (left) and pseudorapidity spectra (right) of all charged hadrons obtained from PYTHIA8 color ropes with ALICE measurements [64] in pp collisions at $\sqrt{s} = 13$ TeV [57].

2.3 Event classifiers

In this section, we discuss some of the event classifiers, such as charged particle multiplicity at midrapidity ($N_{\rm ch}^{\rm mid}$) and forward rapidity ($N_{\rm ch}^{\rm fwd}$), transverse sphericity ($S_{\rm T}$), weighted and unweighted transverse spherocity (S_0 and $S_0^{p_{\rm T}=1}$), relative transverse activity classifier ($R_{\rm T}$), and charged particle flattenicity (ρ_{ch}), which have been used in this chapter to probe the production strange hadrons in proton-proton collisions.

2.3.1 Charged Particle Multiplicity ($N_{\rm ch}$)

The charged particle multiplicity is one of the most fundamental event classifiers, which can give information about system size formed in relativistic collisions. It is also one of the common event classifiers at the LHC. In the ALICE experiment at the LHC, the charged particles are usually measured in two pseudorapidity regions. The charged particle multiplicity at the midpseudorapidity is measured with a time projection chamber (TPC) and silicon pixel detector (SPD), which covers the pseudorapidity range $|\eta| < 0.8$. In this chapter, we denote the charged particle multiplicity in $|\eta| < 0.8$ as $N_{\rm ch}^{\rm mid}$. In contrast, the charged particle multiplicity at the forward pseudorapidity region is measured based on the total charge deposited in the V0 (V0A + V0C) detector, which covers the pseudorapidity region $-3.7 < \eta < -1.7$ (V0C) and $2.8 < \eta < 5.1$ (V0A). The charged particle multiplicity in the V0 detector region is denoted as $N_{\rm ch}^{\rm fwd}$. The study of particle production at different pseudorapidity coverages is helpful in understanding different potential biases in the measurements.

2.3.2 Transverse Sphericity ($S_{\rm T}$)

Transverse sphericity ($S_{\rm T}$) is one of the event shape observables which was initially used at the SLAC to test the existence of jets in e^+e^- collisions [36]. $S_{\rm T}$ is defined based on the eigenvalues of the transverse momentum matrix ($S_{\rm xy}^{\rm Q}$), as follows [35]:

$$S_{\rm xy}^{\rm Q} = \frac{1}{\sum_i p_{{\rm T}_i}} \sum_i \begin{pmatrix} p_{{\rm x}_i}^2 & p_{{\rm x}_i} p_{{\rm y}_i} \\ p_{{\rm y}_i} p_{{\rm x}_i} & p_{{\rm y}_i}^2 \end{pmatrix}, \tag{2.4}$$

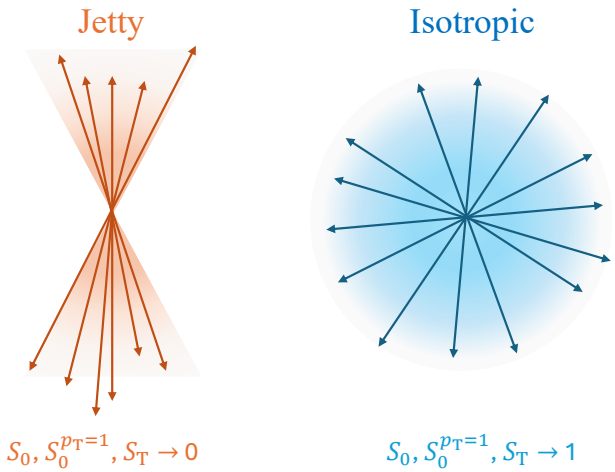

Figure 2.2: Pictorial representation of jetty (left) and isotropic (right) event topology.

where, (p_{x_i}, p_{y_i}) are the projections of transverse momentum (p_{T_i}) of ith particle in (x, y) directions and 'i' runs over all the charged hadrons in an event. Moreover, the superscript 'Q' denotes the quadrature nature of the particle momenta. This quadrature nature makes S_{xy}^{Q} non-collinear safe. Eq. (2.4) can be linearised to make it collinear-safe, as follows.

$$S_{xy}^{L} = \frac{1}{\sum_i p_{T_i}} \sum_i \frac{1}{p_{T_i}} \begin{pmatrix} p_{x_i}^2 & p_{x_i} p_{y_i} \\ p_{y_i} p_{x_i} & p_{y_i}^2 \end{pmatrix}, \tag{2.5}$$

where the superscript 'L' denotes the linearised nature of the momentum matrix. One can calculate the eigenvalues of S_{xy}^{L} as λ_1 and λ_2 such that $\lambda_1 > \lambda_2$, and S_T can be constructed as follows:

$$S_T = \frac{2\lambda_2}{\lambda_1 + \lambda_2}. \tag{2.6}$$

By definition, S_T can vary between 0 and 1. The extreme limits, $S_T \to 0$ denotes the jetty events while $S_T \to 1$ would correspond to isotropic events, as shown in Fig. 2.2. In this chapter, S_T is calculated with all charged particles in $|\eta| < 0.8$ and $p_T > 0.15$ GeV/c. For a statistically meaningful concept event topology, only the events satisfying $N_{ch}^{mid} \geq 10$ have been considered for the studies related to S_T.

2.3.3 Transverse Spherocity (S_0)

Transverse spherocity is another event shape classifier which can separate hard-QCD-dominated jetty events from soft-QCD-dominated isotropic events. The traditional defi-

nition of transverse spherocity is given as follows [34]:

$$S_0 = \frac{\pi^2}{4} \min_{\hat{n}} \left(\frac{\sum_{i=1}^{N_{\rm ch}} |\vec{p}_{{\rm T}_i} \times \hat{n}|}{\sum_{i=1}^{N_{\rm ch}} |\vec{p}_{{\rm T}_i}|} \right)^2. \tag{2.7}$$

In Eq. (2.7), $\hat{n}$ is a unit vector in the transverse plane, which is chosen to minimise the bracketed term. $N_{\rm ch}$ is the number of charged hadrons in an event, and the multiplication factor $\pi^2/4$ makes sure S_0 to lie between 0 and 1. The extreme limits, $S_{\rm T} \to 0$, correspond to the jetty events dominated by hard-QCD processes, while $S_{\rm T} \to 1$ stands for the isotropic events where soft-QCD processes dominate the particle production (shown in Fig. 2.2). Similar to $S_{\rm T}$, S_0 is also collinear and infrared safe, which is explicitly shown in Ref. [58]. S_0 is calculated with charged particles in $|\eta| < 0.8$ with $p_{\rm T} > 0.15$ GeV/c. Only the events with $N_{\rm ch}^{\rm mid} \geq 10$ are considered for the studies with transverse spherocity.

The definition of transverse spherocity given in Eq. (2.7) is $p_{\rm T}$ weighted. This weighted definition of transverse spherocity induces a neutral jet bias in the measurements, which is shown and discussed in Ref. [33]. The jet bias effects can be reduced by modifying the definition of transverse spherocity as follows:

$$S_0^{p_{\rm T}=1} = \frac{\pi^2}{4} \min_{\hat{n}} \left(\frac{\sum_{i=1}^{N_{\rm ch}} |\hat{p}_{\rm T} \times \hat{n}|}{N_{\rm ch}} \right)^2. \tag{2.8}$$

Here, the transverse momentum of all the charged particles is set to one, i.e., $|\vec{p}_{\rm T}| = 1$, to remove the jet biases towards the high-$p_{\rm T}$-particles. Moreover, in the denominator, $\sum_i |\vec{p}_{{\rm T}_i}|$ is replaced with $N_{\rm ch}$. Eq. (2.8) is $p_{\rm T}$-unweighted and thus called as unweighted transverse spherocity, denoted as $S_0^{p_{\rm T}=1}$. Similar to $S_{\rm T}$ and S_0, for the estimation of $S_0^{p_{\rm T}=1}$, we consider charged particles with $|\eta| < 0.8$ and $p_{\rm T} > 0.15$ GeV/c and only the events having $N_{\rm ch}^{\rm mid} \geq 10$ are considered.

2.3.4 Relative Transverse Activity Classifier ($R_{\rm T}$)

Recently, an event classifier, a relative transverse activity classifier ($R_{\rm T}$), is defined to quantify the selection bias towards hard-QCD processes when one selects pp collisions events with large event activity. These selection biases can significantly affect the measurements. The selection bias can be reduced by removing the jet contributions from the event shape estimators. This is efficiently done by choosing an axis that allows the event-by-event separation of jet contribution from the underlying event activity. The direction

of the highest transverse momentum particle (trigger or leading particle) is used as a reference to measure the relative azimuthal angles ($\Delta\phi = \phi^{\rm trig} - \phi^{\rm asso}$) of all other charged particles (associated particles), thus to select regions and corresponding multiplicity where the contributions from jets would be minimum. Based on the value of $\Delta\phi$, we define three topological regions. Charged particles with $|\Delta\phi| < \pi/3$ belong to the towards region, and the charged particles with $|\Delta\phi| \geq 2\pi/3$ belong to the away region. The toward and away regions are expected to have a large contribution from the jet fragmentations. Moreover, the charged particles having $\pi/3 \leq |\Delta\phi| < 2\pi/3$ belong to the transverse region, where the contributions from the jet fragmentations are expected to be minimal and primarily dominated by underlying event activity. Thus, the charged particle multiplicity in the transverse region ($N_{\rm ch}^{\rm T}$) is a good observable to quantify the UE activity in an event. We define the relative transverse activity classifier, $R_{\rm T}$, as follows:

$$R_{\rm T} = \frac{N_{\rm ch}^{\rm T}}{\langle N_{\rm ch}^{\rm T} \rangle}. \tag{2.9}$$

In Eq. 2.9, the angular brackets, $\langle \dots \rangle$, denote the event-averaged value. For the calculation of $R_{\rm T}$, we use charged particles with $|\eta| < 0.8$ and $p_{\rm T} > 0.15$ GeV/c. Only events having $p_{\rm T}^{\rm lead} > 5$ GeV/c in $|\eta| < 0.8$ are considered for the studies related to $R_{\rm T}$. From the definition, it is clear that a large value of $R_{\rm T}$ would imply the dominance of UE in contrast to events having a smaller $R_{\rm T}$ value.

2.3.5 Charged Particle Flattenicity ($\rho_{\rm ch}$)

The distribution of transverse momentum in a $\eta - \phi$ region is expected to be uniform when the event is isotropic and dominated by soft-QCD processes. The uniformity of $p_{\rm T}$-distribution can be measured by dividing the $\eta - \phi$ region in a (10×10) grid. If the sum of transverse momenta of charged particles in each cell of $\eta - \phi$ is denoted as $p_{\rm T}^{\rm cell}$, one can quantify the uniformity of an event through charged particle flattenicity, as follows [40]:

$$\rho_{\rm ch} = \frac{\sigma_{p_{\rm T}^{\rm cell}}}{\langle p_{\rm T}^{\rm cell} \rangle}, \tag{2.10}$$

Here, $\langle p_{\rm T}^{\rm cell} \rangle$, and $\sigma_{p_{\rm T}^{\rm cell}}$ are the average and standard deviation of $p_{\rm T}^{\rm cell}$ distribution, calculated as follows.

$$\langle p_{\rm T}^{\rm cell} \rangle = \frac{\sum_i^{N_{\rm cell}} p_{\rm T}^{\rm cell,i}}{N_{\rm cell}}, \tag{2.11}$$

and

$$\sigma_{p_{\rm T}^{\rm cell}} = \sqrt{\frac{\sum_i^{N_{\rm cell}} (p_{\rm T}^{\rm cell,i} - \langle p_{\rm T}^{\rm cell} \rangle)^2}{N_{\rm cell}}} \tag{2.12}$$

It is worth mentioning that, for the events dominated with jet signals, the corresponding spread in $p_{\rm T}^{\rm cell}$ would be larger, which can lead to a large value of $\sigma_{p_{\rm T}^{\rm cell}}$. Further, the presence of jet signals in these events would also lead to a rise in measured $\langle p_{\rm T}^{\rm cell} \rangle$ value; however, the rise in $\sigma_{p_{\rm T}^{\rm cell}}$ would dominate over corresponding rise in $\langle p_{\rm T}^{\rm cell} \rangle$ for the events dominated by jet signals during the calculations of charged particle flattenicity, shown in Eq. (2.10).

In ALICE3, tracking and particle identification (PID) capabilities can go up to $|\eta| < 4$; thus, $\langle p_{\rm T}^{\rm cell} \rangle$ and $\sigma_{p_{\rm T}^{\rm cell}}$ are estimated from the charged particles in ALICE 3 pseudorapidity acceptance. However, the current PID tracking capabilities of ALICE at LHC and STAR at RHIC are limited to the central pseudorapidity region, i.e., $|\eta| < 1.0$. Moreover, the measurement of physics observables is significantly affected by autocorrelation bias when the event classifier is measured in a similar pseudorapidity region as the physics observable. In most of these experiments, the event classification is often performed based on charged particle multiplicity in the forward rapidity region, which can significantly reduce the autocorrelation bias. However, these forward detectors do not allow the measurement of particle transverse momentum. Thus, a redefinition of charged particle flattenicity is necessary to cope with the current detector scenario, as follows:

$$\rho_{\rm ch} = \frac{\sqrt{\sum_i (N_{\rm ch}^{\rm cell,i} - \langle N_{\rm ch}^{\rm cell} \rangle)^2 / N_{\rm cell}^2}}{\langle N_{\rm ch}^{\rm cell} \rangle}. \tag{2.13}$$

Here, $N_{\rm ch}^{\rm cell}$ is the number of charged particles in each cell measured in a (8×8) in $(\eta - \phi)$ space. Here, $N_{\rm ch}^{\rm cell}$ is calculated in the V0 acceptance region of ALICE. Here, the lower limit, i.e., $\rho_{\rm ch} \to 0$, implies that the events are isotropic and $\rho_{\rm ch} \to 1$ corresponds to the jetty events. To be consistent with the definition of event shape classifiers used in this chapter, we represent the results as a function of $(1 - \rho_{\rm ch})$, where $(1 - \rho_{\rm ch}) \to 0$ and 1 correspond to the jetty and isotropic limit, respectively.

Table 2.2 shows the event selection cuts corresponding to percentile bins for each event shape classifier used in this study. The table represents the cuts only for the PYTHIA8 color ropes tune in pp collisions at $\sqrt{s} = 13$ TeV. Figure 2.3 shows the correlation between different event classifiers and average charged-particle multiplicity measured in

Table 2.2: Selection cuts in terms of percentiles for different event classifiers in pp collisions at $\sqrt{s} = 13$ TeV using PYTHIA 8 Color Ropes [57].

Percentile (%)	N_{mpi}	$N_{\mathrm{ch}}^{\mathrm{mid}}$	$N_{\mathrm{ch}}^{\mathrm{fwd}}$	S_{T}	S_0	$S_0^{p_{\mathrm{T}}=1}$	$N_{\mathrm{ch}}^{\mathrm{T}}$	1-ρ_{ch}
0 - 0.1	23 - 35	54 - 150	120 - 250	0.98 - 1	0.92 - 1	0.94 - 1	26 - 60	0.91 - 1
0.1 - 1	18 - 23	40 - 54	96 - 120	0.96 - 0.98	0.88 - 0.92	0.91 - 0.94	20 - 26	0.90 - 0.91
1 - 5	14 - 18	29 - 40	74 - 96	0.91 - 0.96	0.82 - 0.88	0.87 - 0.91	15 - 20	0.88 - 0.90
5 - 10	11 - 14	23 - 29	62 - 74	0.88 - 0.91	0.78 - 0.82	0.84 - 0.87	13 - 15	0.87 - 0.88
10 - 20	8 - 11	17 - 23	47 - 62	0.82 - 0.88	0.72 - 0.78	0.79 - 0.84	10 - 13	0.85 - 0.87
20 - 30	5 - 8	13 - 17	37 - 47	0.78 - 0.82	0.67 - 0.72	0.75 - 0.79	9 - 10	0.83 - 0.85
30 - 40	4 - 5	10 - 13	30 - 37	0.73 - 0.78	0.62 - 0.67	0.72 - 0.75	7 - 9	0.81 - 0.83
40 - 50	3 - 4	8 - 10	24 - 30	0.68 - 0.73	0.56 - 0.62	0.68 - 0.72	6 - 7	0.79 - 0.81
50 - 70	2 - 3	5 - 8	16 - 24	0.59 - 0.68	0.46 - 0.56	0.59 - 0.68	4 - 6	0.74 - 0.79
70 - 100	0 - 2	1 - 5	1 - 16	0 - 0.59	0 - 0.46	0 - 0.59	0 - 4	0 - 0.74

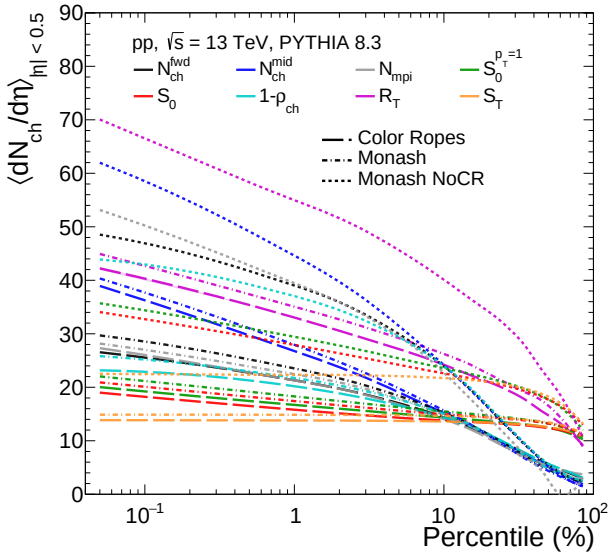

Figure 2.3: Correlation of different event classifiers with average charged-particle multiplicity measured in $|\eta| < 0.5$, i.e., $\langle dN_{\rm ch}/d\eta\rangle_{|\eta|<0.5}$, in pp collisions at $\sqrt{s} = 13$ TeV using PYTHIA8 Color Ropes, Monash and Monash NoCR [57].

$|\eta| < 0.5$, i.e., $\langle dN_{\rm ch}/d\eta\rangle_{|\eta|<0.5}$, in pp collisions at $\sqrt{s} = 13$ TeV using different tunes of PYTHIA8. As one moves from lower to higher percentiles of event classifiers, a decrease in $\langle dN_{\rm ch}/d\eta\rangle_{|\eta|<0.5}$ is observed. $\langle dN_{\rm ch}/d\eta\rangle_{|\eta|<0.5}$ changes very weakly when event selection is performed based on S_0, $S_0^{p_{\rm T}=1}$ and $S_{\rm T}$ for all the tunes of PYTHIA8 shown in Fig. 2.3. It is interesting to note that, out of other tunes shown in Fig. 2.3, all the event classifiers in the lowest percentiles for Monash NoCR possess higher values of $\langle dN_{\rm ch}/d\eta\rangle_{|\eta|<0.5}$ as compared to Monash and Color Ropes. In contrast, Color Ropes tune of PYTHIA8 shows the lowest value of $\langle dN_{\rm ch}/d\eta\rangle_{|\eta|<0.5}$ in the lowest percentile class. This is because, without CR, the individual partonic interactions are independent and lead to large multiplicity in the final state. In contrast, in the presence of CR, partons from individual partonic interactions can color connect, leading to the hardening of $p_{\rm T}$-spectra at the cost of final state particle multiplicity. Moreover, the presence of Rope Hadronisation in Color Ropes tune enhance the production of baryons and strange hadrons which further reduces the final state multiplicity. The requirements of $p_{\rm T}^{\rm lead} > 5$ GeV/c for $R_{\rm T}$ case selects the harder events, where jet-fragmentation contributes to the particle production, and we observe a slightly higher multiplicity in the highest percentile classes as compared to the event classifiers that do not possess such cuts. Similarly for S_0, $S_0^{p_{\rm T}=1}$, the requirements

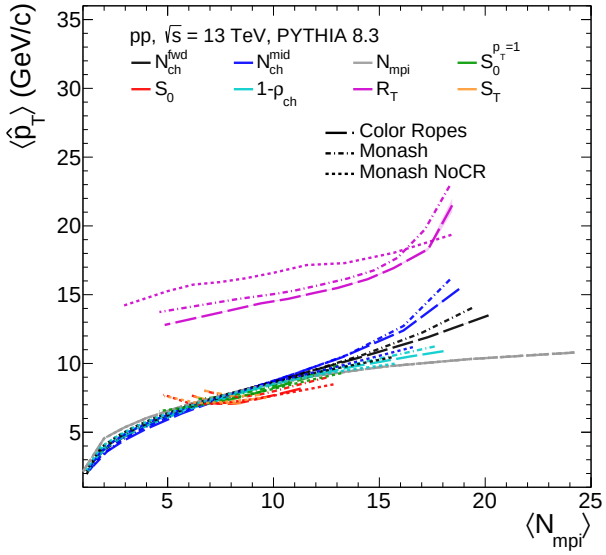

Figure 2.4: Correlation of $\langle N_{\rm mpi}\rangle$ and $\langle \hat{p}_{\rm T}\rangle$ for event selection with different event shape classifiers in pp collisions at $\sqrt{s}$ = 13 TeV using PYTHIA8 Color Ropes, Monash and Monash NoCR [57].

of $N_{\rm ch}^{\rm mid} > 10$ leads to a larger value of $\langle dN_{\rm ch}/d\eta\rangle_{|\eta|<0.5}$ in the highest percentile classes.

2.4 Results and Discussions

We start the section with measuring the Correlation between average number of MPI ($\langle N_{\rm mpi}\rangle$) and average transverse momentum transfer between hardest parton-parton interactions ($\langle \hat{p}_{\rm T}\rangle$) for different event classifiers in pp collisions using PYTHIA8 Color Ropes, Monash and Monash NoCR in Fig. 2.4. Among all the classifiers used in this study, event selection with $R_{\rm T}$ selects the hardest events, which is evident as it requires events to have at least one charged particle with $p_{\rm T} > 5$ GeV/c, which biases the sample towards the hard events. On the other hand, event classifiers such as, S_0, $S_0^{p_{\rm T}=1}$ and $S_{\rm T}$ covers a very small region in both $\langle N_{\rm mpi}\rangle$ and $\langle \hat{p}_{\rm T}\rangle$. Further, classifiers based on charged particle multiplicity, such as $N_{\rm ch}^{\rm mid}$ and $N_{\rm ch}^{\rm fwd}$ cover a large range of $\langle N_{\rm mpi}\rangle$, however, they are affected by hard events towards large $\langle N_{\rm mpi}\rangle$ regions. Finally, event selections based on $(1-\rho_{\rm ch})$ are found to follow event selection based on $N_{\rm mpi}$ closely while avoiding the hard events.

The definition of some of these event-shape observables develops a selection bias in the measurements, which needs to be properly investigated in order to understand the

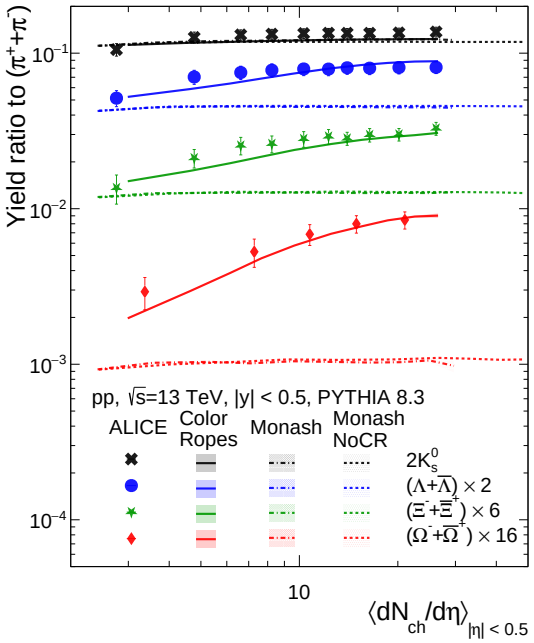

Figure 2.5: Strange hadron yield ratios to pions as a function of $\langle dN_{\rm ch}/d\eta\rangle_{|\eta|<0.5}$ in pp collisions using at $\sqrt{s} = 13$ TeV using Color Ropes, Monash and Monash NoCR tunes of PYTHIA8 [57] compared with corresponding measurements of ALICE experiments from Ref. [28].

interplay of different biases and underlying event activity on the production of different strange hadrons. This motivates us to study event shape dependent production of the strange hadrons such as $K^0_{\rm S}$, ϕ mesons, and $(\Lambda + \bar{\Lambda})$, $(\Xi^- + \bar{\Xi}^+)$ and $(\Omega^- + \bar{\Omega}^+)$ baryons, which will be often referred to as Λ, Ξ and Ω, respectively, throughout the chapter.

It is also equally important to tune the models to match the experimental measurements in order to have a proper physical interpretation of the predictions from models. Figure 2.1 shows the ratios of strange hadrons, such as $K^0_{\rm S}$, Λ, Ξ and Ω, to pions at $|y| < 0.5$ as a function of average charged-particle multiplicity in $|\eta| < 0.5$, $\langle dN_{\rm ch}/d\eta\rangle_{|\eta|<0.5}$, with events selection based on $N^{\rm fwd}_{\rm ch}$ pp collisions using at $\sqrt{s} = 13$ TeV using Color Ropes, Monash and Monash NoCR tunes of PYTHIA8 [57] compared with corresponding measurements of ALICE experiment from Ref. [28]. The yield ratios of strange hadron to pions from the ALICE experiment show a rise with the increase in $\langle dN_{\rm ch}/d\eta\rangle_{|\eta|<0.5}$. This behavior is prominent for Ω, and Ξ, while weak for Λ and absent for $K^0_{\rm S}$. The slope of the rise of yield ratios of strange hadrons to pions with $\langle dN_{\rm ch}/d\eta\rangle_{|\eta|<0.5}$ depends upon

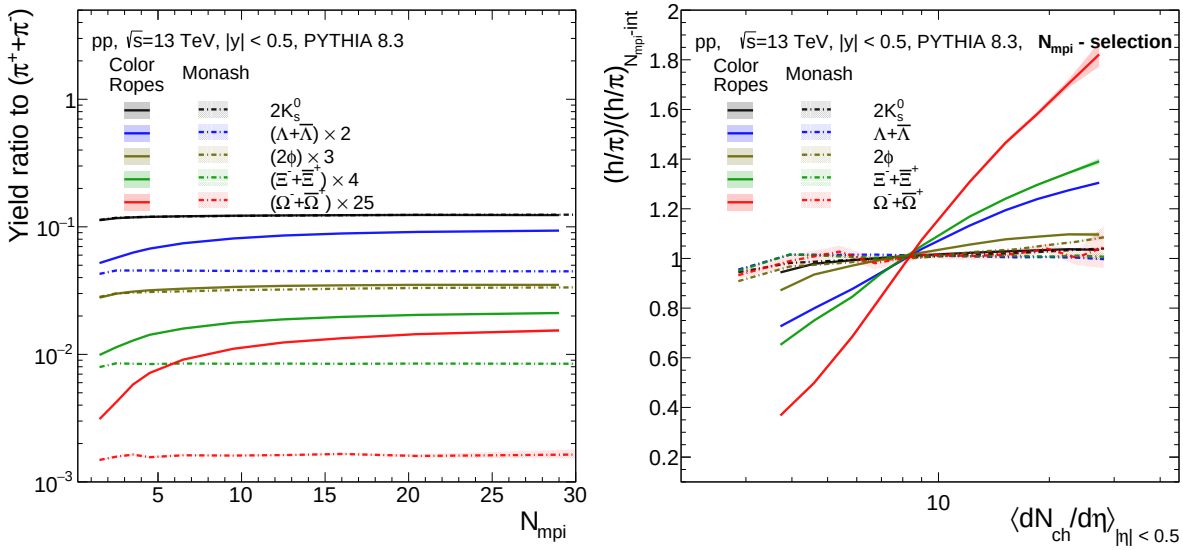

Figure 2.6: Strange hadron to pion yield ratios as a function of N_{mpi} (left) and self-normalised strange hadron to pion ratios as a function of $\langle dN_{\mathrm{ch}}/d\eta\rangle_{|\eta|<0.5}$ with event selection based on N_{mpi} (right) in pp collisions at $\sqrt{s} = 13$ TeV using Color Ropes and Monash tunes of PYTHIA 8 [57].

the number of valence strange quarks that constitute the strange hadron. Interestingly, PYTHIA8 with color ropes explains the experimental measurements quantitatively, while PYTHIA8 with Monash and Monash NoCR fails to explain both quantitative and qualitative trend of yield ratios of strange hadrons to pions as a function of $\langle dN_{\mathrm{ch}}/d\eta\rangle_{|\eta|<0.5}$. In both Monash and Monash NoCR, the yield ratios of strange baryons to pions are significantly diminished as compared to Color Ropes due to the absence of physical mechanisms responsible for multi-strange baryon production where only a statistical production of strange hadrons is possible. This is why K^0_S/π from Monash and Monash NoCR overlaps with that of Color Ropes. Thus, in PYTHIA8, rope hadronisation is crucial to explain the strange hadron production observed in experiments. Since the strange hadron yield ratios to pions from PYTHIA8 Monash and Monash NoCR overlap with each other, the further results discussed in this chapter will be limited to PYTHIA8 Color Ropes and Monash only.

Now, since it is clear that PYTHIA8 can explain the experimental production of strange hadrons through rope hadronisation, we explore the event shape dependence. We

begin with $N_{\rm mpi}$ dependence of strange hadron to pion ratios shown in the left panel of Fig. 2.6. Further, the self-normalised yield ratios of strange hadrons to pions as a function of $\langle dN_{\rm ch}/d\eta\rangle_{|\eta|<0.5}$ is shown in the right panel of Fig. 2.6, where the event selection is performed based on different percentiles of $N_{\rm mpi}$. The study of strange hadron production as a function of $N_{\rm mpi}$ is crucial and can serve as a benchmark for other experimentally measurable event classifiers. Moreover, the studies based on $N_{\rm mpi}$ would provide the depth of selection biases that affect the strangeness production with event selections based on other event classifiers. From Fig. 2.6, it is clear that MPI plays an important role in strange hadron production for PYTHIA8 Color Ropes when RH is enabled. The production of strange baryons, such as Λ, ϕ, Ξ, and Ω, with respect to charged pions, in contrast to strange meson $K^0_{\rm S}$ and ϕ, increase with an increase in $N_{\rm mpi}$. The rise with $N_{\rm mpi}$ is more prominent for baryons with a higher number of valence strange quarks such as Ω and Ξ. Further, after a certain value of $N_{\rm mpi}$, the yield ratios to pions start to saturate, which again depends upon the strange quantum number of the hadron. Thus it is clear that the effect of RH is enhanced for events with large $N_{\rm mpi}$ as a higher value of $N_{\rm mpi}$ would imply large number of color rope formation leading to large strange and multi-strange baryons. A similar observation can be made from the right panel of Fig. 2.6, where a rise in the self-normalised yield of strange hadrons to pions with $\langle dN_{\rm ch}/d\eta\rangle_{|\eta|<0.5}$ is observed for PYTHIA8 Color Ropes. The rising trend is absent in Monash. Interestingly, for PYTHIA8 Color Ropes, the self-normalised yield shows a near linear rise with $\log(\langle dN_{\rm ch}/d\eta\rangle_{|\eta|<0.5})$, the slope of while is the highest for Ω having three strange valence quarks and smallest for K^0_S. Moreover, ϕ-meson, having zero strangeness quantum number, shows a higher slope than that of K^0_S having one strange quantum number, which was not clear from the left panel of Fig. 2.6. This indicates that the strangeness production with respect to charged pions is stronger for baryons than mesons, and it also depends upon the strange quark/antiquark content of the meson rather than the total strangeness quantum number of the meson under consideration.

Figure 2.7 shows the strange hadron to pion yield ratios versus $N^{\rm mid}_{\rm ch}/\langle N^{\rm mid}_{\rm ch}\rangle$ (left) and self-normalised strange hadron to pion ratios as a function of $\langle dN_{\rm ch}/d\eta\rangle_{|\eta|<0.5}$ with event selection based on $N^{\rm mid}_{\rm ch}$ (right) in pp collisions at $\sqrt{s} = 13$ TeV using Color Ropes and Monash tunes of PYTHIA 8 [57]. For PYTHIA8 Color Ropes, the left panel of Fig. 2.7

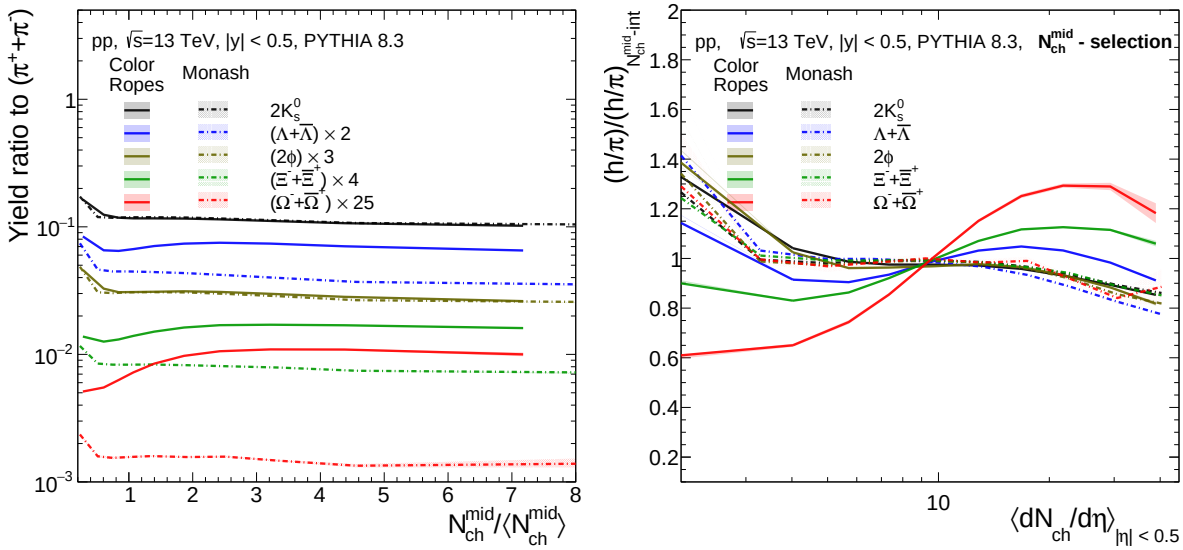

Figure 2.7: Strange hadron to pion yield ratios as a function of $N_{\rm ch}^{\rm mid}/\langle N_{\rm ch}^{\rm mid}\rangle$ (left) and self-normalised strange hadron to pion ratios as a function of $\langle dN_{\rm ch}/d\eta\rangle_{|\eta|<0.5}$ with event selection based on $N_{\rm ch}^{\rm mid}$ (right) in pp collisions at $\sqrt{s} = 13$ TeV using Color Ropes and Monash tunes of PYTHIA 8 [57]

shows a rise in the strange hadron to pion ratio with an increase in $N_{\rm ch}^{\rm mid}/\langle N_{\rm ch}^{\rm mid}\rangle$ for $N_{\rm ch}^{\rm mid}/\langle N_{\rm ch}^{\rm mid}\rangle \geq 1$, which is absent for PYTHIA8 Monash. This is similar to observations made in the left panel of Fig. 2.6, and is attributed to the strong Correlation of $N_{\rm ch}^{\rm mid}$ with $N_{\rm mpi}$, shown in Fig 2.4. Moreover, towards $N_{\rm ch}^{\rm mid}/\langle N_{\rm ch}^{\rm mid}\rangle \lesssim 1$, one observes a rise in the ratio of strange hadron yield to pions with a decrease in $N_{\rm ch}^{\rm mid}/\langle N_{\rm ch}^{\rm mid}\rangle$. In PYTHIA8 Color Ropes, this behaviour is found to have a dependence on the mass of the strange hadrons for color being strongest for $K_{\rm S}^0$ and weakest for Ξ and absent for Ω, which could be attributed to the dominance of jet signals in low multiplicity events.

In the right panel of Fig. 2.7, one finds a peculiar behaviour of self-normalised yield ratios of strange hadrons to pions as a function of $\langle dN_{\rm ch}/d\eta\rangle_{|\eta|<0.5}$ for event selection based on $N_{\rm ch}^{\rm mid}$. For PYTHIA8 Monash, with an increase in $\langle dN_{\rm ch}/d\eta\rangle_{|\eta|<0.5}$, the self normalised yield ratios to pions decrease irrespective of the hadron kind, this could be attributed to the auto-correlation bias in $N_{\rm ch}^{\rm mid}$ which arises because of measuring the hadrons and estimator in a similar rapidity region. A higher value of $N_{\rm ch}^{\rm mid}$ would indicate a large number of charged pions in the denominator, which leads to a decrease in the self-

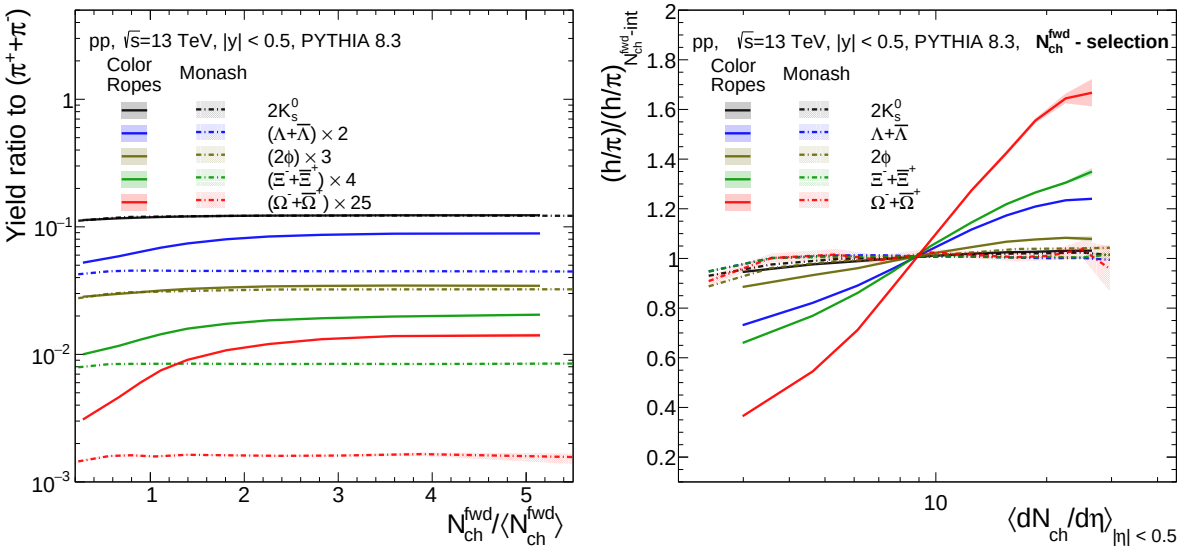

Figure 2.8: Strange hadron to pion yield ratios as a function of $N_{\rm ch}^{\rm fwd}/\langle N_{\rm ch}^{\rm fwd}\rangle$ (left) and self-normalised strange hadron to pion ratios as a function of $\langle dN_{\rm ch}/d\eta\rangle_{|\eta|<0.5}$ with event selection based on $N_{\rm ch}^{\rm fwd}$ (right) in pp collisions at $\sqrt{s} = 13$ TeV using Color Ropes and Monash tunes of PYTHIA 8 [57].

normalised yield ratios of strange hadrons to charged pions. Similar behaviour is observed in PYTHIA8 Color Ropes for K^0_S and ϕ mesons. On the other hand, for PYTHIA8 Color Ropes, the self-normalised yield ratios of strange and multi-strange baryons to pions do not follow the usual trend discussed above. For Λ, the self-normalised yield ratio to pions slightly increases in $7 \lesssim \langle dN_{\rm ch}/d\eta\rangle_{|\eta|<0.5} \lesssim 15$. This is followed by a decrease in the lower and high $\langle dN_{\rm ch}/d\eta\rangle_{|\eta|<0.5}$ regions. This is attributed to the competing effects of RH and autocorrelation bias due to event selection. The dominating contributions to Ξ/π and Ω/π from RH, self-normalised yield ratios to pions increase with increased charged particle multiplicity except for the highest multiplicity class, where the selection bias is the largest.

The left panel of Fig. 2.8 shows strange hadron to pion yield ratios as a function of $N_{\rm ch}^{\rm fwd}/\langle N_{\rm ch}^{\rm fwd}\rangle$ while the right panel shows the self-normalised strange hadron to pion ratios as a function of $\langle dN_{\rm ch}/d\eta\rangle_{|\eta|<0.5}$ with event selection based on $N_{\rm ch}^{\rm fwd}$ (right) in pp collisions at $\sqrt{s} = 13$ TeV using Color Ropes and Monash tunes of PYTHIA 8 [57]. It is interesting to see that the event selection based on $N_{\rm ch}^{\rm fwd}$ follows quite closely to the measurements

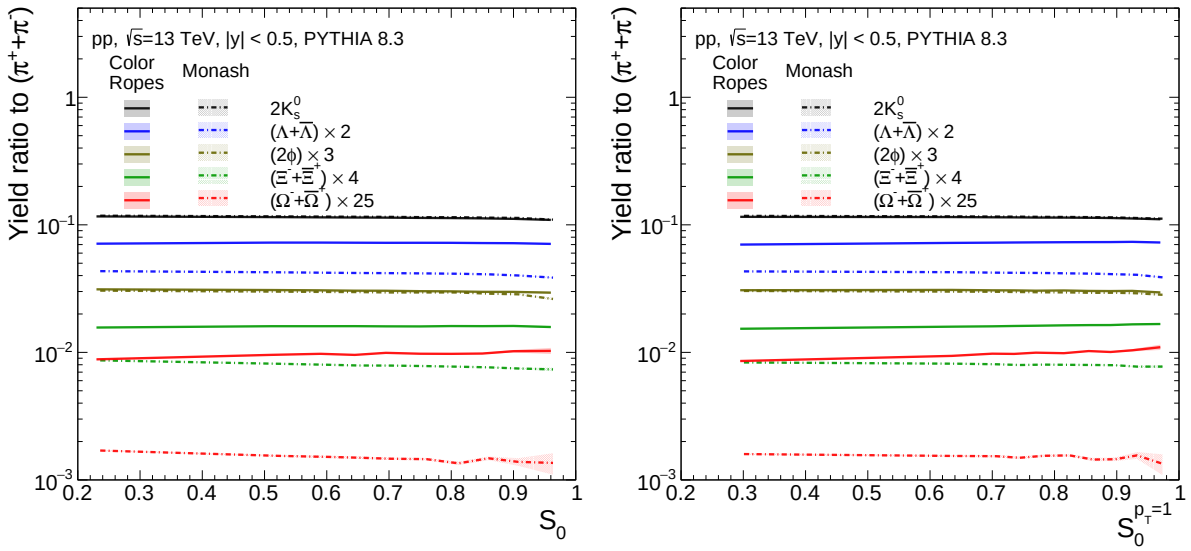

Figure 2.9: Yield ratios of strange hadrons to pions as a function of S_0 (left) and $S_0^{p_{\mathrm{T}}=1}$ (right) in pp collisions at $\sqrt{s}$ = 13 TeV using Color Ropes and Monash tunes of PYTHIA 8 [57].

with N_{mpi} shown in Fig. 2.6, except for a saturation behaviour in the production of self-normalised yield ratios of strange hadrons to pion for PYTHIA8 Color Ropes which shows a saturation behaviour at large $\langle dN_{\mathrm{ch}}/d\eta\rangle_{|\eta|<0.5}$ for ϕ and Λ and is absent for Ω and Ξ. This saturation behaviour of Λ and ϕ can be attributed to selection bias towards charged particles while affecting the neutral particle production. Another possible speculation is that since Ξ and Ω are highly affected by RH, the effects of selection bias are not visible for these particles.

Fig. 2.9 shows the strange hadron to charged pion yield ratio as a function of S_0 (left) and $S_0^{p_{\mathrm{T}}=1}$ (right) in pp collisions at $\sqrt{s}$ = 13 TeV using Color Ropes and Monash tunes of PYTHIA 8 [57]. As already discussed and shown in Ref. [33], $p_{\mathrm{T}}-$weighted S_0 estimator introduces a neutral jet bias and detector smearing effect, which is absent in $S_0^{p_{\mathrm{T}}=1}$. For PYTHIA8 Color Ropes, K^0_S/π, Λ/π, Ξ/π, and ϕ/π ratios show no dependence of S_0 and $S_0^{p_{\mathrm{T}}=1}$. On contrary, Ω/π shows a rise with increase in S_0 and $S_0^{p_{\mathrm{T}}=1}$ for PYTHIA8 Color Ropes. However, both Ξ/π and Ω/π decreases with an increase in S_0 and remains nearly unchanged with an increase in $S_0^{p_{\mathrm{T}}=1}$ for PYTHIA8 Monash. Interestingly, the yield ratios of strange hadrons to pions are comparable to the values in high multiplicity events as

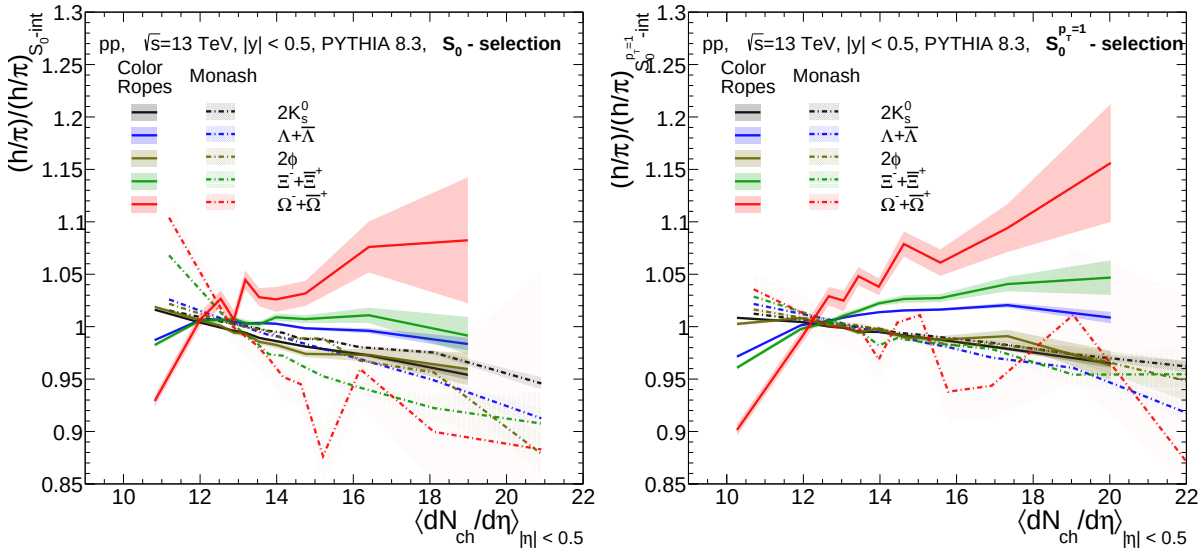

Figure 2.10: Self-normalised strange hadron to pion ratios as a function of $\langle dN_{\rm ch}/d\eta\rangle_{|\eta|<0.5}$ with event selection based on S_0 (left) and $S_0^{p_{\rm T}=1}$ (right) in pp collisions at $\sqrt{s} = 13$ TeV using Color Ropes and Monash tunes of PYTHIA 8 [57].

observed in Figs. 2.6, and 2.7, which can be the consequence of the event selection cut $N_{\rm ch}^{\rm mid} \geq 10$ for S_0 and $S_0^{p_{\rm T}=1}$.

Figure 2.10 shows the self-normalised strange hadron to pion ratios as a function of $\langle dN_{\rm ch}/d\eta\rangle_{|\eta|<0.5}$ with event selection based on S_0 (left) and $S_0^{p_{\rm T}=1}$ (right) in pp collisions at $\sqrt{s} = 13$ TeV using Color Ropes and Monash tunes of PYTHIA 8 [57]. In PYTHIA8 Color Ropes, the self-normalised yield ratio of Ω/π shows a steeper rise with $\langle dN_{\rm ch}/d\eta\rangle$ for event selection based on $S_0^{p_{\rm T}=1}$ than that of S_0. Moreover, for $S_0^{p_{\rm T}=1}$, the self-normalised yield ratio for Ξ to charged pions shows a steeper increase as a function of $\langle dN_{\rm ch}/d\eta\rangle$ than that of Λ which holds the scaling of the strangeness quantum number. Further, for ϕ and K_S^0, one finds that the self-normalised yield ratio to charged pions decreases with increase in $\langle dN_{\rm ch}/d\eta\rangle_{|\eta|<0.5}$ for event selections based on both S_0 and $S_0^{p_{\rm T}=1}$. However, the rate of this decrease is higher for S_0 than $S_0^{p_{\rm T}=1}$, which can arise as a consequence of measuring spherocity and the strange particles in similar rapidity regions. In contrast, the self-normalised yield ratios of all the strange hadrons to pions decrease with increase in $\langle dN_{\rm ch}/d\eta\rangle_{|\eta|<0.5}$ for event selection based on both S_0 and $S_0^{p_{\rm T}=1}$ with PYTHIA 8 Monash. This is similar to the observations made in Fig. 2.7, where the events are selected with

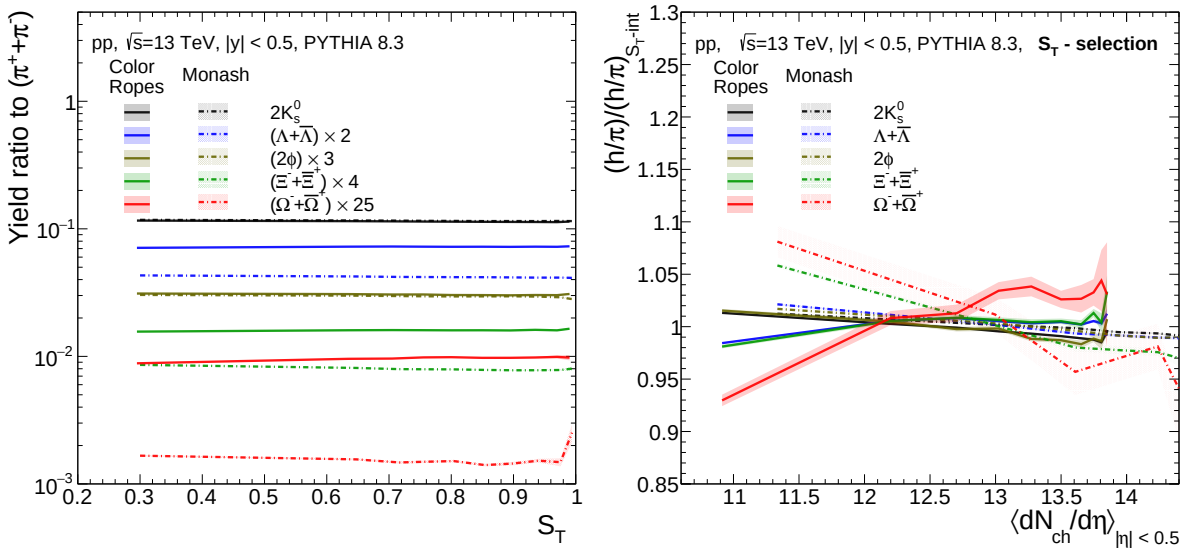

Figure 2.11: Strange hadron to pion yield ratios as a function of S_{T} (left) and self-normalised strange hadron to pion ratios as a function of $\langle dN_{\mathrm{ch}}/d\eta\rangle_{|\eta|<0.5}$ with event selection based on S_{T} (right) in pp collisions at $\sqrt{s}$ = 13 TeV using Color Ropes and Monash tunes of PYTHIA 8 [57].

$N_{\mathrm{ch}}^{\mathrm{mid}}$. This indicates that the self-normalised yield ratios of strange hadrons to pions are highly affected by the autocorrelation bias in the absence of RH. Further, the decrease of the self-normalised yield ratios of strange hadrons to pions is weaker for $S_0^{p_{\mathrm{T}}=1}$-based event selection as compared to S_0. This concludes that, for the study of strange and multi-strange hadron production in pp collisions at the LHC energies, $S_0^{p_{\mathrm{T}}=1}$ possess a small selection bias but a better observable as compared to S_0.

The left panel of Fig. 2.11 shows the yield ratios of strange hadrons to pions as a function of S_{T} in pp collisions at $\sqrt{s}$ = 13 TeV using PYTHIA 8 Color Ropes and Monash. One finds a negligible dependence of yield ratios of strange hadrons to pions as a function of S_{T} for PYTHIA 8 Color Ropes, which is similar to S_0, shown in the left panel of Fig. 2.9. In contrast, one observes a decreasing trend for yield ratios of Ξ and Ω to charged pions as a function of S_{T} for PYTHIA 8 Monash, similar to that observed in the left panel of Fig. 2.7 and Fig. 2.9. Thus, one can conclude that the isotropic events have similar behaviour of strange to pion ratio as the jetty events for event classifiers having $N_{\mathrm{ch}}^{\mathrm{mid}} \geq 10$, which makes S_0, $S_0^{p_{\mathrm{T}}=1}$ and S_{T} inefficient to study the strangeness

suppression characteristics in low multiplicity events.

The right panel of Fig. 2.11 shows self-normalised strange hadron yield ratios to pions as a function of $\langle dN_{\rm ch}/d\eta\rangle_{|\eta|<0.5}$ for event selection based on $S_{\rm T}$ in pp collisions at $\sqrt{s} = 13$ TeV using PYTHIA 8 Color Ropes and Monash. Here, similar to S_0 in the left panel of Fig. 2.10, one observes a similar enhancement trends for strange baryons and suppression trends for mesons, ϕ, and K^0_S, with a rise in $\langle dN_{\rm ch}/d\eta\rangle_{|\eta|<0.5}$ with event selection based on $S_{\rm T}$ with PYTHIA 8 Color Ropes. Moreover, with an increase in $\langle dN_{\rm ch}/d\eta\rangle_{|\eta|<0.5}$, the self-normalised yield ratios of the strange hadrons to pions decrease, which is stronger for hadrons having a larger number of strange quarks. However, the amplitudes for these enhancement or suppression trends using $S_{\rm T}$ are the smallest among all other event shapes used in this chapter.

The top panels of Fig. 2.12 show the ratios of strange and multi-strange hadrons to charged pions as a function of $R_{\rm T}$ in toward (left) and transverse (right) regions in pp collisions at $\sqrt{s} = 13$ TeV using PYTHIA 8 Color Ropes and Monash. Here, the particle measurement is restricted to $p_{\rm T} < 5$ GeV/c to avoid the trigger particle selection bias for $R_{\rm T}$ [38, 39]. The behaviour of strange particle ratios to pions is observed to be different in toward and transverse regions. In the toward the region, with the absence of auto-correlation bias, Ω/π shows a mild rise with an increase in $R_{\rm T}$ in PYTHIA 8 Color Ropes. In contrast, Ξ/π and Λ/π do not show noteworthy dependence on $R_{\rm T}$. In the transverse region, dominated with correlation bias as $R_{\rm T}$ is defined in the same region, the Ω/π enhancement is not observed in the ratios of strange hadrons to pions. Moreover, a decrease in the neutral strange hadrons to charged pion ratios, such as ϕ/π, K^0_S/π and Λ/π, is observed with an increase in $R_{\rm T}$. This effect seems to be influenced by large autocorrelation biases. Similar to S_0, $S_0^{p_{\rm T}=1}$ and $S_{\rm T}$, the enhancement of strangeness is observed to be weak with event selection based on $R_{\rm T}$, which could be attributed to the high-$p_{\rm T}$ selection of trigger particle, where one always selects high multiplicity events. The bottom panels show the self-normalised yield ratios of strange hadrons to pions as a function of $\langle dN_{\rm ch}/d\eta\rangle_{|\eta|<0.5}$ with event selection based on $R_{\rm T}$ in pp collisions at $\sqrt{s} = 13$ TeV using PYTHIA 8 Color Ropes and Monash. In the transverse region, for PYTHIA8 Color Ropes, the self-normalised yield ratios of ϕ, K^0_S and Λ to pions decrease with an increase in $\langle dN_{\rm ch}/d\eta\rangle_{|\eta|<0.5}$ with event selection based on $R_{\rm T}$ indicating the presence of

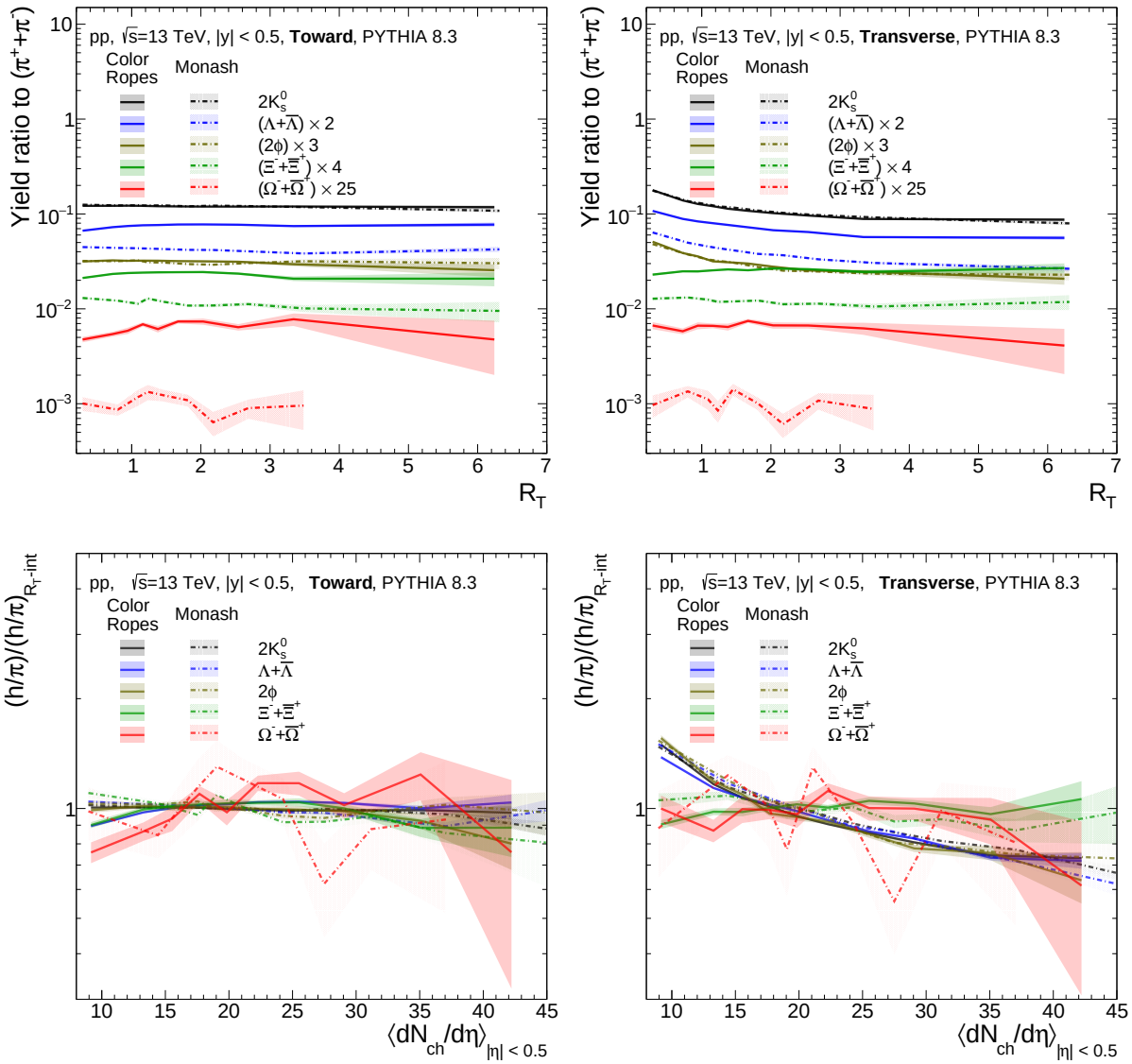

Figure 2.12: Upper panel shows the strange hadron to pion ratio in the toward (left) and transverse (right) regions as a function of R_{T}. The lower panel shows the self-normalised yield ratios of strange hadrons to pions in toward (left) and transverse (right) regions as a function of $\langle dN_{\mathrm{ch}}/d\eta \rangle_{|\eta|<0.5}$ for event selections based on R_{T} in pp collisions at $\sqrt{s} = 13$ TeV using PYTHIA8 Monash and Color Ropes [57].

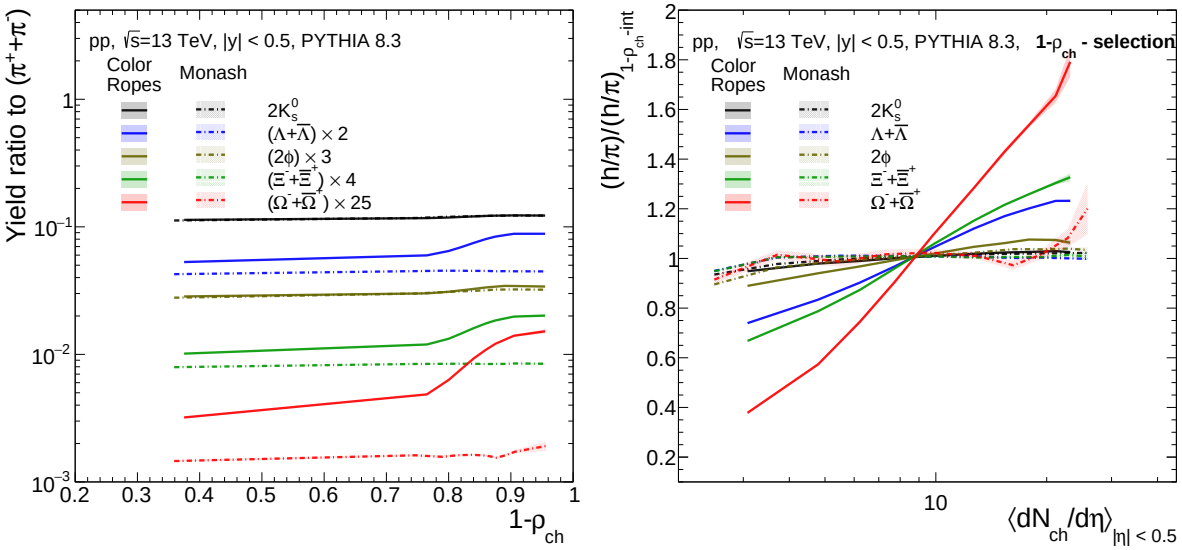

Figure 2.13: Strange hadron to pion yield ratios as a function of $(1-\rho_{\rm ch})$ (left) and self-normalised strange hadron to pion ratios as a function of $\langle dN_{\rm ch}/d\eta\rangle_{|\eta|<0.5}$ with event selection based on $(1-\rho_{\rm ch})$ (right) in pp collisions at $\sqrt{s}=13$ TeV using Color Ropes and Monash tunes of PYTHIA 8 [57].

strong autocorrelation bias. A similar feature is observed for all strange hadrons for PYTHIA8 Monash where RH is absent, which counters the selection bias in Color Ropes for Ω and Ξ.

Figure 2.13 shows the strange hadron to pion yield ratios as a function of $(1-\rho_{\rm ch})$ (left) and self-normalised strange hadron to pion ratios as a function of $\langle dN_{\rm ch}/d\eta\rangle_{|\eta|<0.5}$ for different percentiles of $(1-\rho_{\rm ch})$ (right) in pp collisions at $\sqrt{s}=13$ TeV using Color Ropes and Monash tunes of PYTHIA 8 [57]. Interestingly, both left and right panels of Fig. 2.13 show a similar behaviour of strangeness enhancement with that observed in Fig. 2.6, where events are selected based on $N_{\rm mpi}$. The only difference is that in the left panel of Fig. 2.13, the qualitative enhancement of strange hadrons is amplified in $0.75 \lesssim (1-\rho_{\rm ch}) \lesssim 0.9$, where most of the events lie. On the other hand, the self-normalised yield ratio of strange hadron production with respect to pions with event selection based on $(1-\rho_{\rm ch})$ are very close to that of $N_{\rm mpi}$, which confirms the fact that event selection based on (1-$\rho_{\rm ch}$) is not affected by selection bias and flattenicity is one of the best event shape observables at the LHC energies to study the strangeness production.

2.5 Summary

In summary, in this chapter, the production of strange hadrons with different event shape observables in proton-proton collisions at $\sqrt{s} = 13$ TeV using different tunes of PYTHIA are studied. We have studied strange hadron-to-pion yield ratios and self-normalised yield ratios of strange hadrons to pions for different event classifiers available at the LHC energies. The strange hadrons include, K^0_S, ϕ mesons, and $(\Lambda + \bar{\Lambda})$, $(\Xi^- + \bar{\Xi}^+)$ and $(\Omega^- + \bar{\Omega}^+)$ baryons. Implementation of Color Ropes in PYTHIA8 allows to describe the strange and multi-strange hadron production. In this study, event classifiers such as charged particle multiplicity at mid ($N^{\rm mid}_{\rm ch}$) and forward ($N^{\rm fwd}_{\rm ch}$) rapidity regions, number of multi-partonic interactions ($N_{\rm mpi}$), weighted and unweighted transverse spherocity (S_0, and $S_0^{p_{\rm T}=1}$), transverse sphericity ($S_{\rm T}$), relative transverse activity classifier ($R_{\rm T}$) and charged particle flattenicity ($\rho_{\rm ch}$) have been explore to probe the strange and multi-strange hadron production. Although, $N^{\rm mid}_{\rm ch}$ and $N^{\rm fwd}_{\rm ch}$ have large correlation with $N_{\rm mpi}$, they are affected by significant selection bias. Further event shape observables such as S_0, $S_0^{p_{\rm T}=1}$ and $S_{\rm T}$ are also affected by selection bias due to an implicit cut of $N^{\rm mid}_{\rm ch} \geq 10$. Further, the trigger particle selection cut of $p^{\rm lead}_{\rm T} \geq 5$ GeV/c contaminates the strange hadron production rations to pions and their self-normalised yield as a function of $R_{\rm T}$. In contrast, the strange hadron production as a function of $(1-\rho_{\rm ch})$ mimics the results based on $N_{\rm mpi}$-selections and are least affected by selection bias as compared to other experimentally measurable event classifiers. Thus, one should use charged particle flattenicity at the LHC to study strangeness production.

2.6 Outlook

This study is useful for the experimentalist to choose the best event classifier when performing the study of strangeness production, the observation of which in small systems is still a puzzle to date. Additionally, the biases discussed in this chapter for strange hadrons also affect the heavy flavour hadron production, as discussed below. Figure 2.14 shows the self-normalised yield of prompt[1] and non-prompt[2] J/ψ as a function of self-normalised

[1]Prompt J/ψ is produced directly or through decay of higher charm states, such as $\psi(2S)$ or χ_c, etc.
[2]Non-prompt J/ψ is produced through weak decay of beauty hadrons.

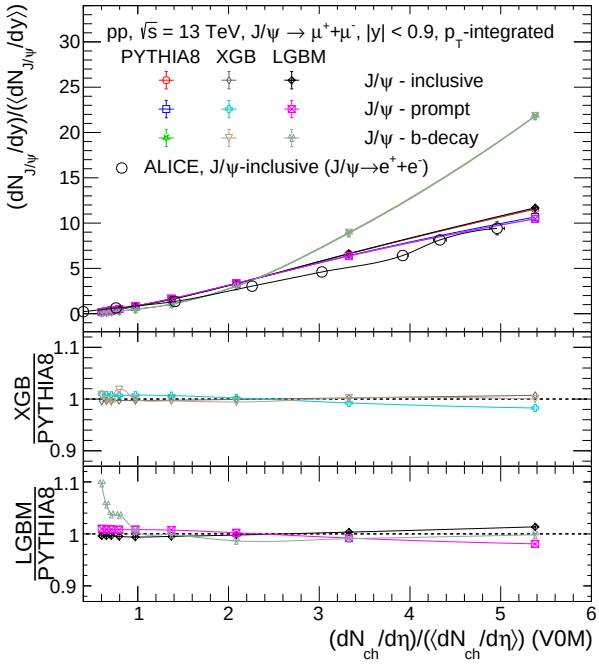

Figure 2.14: Self-normalised yield of prompt and non-prompt J/ψ $((dN_{\mathrm{J}/\psi}/dy)/\langle dN_{\mathrm{J}/\psi}/dy\rangle)$ as a function of self-normalised charged particle multiplicity $((dN_{\mathrm{ch}}/d\eta)/\langle dN_{\mathrm{ch}}/d\eta\rangle)$ in pp collisions at $\sqrt{s}$ = 13 TeV with PYTHIA8. Predictions from XGBoost and LihgtGBM models are also compared [65]. ALICE measurements are taken from Ref. [66].

charged particle multiplicity $((dN_{\mathrm{ch}}/d\eta)/\langle dN_{\mathrm{ch}}/d\eta\rangle)$ using PYTHIA8 and compared with ALICE measurements for prompt case in pp collisions at $\sqrt{s} = 13$ TeV. The multiplicity selection is performed with $N_{\mathrm{ch}}^{\mathrm{fwd}}$ (or V0M, as shown in the figure), while J/ψ is measured in the midrapidity to avoid the selection biases as shown in previous sections of this chapter. PYTHIA8 results for prompt J/ψ slightly overestimate the experimental measurement; however, it provides a good qualitative description of the multiplicity-dependent yield of J/ψ. As one can see, the production of J/ψ increases stronger than linear with charged-particle multiplicity. These effects are even stronger for the non-prompt cases. This stronger-than-linear rise of J/ψ for prompt and non-prompt cases is still not understood well in experiments and requires the help of new event shape observables with new measurement techniques such as Machine Learning, which are useful for precise measurements and accurate identifications of particle species, as shown in Fig. 2.14. Thus, the present study of using event shape observables for strangeness production can be extended

in experiments to study charm production, which are excellent probes for QCD medium formation in heavy-ion collisions.

Chapter 3

ALICE: A Large Ion Collider Experiment

Since the beginning of human existence, the journey of homo sapiens has been driven by necessity, curiosity and the desire to understand the nature around us. From the moment of harnessing fire by striking the stones together to understanding the fundamental constituents of matter by colliding protons at nearly the speed of light, the human story has been one of exploration and discovery. Each page in this story has deepened our understanding of the universe, and yet a lot still remains to be explored. The pursuit of knowledge and understanding of the universe by modern civilisation has led to the building of a scientific and engineering marvel, the Large Hadron Collider, at CERN, Geneva, Switzerland. LHC is currently the world's largest and most powerful accelerator, which was inaugurated on 10 September 2008. A Large Ion Collider Experiment (ALICE) is one of the experiments at LHC with a focus to study the properties of QGP, a state of QCD matter under high temperature and energy density environment, produced in ultra-relativistic nuclear collisions. ALICE has been operational since November 2009 and has been working to date with a few upgrades [67].

This chapter presents a brief discussion on the ALICE detectors at the LHC. The chapter is organised as follows. The chapter starts with a discussion on LHC complex in Section 3.1. Section 3.2 provides a brief introduction to ALICE detectors with a focused discussions on ITS, TPC, and FV0. Finally, Section 3.3 describes the ALICE computing and analysis framework briefly.

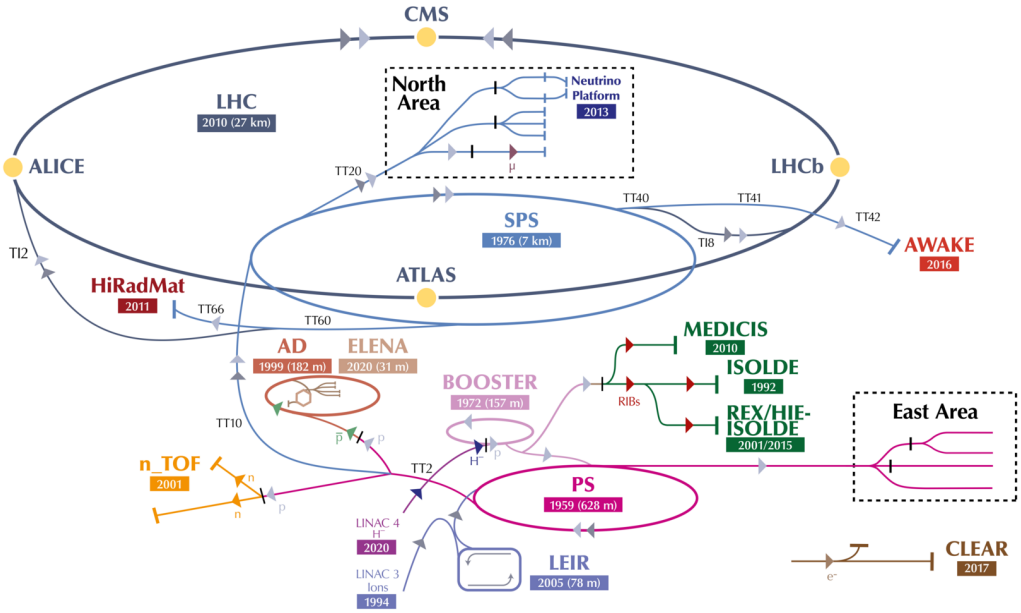

Figure 3.1: Schematic view of CERN accelerator complex [69].

3.1 The Large Hadron Collider

The LHC features a 26.7 km circular tunnel, at a depth of 47-170 m across the Switzerland and France border [68]. It is capable of accelerating protons or heavy ions, where two beams of the same or different species can be accelerated in opposite directions. LHC is designed to achieve a maximum of 14 TeV (by design)/13.6 TeV (achieved to date) centre of mass energy for protons. The former corresponds to $\sqrt{s_{\rm NN}} = 5.5$ TeV in Pb–Pb collisions. In Run3, LHC is able to reach up to $\sqrt{s_{\rm NN}} = 5.36$ TeV in Pb–Pb collisions. Figure 3.1 shows the schematic view of the LHC accelerator complex at CERN. Before the particles are injected into the LHC, they are accelerated sequentially through several other accelerators. First of all, a strong electric field is used to strip off the electrons from atomic nuclei. The proton bunches are then accelerated through LINAC2 (accelerates to 50 MeV energy), PS booster (accelerates to 1.4 GeV energy), PS (accelerates up to 25 GeV energy) and SPS (accelerates to 450 GeV energy) before being injected into LHC. In contrast, the bunches of heavy ions have to be accelerated through LINAC3, LEIR, PS, and SPS before injection into the LHC. This is pictorially represented in Fig. 3.1. The beams are injected into the LHC to move clockwise and anti-clockwise for hours under normal operating conditions.

The beams of ions thus injected into LHC travel close to the speed of light in opposite directions in two separate tubes, known as beam pipes, which are kept at ultra-high vacuum. While the electric field accelerates the beams towards the final beam energy, strong magnetic fields are generated under controlled environments through the superconducting electromagnets to guide the beams along the accelerator ring. Instantaneous luminosity (L) plays a vital role in ensuring a high collision rate at the collision points. The LHC is designed to provide a maximum of 10^{34} (10^{27}) $\mathrm{cm}^{-2}\mathrm{s}^{-1}$ for pp (heavy-ion) collisions. There are four interaction points where the collisions occur, which constitute four major detectors having different physics goals, which are discussed below.

- **ATLAS (A Toroidal LHC Apparatus):** ATLAS is the largest particle detector at the LHC, which is designed to study the physics beyond the standard model, which includes, but is not limited to, dark matter, supersymmetric particles, search for Higgs boson, etc.
- **CMS (Compact Muon Solenoid):** The purpose of CMS is similar to that of ATLAS.
- **LHCb (Large Hadron Collider beauty):** The LHCb detector covers the forward rapidity regions and is built to study physics related to beauty hadron production, which includes charge parity (CP) violation and rare decays.
- **ALICE (A Large Ion Collider Experiment):** ALICE experiments at the LHC have exceptional particle identification capabilities down to zero transverse momenta, suited to study the formation of QGP in nuclear collisions.

In the following section, we shall briefly discuss the ALICE detector.

3.2 ALICE at the LHC

ALICE is a heavy-ion detector at the LHC with a focus on studying the QCD sector of the Standard Model of particle physics. It has a dimension of $26 \times 16 \times 16$ m^3 while weighing approximately 10,000 tons. Since, ALICE focuses on studying the formation of QGP in

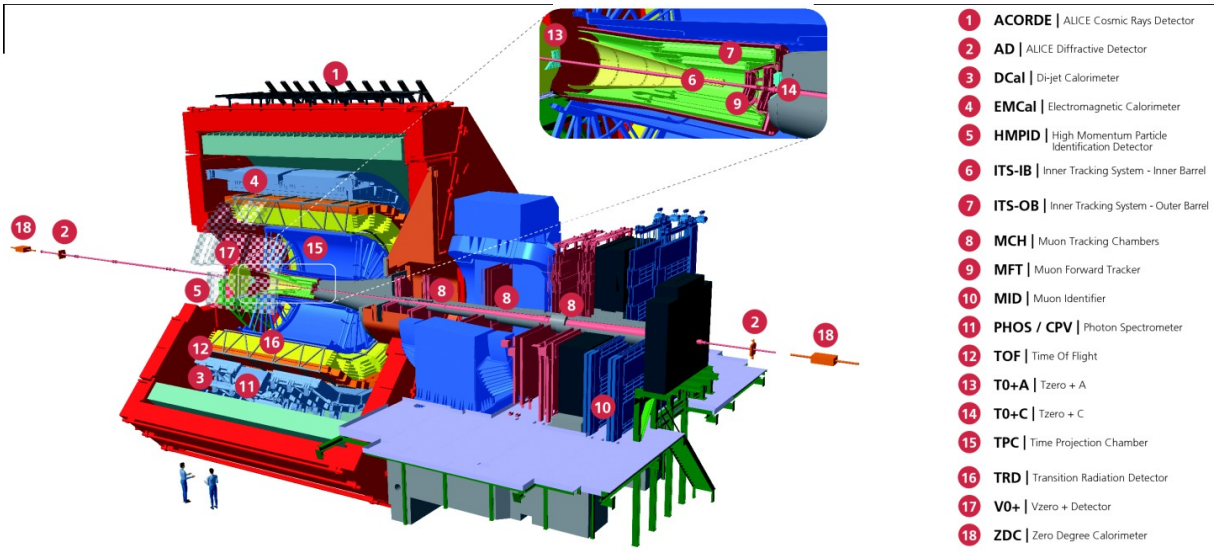

Figure 3.2: Schematic layout of ALICE detector during Run3 data-taking of LHC [70].

heavy-ion collisions, the signatures of which are prominent in the low to intermediate p_{T}-regions, the ALICE detector is equipped with excellent particle identification and tracking down to $p_{\mathrm{T}} \to 0.1$ GeV/c.

Figure 3.2 shows various detectors in ALICE, which can be divided into two groups as follows.

1. **Central barrel detectors:** The central barrel detectors (CBT) cover the mid pseudo-rapidity region ($|\eta| < 0.9$) and 2π azimuthal region. The central barrel detectors are primarily used for tracking, vertexing, particle identification, etc. The CBT consists of Inner Tracking System (ITS) [71], Time Projection Chamber (TPC) [72], Transition Radiation Detector (TRD) [73], Time of Flight (TOF) [74] detector, High Momentum Particle Identification detector (HMPID) [75], Photon Spectrometer (PHOS) [76], Electro-magnetic calorimeter (EMCAL) [77], and ALICE Cosmic Ray Detector (ACORDE) [78]. The position of these detectors can be seen in Fig. 3.2.

2. **Forward detectors:** The forward detectors at ALICE consist of a set of Fast Interaction Trigger (FIT) detectors, Muon Forward Tracker (MFT), and Muon Spectrometer [70]. The FIT detector [79] consists of three sub-detectors, such as Forward

Time Zero (FT0) [1], Forward VZERO (FV0) [2], and Forward Diffractive Detector (FDD). These three sub-detectors with different technologies are stationed at forward and backwards rapidity regions. The online functionality of these sub-detectors involves luminosity monitoring, minimum bias, vertex and centrality triggering [70, 79]. The offline FIT delivers the precise time for TOF-based PID, measurement of diffractive cross-section, and centrality determination [70, 79]. The primary goal of MFT is to improve the pointing resolution of muons, the details of which can be found in Ref. [70]. The muon spectrometer situated in the forward rapidity regions is used to study the heavy-quark vector meson resonances as well as the ϕ meson through their $\mu^+\mu^-$ decay channels [80].

A right-handed reference coordinate system is used globally within ALICE, where the z-axis points along the beam line, in the direction away from muon detectors, the y-axis points vertically upwards, and the x-axis points horizontally towards the centre of LHC. The interaction point is considered as the centre of the coordinate system [70]. The direction of the muon arm from the centre is referred to as the C side, and the direction towards the FV0 is the A side of the detector. In the following sections, ALICE ITS, TPC, and FV0 are discussed in detail, which are used for the analysis presented in Chapter 4 of this thesis.

3.2.1 Inner Tracking System (ITS)

ITS is the closest to the beam pipe and is primarily responsible for the measurement of primary and secondary vertices, as well as helping in the identification and tracking of low-momentum particles [71]. The measurement of primary and secondary vertices is crucial for the reconstruction of the light or heavy-flavour resonance particles. ITS further improves the measurement of TPC by providing additional tracking points near the interaction point.

Figure 3.3 shows an overview of the ITS2 structure operational during Run 3 of ALICE

[1] FT0 consists of FT0A and FT0C, which are also referred to as TO+A and T0+C, respectively, as depicted in Fig. 3.2.

[2] FV0 is usually referred to as FV0A (presently stationed in the direction of ATLAS) or V0+, as shown in Fig. 3.2.

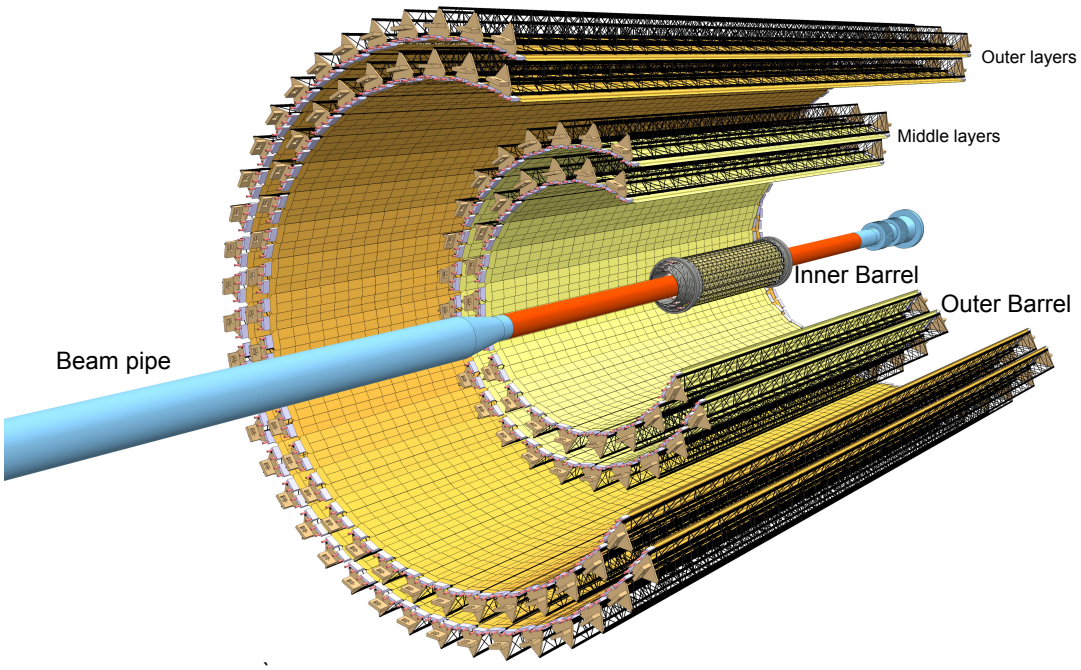

Figure 3.3: Schematic layout of ITS2 at ALICE during LHC Run 3 [70].

data taking, which replaces the ITS present during Run 1 and Run 2 of ALICE data taking. The primary goal of the ITS upgrade is to improve the reconstruction of the primary vertex and the decay vertex of the resonance hadrons, as well as improve the detection of low-p_{T} particles. The improvement in ITS includes increased granularity, the detector moved closer to the beam pipe (from 39 mm to 22.4 mm) and reduced material budget. The details of the upgrades from ITS to ITS2 can be found in Ref. [70]. In Fig. 3.3, ITS is grouped into the inner barrel (IB) and the outer barrel (OB). IB consists of three innermost layers, while OB consists of two double layers. Table 3.1 shows the ITS2 radial positions, stave details, as well as the total number of chips in each layer of ITS2 [70]. Stave is the basic detector unit of ITS2, consisting of a hybrid integrated circuit, a cold plate and a space frame [70]. A cold plate is a carbon fibre sheet with high thermal conductivity used for cooling. A space frame is a carbon fibre truss-like support structure that provides mechanical support and necessary stiffness. The radial positions of each layer of ITS2 are optimised based on the best performance of pointing resolution, p_{T}-resolution and tracking efficiency in the high track-density (high multiplicity) environment of Pb-Pb collisions. The pseudo-rapidity coverage of ITS2 is $|\eta| < 1.22$ for the interaction having z-component of the interaction vertex, $V_z \approx 10$ cm. ITS2 encompasses a total

Table 3.1: Layout parameters of ITS2 [70].

Layer no.	Average radius (mm)	Stave length (mm)	No. of staves	Total no. of chips
0	23	271	12	108
1	31	271	16	144
2	39	271	20	180
3	196	844	24	2688
4	245	844	30	3360
5	344	1478	42	8232
6	393	1478	48	9408

surface area of 10 m^2 and is operated at a room temperature (20°C to 25° C) using water cooling. There are 192 identical readout units and 142 power boards which provide complete control over power management, triggering, and data readout. The performance of readout and power management is unaffected when tested against a magnetic field of 0.5 Tesla.

Figure 3.4 shows the schematic of $\Xi^- \rightarrow \Lambda + \pi^-$ decay topology through ITS2 layers. The arcs represent the reconstructed tracks. Figure 3.5 shows the dE/dx versus track rigidity in the ALICE ITS2 inner barrel for pp collisions at $\sqrt{s}$ = 13.6 TeV [81, 82]. A clear identification of charged pions, kaons and protons can be inferred. The new ITS2 is excellent for both PID and tracking.

In the next section, we will move the discussion to another important tracking and PID detector in the central barrel, namely, the TPC.

3.2.2 Time Projection Chamber (TPC)

TPC is the primary detector used for tracking and particle identification, which covers a pseudo-rapidity range $|\eta| < 0.9$ in the complete azimuth region. TPC is able to reconstruct primary tracks with transverse momentum ranging from 0.1 GeV/c to 100 GeV/c with a very good resolution. With the measurement of deflection by the magnetic field, ITS,

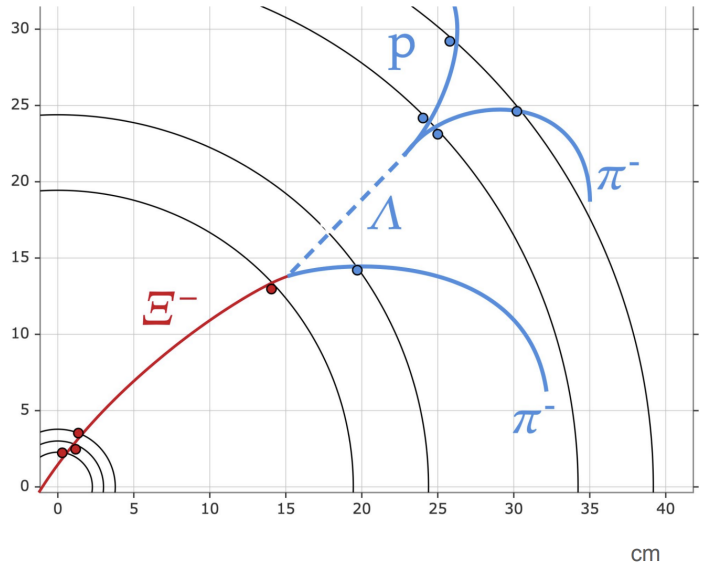

Figure 3.4: Schematic showing $\Xi^- \to \Lambda + \pi^-$ weak decay overlaid on the ITS2 geometry. Figure is taken from Ref. [81].

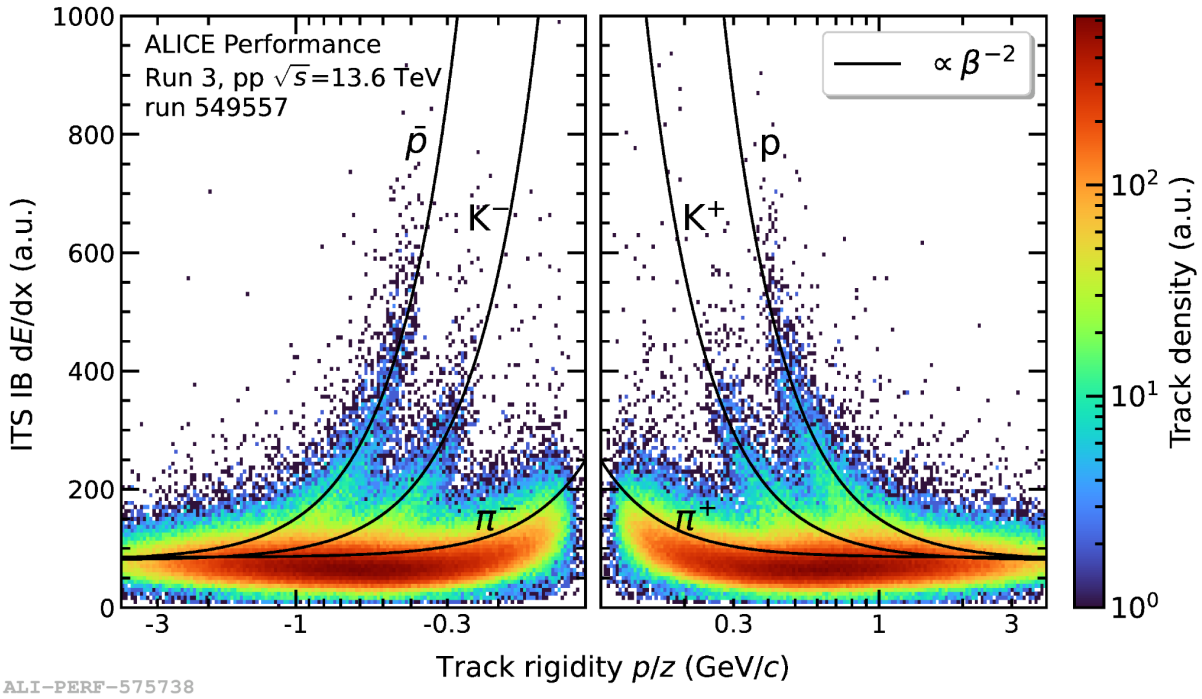

Figure 3.5: dE/dx versus track rigidity in the ALICE ITS2 inner barrel for pp collisions at $\sqrt{s} = 13.6$ TeV [81, 82].

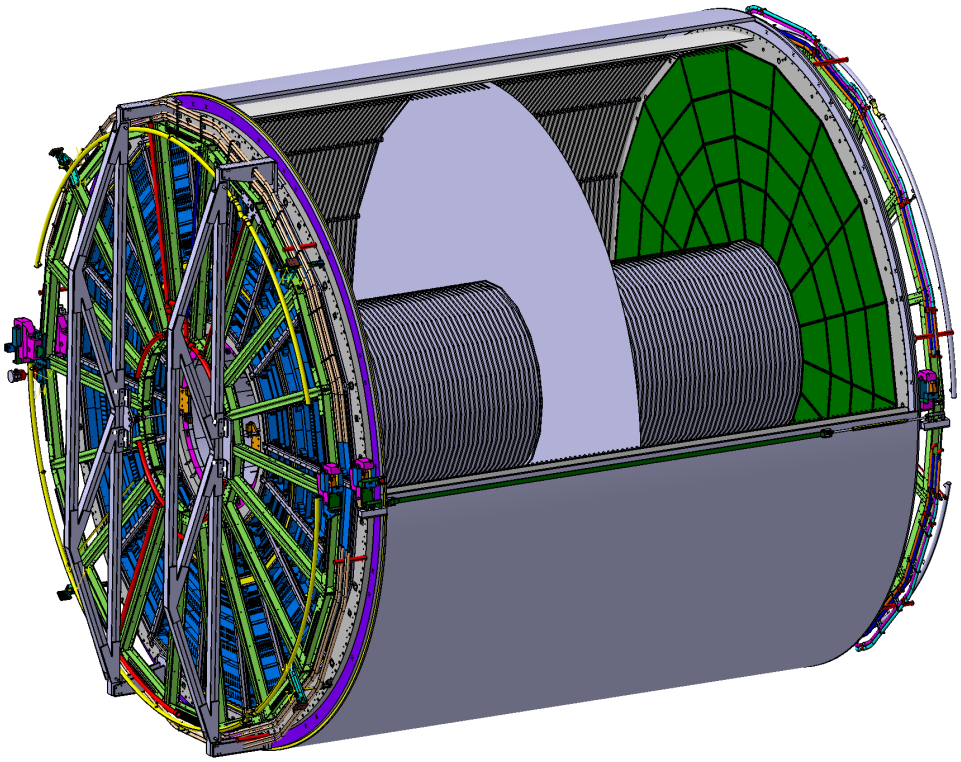

Figure 3.6: Schematic view of ALICE TPC. Figure is taken from Ref. [70].

along with TPC are able to determine momentum of charged particles with resolution better than 1% at lower values of p_{T}, which rises to 20% towards $p_{\mathrm{T}} \sim 100$ GeV/c.

The total active volume of TPC is 88 m^3, which is cylindrical in shape with a length and outer diameter of about 5 m. The TPC barrel has a high-voltage circular electrode at the center, which divides the total volume into halves, as shown in Fig. 3.6. The inner diameter of the TPC drum is 114 cm, which allows the required space for the ITS installation. Each of the two end plates of the TPC is subdivided into 18 azimuthal sectors, where each sector constitutes one inner and one outer readout chamber. During Runs 1 and 2, the TPC readout was based on a multiwire proportional chamber (MWPC). However, in the upgraded TPC, to cope with continuous readout, MWPC is replaced with Gas Electron Multipliers (GEMs) [83], which can be arranged in stacks to create layers of controlled amplification stages. TPC uses a combination of Ne-CO_2-N_2 (90-10-5) mixture for the operation. The gas mixture based on Ne provides higher ion mobility as compared to Ar.

TPC measures the particle energy loss and momentum simultaneously by measuring the charge collected in the TPC readout pads. This allows the separation of various

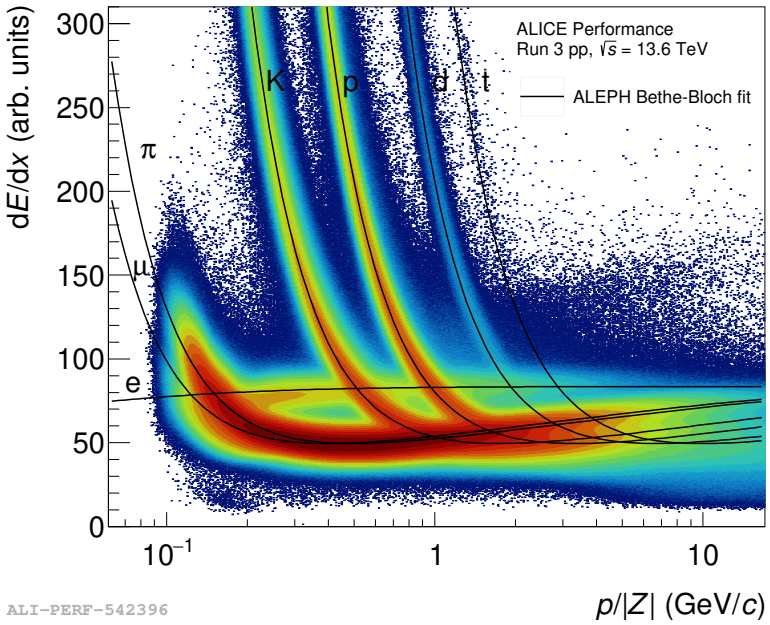

Figure 3.7: ALICE TPC dE/dx distribution for charged particles in pp collisions at $\sqrt{s} = 13.6$ TeV [85].

charged particle species, and thereby their identification, in the low-p_{T} region. The energy loss (dE/dx) of charged particle species in the TPC is estimated using the Bethe-Bloch formula, given as follows [84].

$$-\left\langle \frac{dE}{dx} \right\rangle = \frac{4\pi N z^2 e^4}{mc^2\beta^2}\left(\ln \frac{2mc^2\beta^2\gamma^2}{I} - \beta^2 - \frac{\delta(\beta)}{2} \right) \tag{3.1}$$

Here, N, m, and e are the number density, mass and electric charge of electrons, respectively. z, β and γ are the charge, velocity and Lorentz factor of the travelling particles, respectively. I is the average excitation energy and $\delta(\beta)$ is the correction term for the density effect [84]. In Eq. 3.1, dE/dx can be expressed as a parameterised form of $\beta\gamma$, which is used in the ALICE experiment (originally used in the ALEPH collaboration). The parameterisation is given as follows.

$$f(\beta\gamma) = \frac{P_1}{\beta^{P_4}}\left[P_2 - \beta^{P_4} - \ln\left(P_3 + \frac{1}{(\beta\gamma)^{p_5}} \right) \right] \tag{3.2}$$

Here, P_{1-5} are the fit parameters. Eq. (3.2) is often referred to as the ALEPH Bethe-Bloch function. Figure 3.7 shows the ALICE TPC dE/dx versus track rigidity in pp collisions at $\sqrt{s} = 13.6$ TeV. The solid lines represent the fit of Eq (3.2). Each track has an associated identification resolution (σ) with it, which can be obtained using the following expression.

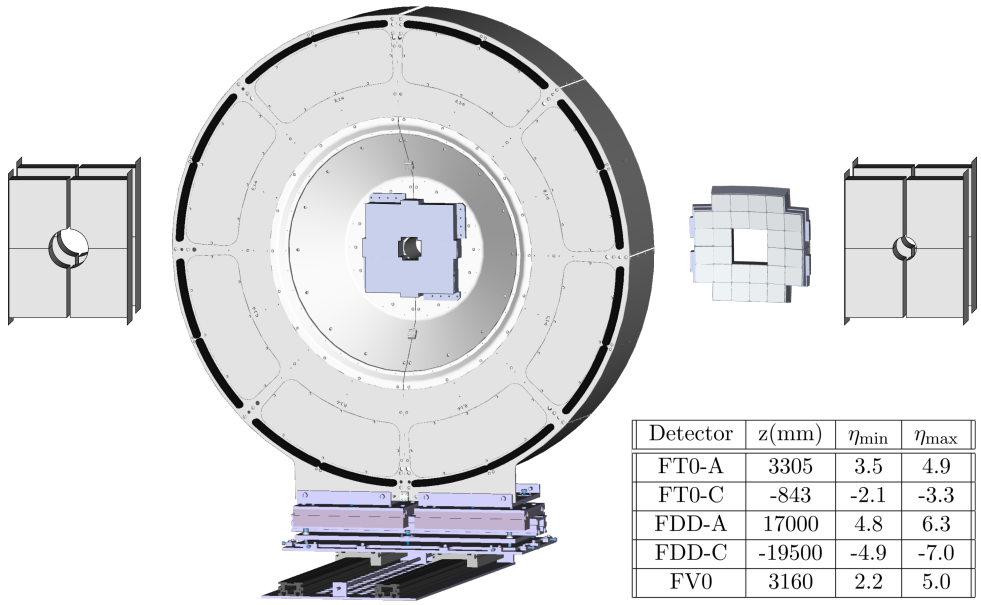

Detector	z(mm)	$\eta_{\min}$	$\eta_{\max}$
FT0-A	3305	3.5	4.9
FT0-C	-843	-2.1	-3.3
FDD-A	17000	4.8	6.3
FDD-C	-19500	-4.9	-7.0
FV0	3160	2.2	5.0

Figure 3.8: Schematic diagram of FIT detectors with relative sizes and pseudo-rapidity coverage. From left to right: FDD-A, FT0-A, FV0, FT0-C and FDD-C. FT0-C and FV0 have a common mechanical support, where FT0-C, a quadrangular structure, lies at the center of the large and circular FV0. Figure is taken from Ref. [70].

$$n\sigma = \frac{(dE/dx)_{\text{measured}} - (dE/dx)_{\text{expected}}}{\sigma^{\text{PID}}_{\text{TPC}}} \tag{3.3}$$

Here, $(dE/dx)_{\text{measured}}$ and $(dE/dx)_{\text{expected}}$ are the energy loss of the TPC measured tracks and the ALEPH Bethe-Bloch function, respectively. $\sigma^{\text{PID}}_{\text{TPC}}$ is the PID resolution of TPC.

3.2.3 Forward VZERO (FV0)

FV0 is a large and segmented scintillator disk which covers a rapidity region $2.2 < \eta < 5.0$ and possesses a time resolution of about 200 ps (2×10^{-10} s) [70]. FV0 has a four cm-thick plastic scintillator, which is divided into five concentric rings having equal pseudo-rapidity coverage. The outer diameter of FV0 is 144 cm, and the inner diameter is 8 cm. The inner four rings of FV0 are divided into eight sectors having 45° each. The outer ring is subdivided into 16 sectors, each covering 22.5° in azimuth. A total of 48 sectors of FV0 are connected to 48 readout channels. Figure 3.8 shows the schematic diagram of FDD-A, FT0-A, FV0, FT0-C and FDD-C, from left to right. FT0-C and FV0 have a common mechanical support, where FT0-C, a quadrangular structure, lies at the center of the

large and circular FV0. FV0 can provide information about charged particle multiplicity, which is used to estimate centrality and event plane resolution. Along with FT0, FV0 can provide minimum bias and multiplicity triggers at 'minus one' trigger level, with a total latency below 425 ns. Moreover, FV0 is also used to monitor LHC background conditions and luminosity.

3.3 ALICE Computing and Analysis

The ALICE grid was introduced to handle and process a large amount of data generated during the collisions. In the ALICE grid, the processing of data is allocated to several computing centres present worldwide. This is usually managed by Worldwide LHC Computing Grid (WLCG) project. ALICE grid uses the Models Of Network Analysis at Regional Centers (MONARC). MONARC is classified into different tiers and stages. Tier-0 handles all real data originating from CERN. Tier-1 are large regional computing centers that share the role of data storage and processing with CERN. Tier-2 are small centers clustered around Tier-1, which is used to perform MC simulations and user analysis. ALICE computing users use the ALICE Environment (ALIEN) to have access to grid computing and storage resources.

ALICE primarily uses the CERN-ROOT framework [86], which is based on C++ with integration of Python and R. It is equipped to handle petabytes of data and thus is useful for high-energy physics experiment analysis. Besides ROOT, the O2 framework was developed to fulfil the necessity of data analysis, detector simulations and MC event generation [87].

Chapter 4

Production of K^0_S and $\Lambda + \bar{\Lambda}$ as a function of charged particle flattenicity in pp collisions at $\sqrt{s} = 13.6$ TeV with ALICE

Based on: *S. Prasad and R. Sahoo, "Production of K^0_S and $\Lambda + \bar{\Lambda}$ as a function of charged particle flattenicity in proton-proton collisions at $\sqrt{s} = 13.6$ TeV with ALICE." Analysis Note ID number: ANA-1609 (ALICE Internal),* https://alice-notes.web.cern.ch/node/1609

4.1 Introduction and motivation

Chapter 1 of this thesis provides a general overview of QGP, including its various signatures and its possible formation in small systems such as pp collisions. Among the intriguing features observed in these systems are the enhanced production of strange hadrons and collective behavior, both of which require a deeper understanding of their underlying origins in small collision systems. Chapter 2 shows that the p-QCD-based models, such as PYTHIA 8, with the implementation of CR, RH and MPI, explain many of these QGP-like phenomena in small systems [52, 57, 58, 88]. Further, the chapter

introduces several event shape observables that are crucial for studying MPI, which are essential to explain flow-like effects in small collision systems. Investigating QGP signatures using a robust and unbiased event classifier can offer valuable insights into the microscopic mechanisms responsible for these phenomena. Among the various event shape classifiers, Chapter 2 highlights charged particle flattenicity as a particularly suitable tool for studying strangeness production in small systems. This preference arises from the fact that flattenicity is strongly correlated with MPI, minimally affected by auto-correlation biases, and less susceptible to contamination from multi-jet topologies [41, 42, 57, 58].

Although several event-shape observables have been employed by the ALICE experiment to explore the microscopic origin of QGP-like signatures in small systems, many of these observables suffer from selection biases. In a recent publication by ALICE collaboration, the collective effects and different biases of charged particle flattenicity are explored with the study of charged hadrons, and identified pions, kaons and protons [41]. In this chapter, I aim to study neutral strange hadrons as a function of charged particle flattenicity in pp collisions at $\sqrt{s}$ = 13.6 TeV using the new LHC Run 3 data. The analysis aims to demonstrate the neutral strange production along with cleaner radial flow signals with p_{T}-differential $(\Lambda+\bar{\Lambda})/2K^0_{\mathrm{S}}$. Possible selection biases of charged particle flattenicity are explored by studying Q_{pp}, defined as follows [88].

$$Q_{\mathrm{pp}} = \frac{d^2N^{\rho}_{\mathrm{V^0}}/\langle N^{\rho}_{\mathrm{V^0}}\rangle dydp_{\mathrm{T}}}{d^2N^{\mathrm{MB}}_{\mathrm{V^0}}/\langle N^{\mathrm{MB}}_{\mathrm{V^0}}\rangle dydp_{\mathrm{T}}} \tag{4.1}$$

Here, $\mathrm{V^0}$ stands for K^0_{S}, Λ, or $\bar{\Lambda}$. $N^{\rho}_{\mathrm{V^0}}$ and $N^{\mathrm{MB}}_{\mathrm{V^0}}$ stands for the number of $\mathrm{V^0}$s in a given percentile of charged particle flattenicity and the minimum bias events, respectively.

The chapter is organised as follows. We started with a brief introduction and motivation for the study in Section 4.1. Section 4.2 discusses the dataset used for the study. In Section 4.3, different event and track selection cuts are discussed. Section 4.4 introduces and defines charged particle flattenicity in LHC Run 3 of ALICE detector setup. The signal extraction, and corrections for K^0_{S}, Λ and $\bar{\Lambda}$ are discussed in Section 4.5. The chapter then moves towards the discussion of estimation of systematic uncertainties from different sources, which is shown in Section 4.6. The results obtained from the analysis are shown and discussed in Section 4.7. Finally, the chapter is summarised in Section 4.8.

4.2 Data Sets

This analysis uses the data collected by ALICE during Run 3 of the LHC. The data are based on pp collisions at $\sqrt{s} = 13.6$ TeV. ALICE data is organised based on the period of data taking and collision parameters, such as interaction rate, etc. Different filters are applied to improve data quality. The data where this analysis is performed correspond to the apass7 and 2024 of data taking. The analysis used AO2D data file format, which is standard for Run 3, unlike AODs and ESDs, which were used during Run 2. The details of the data and corresponding anchored Monte Carlo are given in the appendix (see Section 4.9.1). The data sample used in this study has approximately 1.42×10^{10} events, shown in Fig. 4.1.

4.3 Event and Track selection

4.3.1 Event Selection

The following event selection cuts are applied in this analysis, which is standard for the analysis with Run 3 data.

- Events that pass sel8 trigger selection criteria
- Vertex z position, $|v_z| < 10$ cm
- At least one charged particle within $|\eta| < 1.0$, INEL > 0

Figure 4.1 shows the event statistics after implementing different event selection cuts discussed earlier. The fourth bin, INEL > 0, shows the total number of accepted events used for this study, which is nearly 10^{10} events.

4.3.2 Track Selection

K^0_S and $\Lambda(\bar{\Lambda})$ are unstable neutral strange hadrons. These hadrons usually decay through the weak interaction, having average lifetimes of around 8.954×10^{-11} seconds (average decay length $\simeq 2.7$ cm) and 2.716×10^{-10} seconds (average decay length $\simeq 7.9$ cm), for

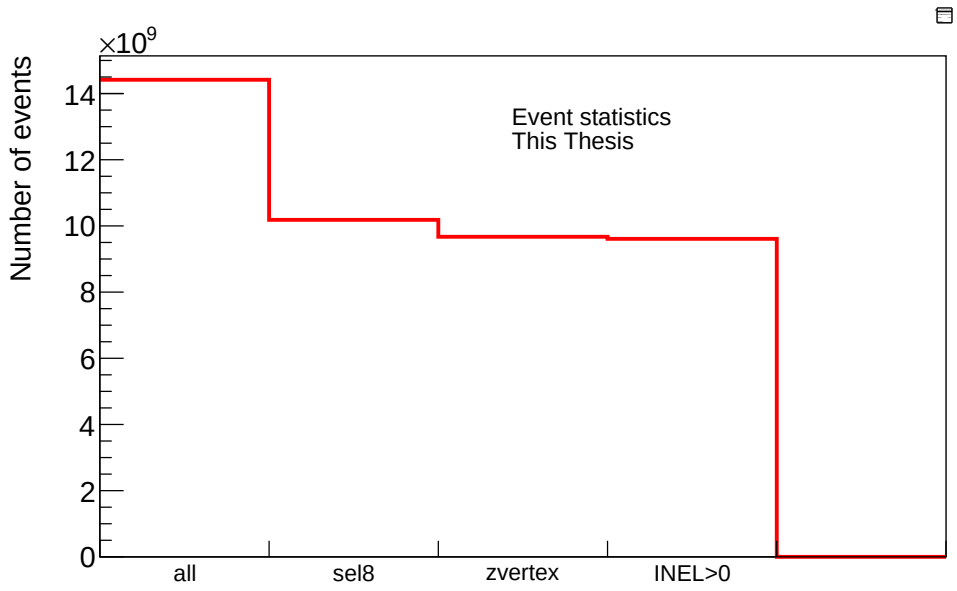

Figure 4.1: Event statistics after implementing event-selection cuts. The fourth bin (INEL > 0) shows the total number of events accepted for the analysis [89].

K^0_S and $\Lambda(\bar{\Lambda})$, respectively [90]. In ALICE, these neutral strange hadrons are usually reconstructed using the following decay channels.

$$K^0_S \rightarrow \pi^+\pi^- \qquad (\text{BR} : 69.2\%) \tag{4.2}$$

$$\Lambda \rightarrow p\pi^- \qquad (\text{BR} : 63.9\%) \tag{4.3}$$

$$\bar{\Lambda} \rightarrow \bar{p}\pi^+ \qquad (\text{BR} : 63.9\%) \tag{4.4}$$

K^0_S and $\Lambda(\bar{\Lambda})$, being chargeless are undetectable in the detectors. However, they decay into a V-shaped pair of detectable charged tracks. Because of the appearance of the decay topologies of these neutral strange hadrons in the detectors, they are commonly referred to as V^0s. A pictorial representation of V^0s and cascade decay topology is shown in Fig. 4.2.

In the new O^2 analysis framework, which is used for the results of this chapter, the O2Physics data format (AO2D) is used. This can store track index pairs or triplets for the analysis of V^0s and cascades [92]. All analysis-related properties for these V^0s and cascades can be easily constructed from these indices. The strangeness builders are centrally provided, which can construct the analysis information related to V^0s and cascades. These builders include the tasks "lambdakzerobuilder" and "cascadebuilder", which take

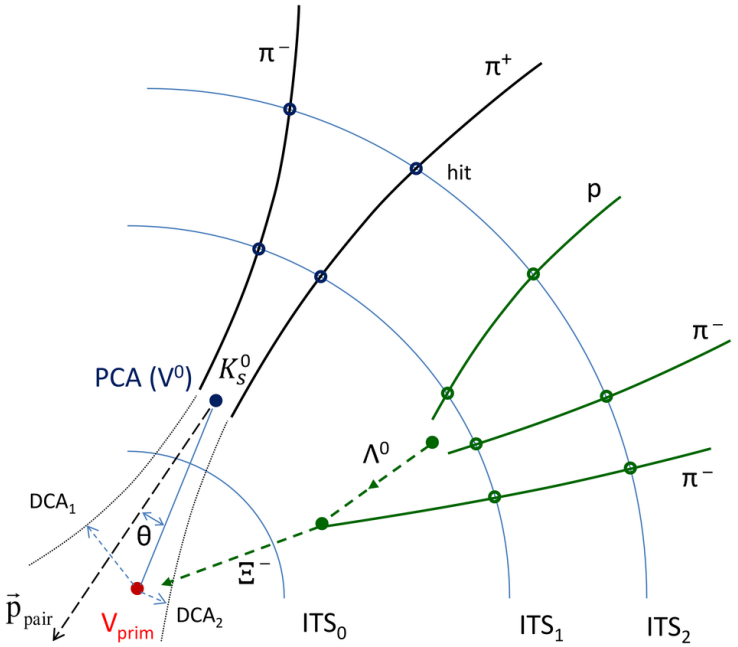

Figure 4.2: Decay topology of V^0s and cascades in ITS The reconstructed charged particle tracks, extrapolated to the secondary vertex are shown in solid lines. The extrapolations to the primary vertex are shown in dotted lines. The figure is taken from Ref. [91].

track index pairs and triplets, for V^0s and cascades, respectively, and construct the analysis information related to them. Additional selection criteria or cuts are further applied to suppress the background in the V^0s. The reconstructed tracks are required to fulfill the selection criteria listed in Table 4.1, which includes the cuts on the kinematics of the daughter and mother tracks, constraints on the decay topology, reconstruction quality of the daughter tracks, cuts on specific ionisation energy loss "dE/dx" of the daughter tracks in the TPC gas (expressed as σ_{TPC}). Further, V^0s candidates with invariant mass calculated under the competing hypothesis of daughter masses too close to the mass of the competing V^0s are rejected. Here, a V^0 with $M_{\pi\pi} \approx m_{K^0_S}$ will not be considered as a Λ or $\bar{\Lambda}$ candidate. The selection criteria listed in Table 4.1 remove most of the combinatorial background for K^0_S, Λ and $\bar{\Lambda}$. The residual background can be further removed by the sideband fitting procedure, which is discussed in Section 4.5.

V^0 daughter track selection	
Pseudorapidity, $\|\eta\|$	< 0.8
DCA Negative Track to PV	> 0.06 cm
DCA Positive Track to PV	> 0.06 cm
TPC dE/dx selection	$< 5\sigma$
V^0 Selection Criteria	
V^0 Decay Radius	> 0.5 cm
V^0 Cosine of Pointing Angle	> 0.97 for K^0_S, > 0.995 for Λ
DCA V^0 daughters	< 1.0
Rapidity, $\|y\|$	< 0.5
Proper Lifetime	< 20 cm for K^0_S, < 30 cm for Λ
Competing Mass Rejection	$M_{p\pi} - m_\Lambda > 0.005$ for K^0_S $M_{\pi\pi} - m_{K^0_S} > 0.01$ for Λ
Armenteros-Podolanski (for K^0_S)	$Q_T > 0.2 \times \|\alpha\|$

Table 4.1: V^0 and V^0 daughter track selection criteria for K^0_S and Λ [89].

4.4 Flattenicity

Chapter 2 discusses the charged particle flattenicity with Run 2 ALICE detector configurations, where it is defined using the charged particle multiplicity in ALICE V0A+V0C detectors. However, with the upgrade for Run 3 of data taking, V0 is removed; instead, the FIT detector is installed at the forward rapidity. Thus, for this study, the charged particle flattenicity (ρ) is defined using the energy registered in the FV0A detector ($2.2 < \eta < 5.1$) of ALICE. The energy deposition in cell 'i' of FV0 is proportional to the charged particle multiplicity ($N_{\rm ch}^{{\rm cell},\ i}$) in the cell. Flattenicity can be calculated using the following equation [41, 42].

$$\rho = \frac{\sqrt{\sum_i^{N_{\rm cell}} (N_{\rm ch}^{{\rm cell},\ i} - \langle N_{\rm ch}^{\rm cell}\rangle)^2 / N_{\rm cell}^2}}{\langle N_{\rm ch}^{\rm cell}\rangle} \tag{4.5}$$

Here, $N_{\rm cell}$ is the total number of cells, $N_{\rm ch}^{{\rm cell},\ i}$ is the particle multiplicity in the ith cell, and $\langle N_{\rm ch}^{\rm cell}\rangle$ is the average number of charged particles in the cells. Flattenicity is shown to

be robust against the choice of the bin size [42]. Flattenicity is a quantitative estimate of energy or multiplicity fluctuations in the FV0A detector. Small fluctuations would lead to a smaller value of flattenicity, i.e., $\rho \to 0$. The value of ρ ranges between 0 and 1. Based on PYTHIA 8 simulations, a large value of flattenicity, i.e., $\rho \to 1$, would imply events dominated by jet topologies, while a smaller value would correspond to events having large MPI or isotropic in nature [41, 42]. To be consistent with other event shape observables, in this study, the calculations are made with $(1-\rho)$. Thus, $(1-\rho) \to 0$ would imply events dominated by hard processes, and $(1-\rho) \to 1$ would correspond to soft isotropic events. The left panel of Fig. 4.3 shows the correlation between flattenicity estimated from the FV0A detector in Run 3 and the V0 (V0A+V0C) detector in Run 2 in pp collisions at $\sqrt{s} = 13$ TeV using PYTHIA 8 Monash. Here, a good qualitative agreement is observed between the flattenicity calculations performed in FV0A versus V0 detector pseudorapidity regions towards higher values of $(1-\rho)$. However, deviations in the values of ρ from two pseudorapidity regions become significant towards the lower values of $(1-\rho)$. The right panel of Fig. 4.3 shows the correlation between the average number of multi-partonic interactions ($\langle N_{\rm mpi} \rangle$) and average transverse momentum transfer of the hardest parton-parton interactions ($\langle \hat{p}_{\rm T} \rangle$). Here, ρ estimated using V0 detector pseudorapidity region has larger coverage in $\langle N_{\rm mpi} \rangle$ versus $\langle \hat{p}_{\rm T} \rangle$ as compared to $\rho_{\rm FV0A}$. This can be attributed to a larger pseudorapidity coverage of the V0 detector as compared to FV0A. The left panel of Fig. 4.4 shows the $(1-\rho)$ distribution measured with the FV0A detector. The right panel shows the reconstruction efficiency of flattenicity with the FV0A detector. The reconstruction efficiency is good towards higher values of $(1-\rho)$. Table 4.2 shows the definition of flattenicity percentiles classes and corresponding values of $(1-\rho)$ used in this study

Quantity	**Values**				
% Class	$0-10$	$10-20$	$20-30$	$30-50$	$50-100$
$(1-\rho)$ **range**	$0.90-1$	$0.88-0.90$	$0.86-0.88$	$0.83-0.86$	$0-0.83$

Table 4.2: Definition of flattenicity percentiles classes and corresponding values of $(1-\rho)$ used in this study [89, 93].

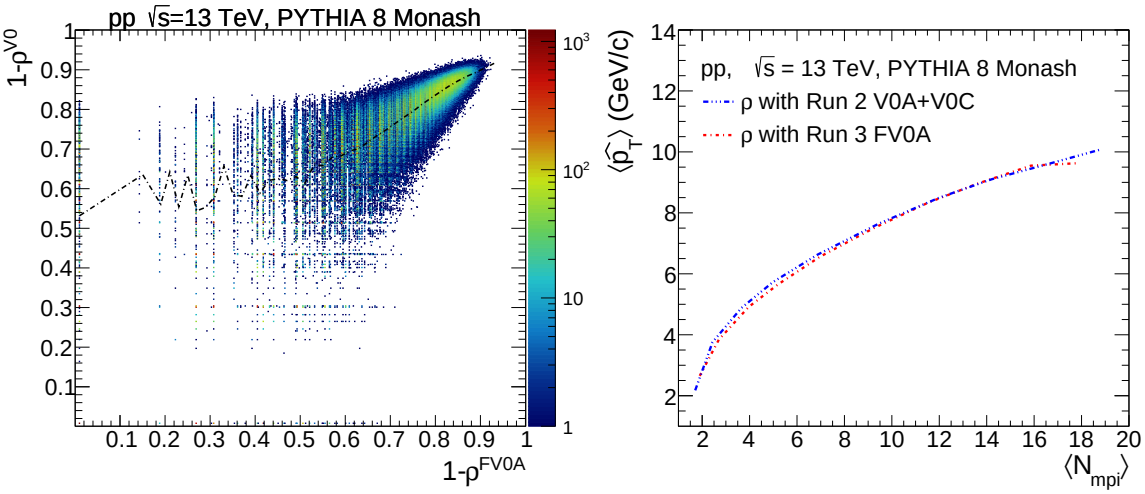

Figure 4.3: (Left) Correlation between flattenicity estimated from FV0A detector in Run 3 and V0 (V0A+V0C) detector in Run 2. (Right) Correlation between $\langle N_{\mathrm{mpi}} \rangle$ and $\langle \hat{p}_{\mathrm{T}} \rangle$ as a function of flattenicity in pp collisions at $\sqrt{s} = 13$ TeV using PYTHIA 8 Monash [89].

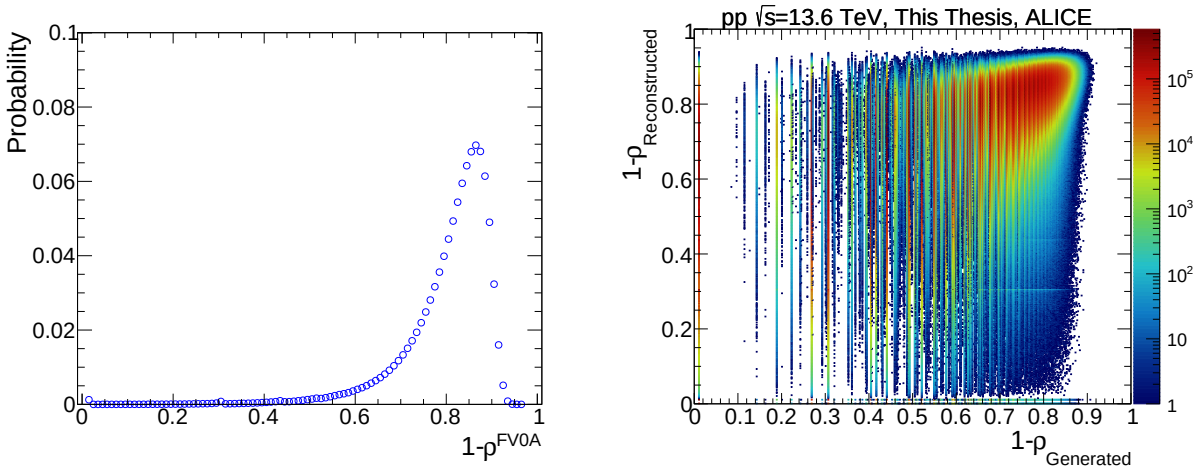

Figure 4.4: (Left) Flattenicity probability distribution measured with FV0A and (Right) Correlation between flattenicity calculated from generation versus reconstruction level [89].

4.5 K^0_S, Λ, and $\bar{\Lambda}$ signal extraction and corrections

The particle identification from the reconstructed V^0s can be made based on the invariant mass. An invariant mass analysis is used to statistically separate the signal from the combinatorial background. The invariant mass of the particles is calculated using the following expression:

$$M_{\rm inv} = \sqrt{(E_1 + E_2)^2 - (|\vec{p}_1 + \vec{p}_2|)^2}, \tag{4.6}$$

where E_i, and $\vec{p}_i$ are the energy and momenta of the 'i'th daughter. Here, the invariant mass distribution for the particle pairs are obtained. The invariant mass of the particle pairs represent the parent particle when the pairs originate from it i.e., $M_{\pi\pi} = M_{K^0_S}$, and $M_{p\pi} = M_\Lambda$. The V^0 signal can be separated from the background in distributions of $\Delta M_{\rm V^0} = M_{\rm inv} - m_{\rm V^0}$ by different signal extraction methods. Here $m_{\rm V^0}$ is the rest mass of the V^0 candidate taken from the PDG [94]. The sideband method is used to separate the signal from the residual background in each $p_{\rm T}$-intervals, considering the signal peak around $\Delta M_{\rm V^0}$ and an approximate linear background in the signal region. The details of the sideband procedure used in this study are given in Section 4.5.1.

4.5.1 Signal extraction using sideband method

The mean (μ) and widths (σ) of the V^0 peak in the invariant mass distribution are estimated using a χ^2-minimization fit with a seven-parameter function. The function contains a linear background function along with two Gaussian functions with common mean, μ, and varying widths, σ_1 and σ_2, respectively.

$$f(\Delta M_{\rm V^0}) = \{0\} + \{1\} \cdot \Delta M_{\rm V^0} + \{2\} \cdot G(\Delta M_{\rm V^0}, \mu, \sigma_1^2) + \{3\} \cdot G(\Delta M_{\rm V^0}, \mu, \sigma_2^2). \tag{4.7}$$

Here, G stands for a Gaussian function, and $\{\cdot\}$ represents four free parameters. The function shown in Eq. (4.7) is used to extract μ, σ_1, and σ_2 across all $p_{\rm T}$ intervals. A demonstration of fit for $1.0 < p_{\rm T} < 1.1$ GeV/c is as shown in Fig: 4.5. In each $p_{\rm T}$ bin, a common parameter σ can be obtained from the two Gaussian functions as the standard deviation of $\{2\} \cdot G(\mu, \sigma_1^2) + \{3\} \cdot G(\Delta M_{\rm V^0}, \mu, \sigma_2^2)$ distribution, sampled 10^5 times. The

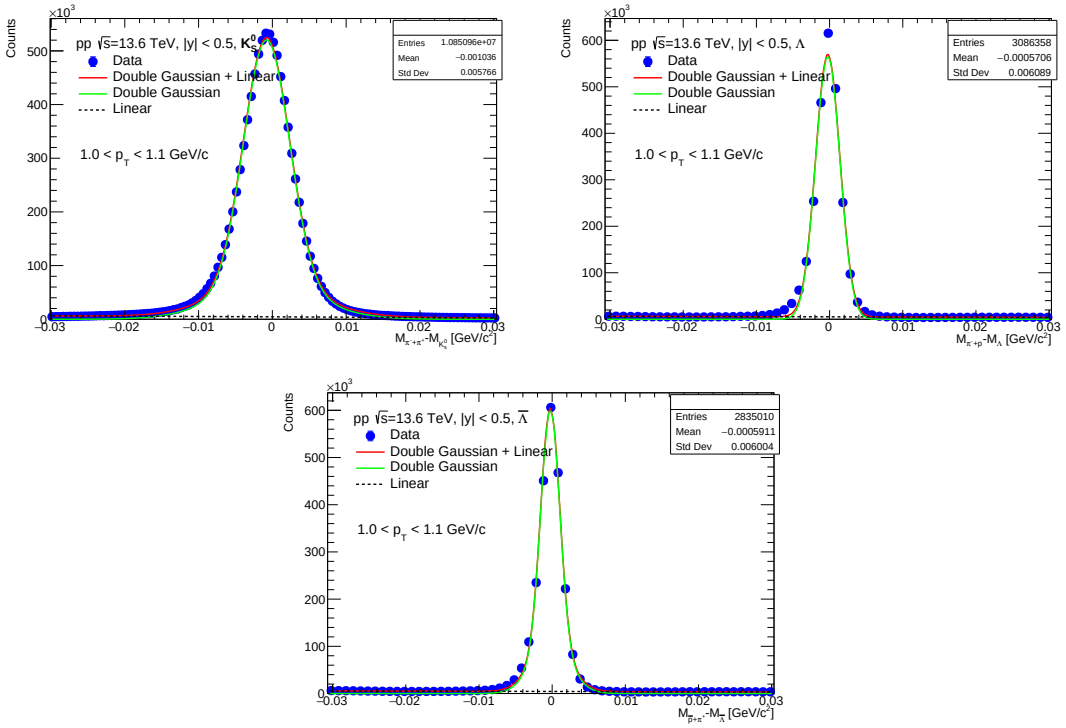

Figure 4.5: Fit of invariant mass distribution of K^0_S (left), Λ (right), and $\bar{\Lambda}$ (bottom) with Eq. (4.7) [89].

variables μ and σ for each V^0s, denoted as μ_{V^0} and σ_{V^0}, can be interpolated using the following functions with a χ^2 fit.

$$\mu_{K^0_S}(p_T) = \begin{cases} \{0\} + \{1\} \cdot p_T + \{2\} \cdot p_T^2 & \text{if } p_T < 1.6 \text{ GeV}/c \\ \{3\} & \text{if } p_T \geq 1.6 \text{ GeV}/c \end{cases} \tag{4.8}$$

$$\mu_{\Lambda,\bar{\Lambda}}(p_T) = \begin{cases} \{0\} + \{1\} \cdot p_T + \{2\} \cdot p_T^2 & \text{if } p_T < 1.9 \text{ GeV}/c \\ \{3\} + \{4\} \cdot p_T & \text{if } p_T \geq 1.9 \text{ GeV}/c \end{cases} \tag{4.9}$$

$$\sigma_{V^0}(p_T) = \{0\} + \{1\} \cdot p_T + \frac{\{2\}}{p_T} \tag{4.10}$$

Figure 4.6 shows the means and sigmas extracted from the above-mentioned steps. The solid red and blue lines, respectively, denote the parameterised μ and σ using Eqs. (4.8), (4.9) and (4.10) for K^0_S (left), Λ (middle), and $\bar{\Lambda}$ (right). In each p_T bin, one defines the signal region N as $(\mu_{V^0} - 4\sigma_{V^0};\ \mu_{V^0} + 4\sigma_{V^0})$ and sidebands A, and B as $(\mu_{V^0} - 8\sigma_{V^0};\ \mu_{V^0} - 4\sigma_{V^0})$ and $(\mu_{V^0} + 4\sigma_{V^0};\ \mu_{V^0} + 8\sigma_{V^0})$, respectively. N, A, and B can

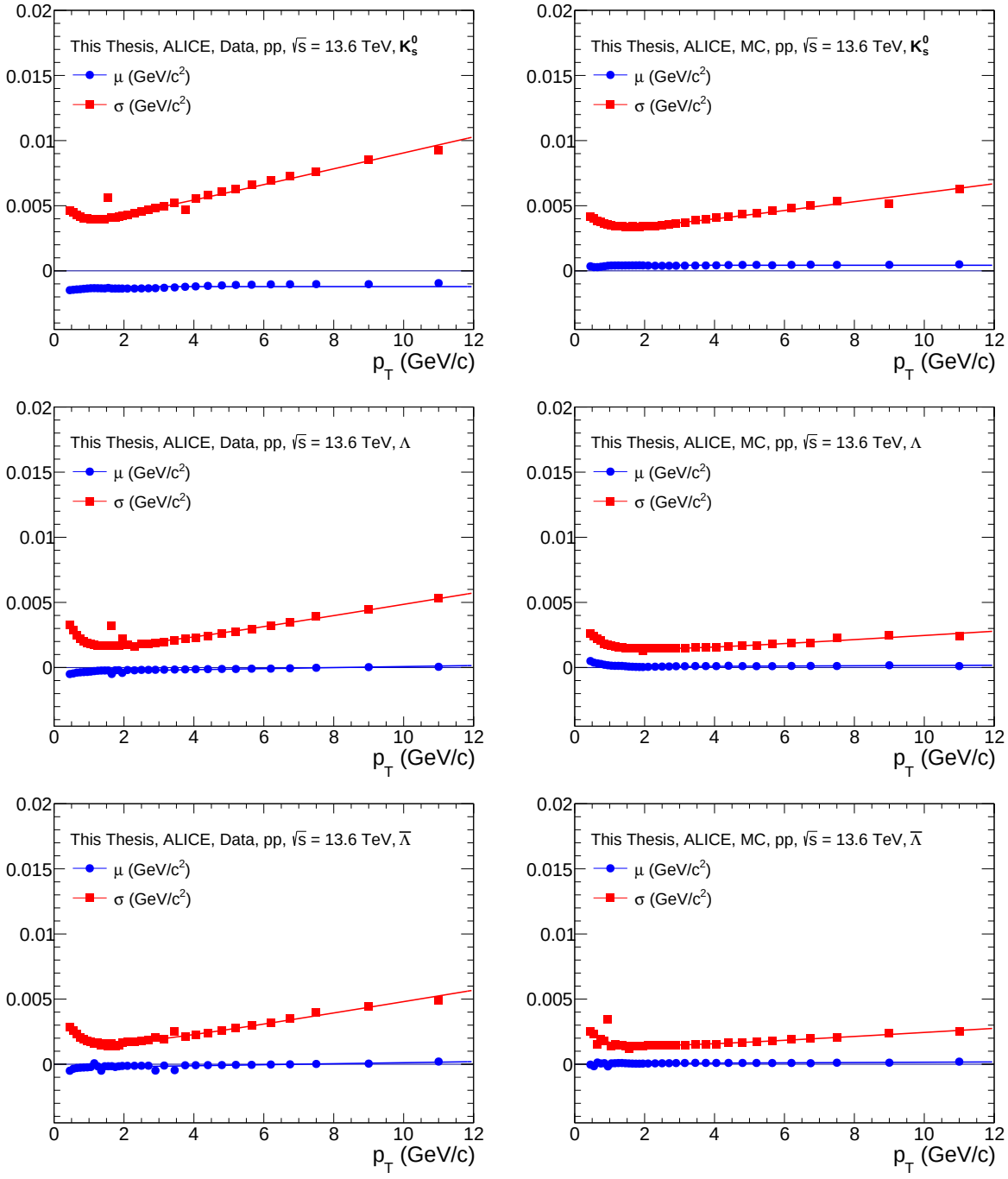

Figure 4.6: Means (μ) and widths (σ) extracted from the fit of Eq. 4.7 to the invariant mass spectra of V^{0}s. The solid red and blue lines, respectively, denote the parameterised μ and σ using Eqs. (4.8), (4.9) and (4.10) for K^0_S (upper), Λ (middle), and $\bar{\Lambda}$ (lower) [89].

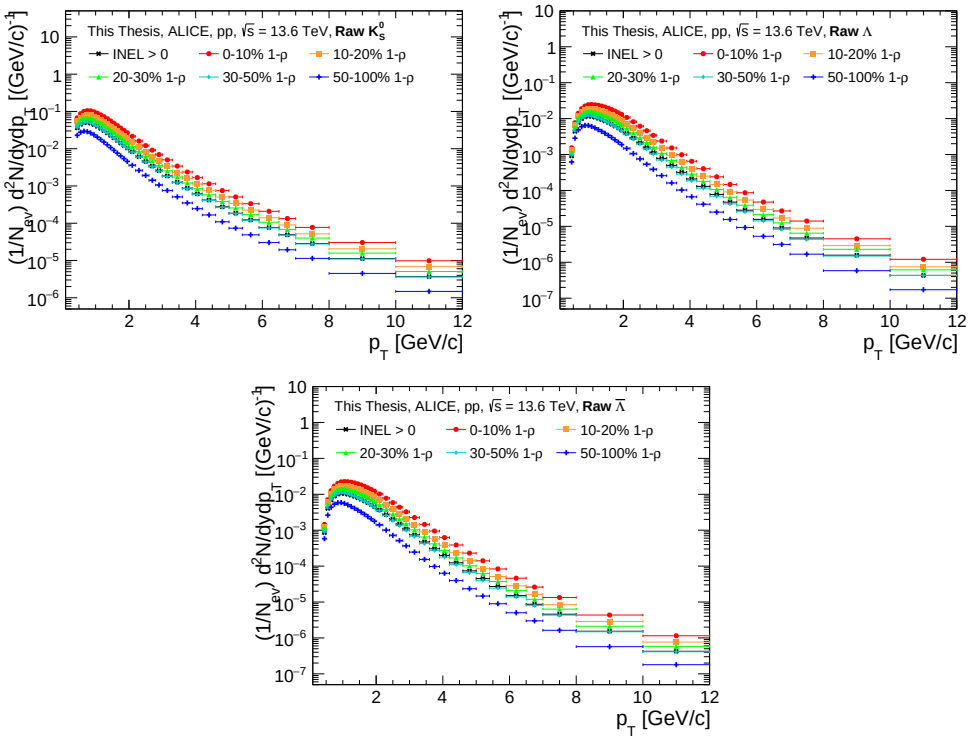

Figure 4.7: Raw p_{T}-spectra of K^0_{S} (left), Λ (right), and $\bar{\Lambda}$ (bottom) for different percentile classes of flattenicity in pp collisions at $\sqrt{s} = 13.6$ TeV with ALICE [89].

be calculated using the sum of entries in these regions. Considering a linear background, the background in the signal region would be the sum of the backgrounds in the sideband regions. Thus, the particle yields Y, and corresponding uncertainty σ_Y for each p_{T} bin can thus be evaluated using the following expressions [95].

$$Y = N - A - B \tag{4.11}$$

$$\sigma_Y = \sqrt{N + A + B} \tag{4.12}$$

Here, the statistical uncertainties in the signal and sideband regions are uncorrelated. Fig. 4.7 shows the raw p_{T}-spectra of K^0_{S} (left), Λ (middle), and $\bar{\Lambda}$ (right) for different percentile classes of flattenicity in pp collisions at $\sqrt{s} = 13.6$ TeV.

4.5.2 Corrections

To obtain the final spectra, one needs to apply corrections to the measured raw spectra. The measured spectra are normalised to the accepted number of INEL > 0 events, which is discussed in Section 4.3.1. The corrections include acceptance $\times$ efficiency ($\epsilon_{\mathrm{acc.}\times\mathrm{eff.}}$), event

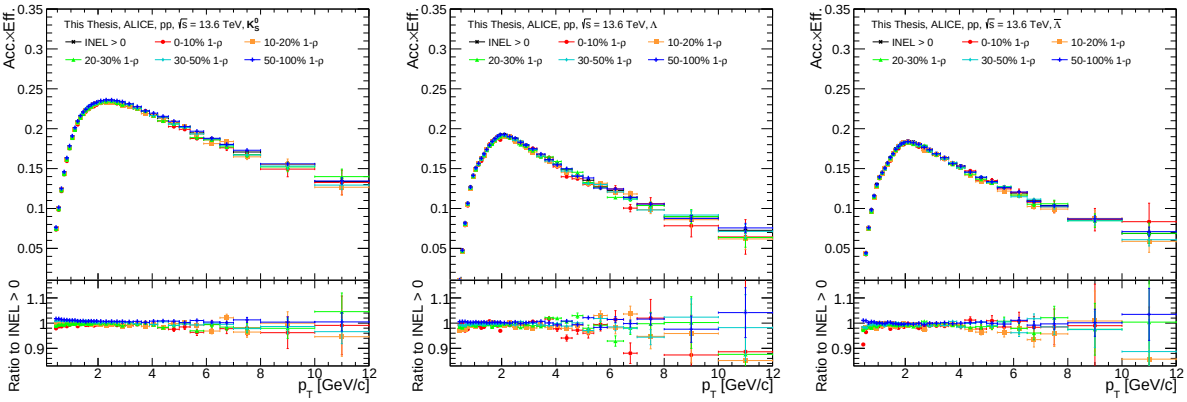

Figure 4.8: $\epsilon_{\text{acc.}\times\text{eff.}}$ correction factors of K^0_S (left), Λ (middle), and $\bar{\Lambda}$ (right) for different percentile classes of flattenicity in pp collisions at $\sqrt{s} = 13.6$ TeV with ALICE. The bottom panel shows the ratios to INEL > 0 events [89].

loss (ϵ_{event}), event splitting (ϵ_{split}), and signal loss (ϵ_{signal}). The correction factors can be calculated using Monte Carlo simulations, where both the generation and reconstruction level information are stored. After the calculation of these correction factors, one can obtain the final and corrected spectra using the following expression.

$$\frac{1}{N^{\text{true INEL>0}}_{\text{events}}} \times \frac{dN^{\text{true INEL>0}}_{\text{part}}}{dp_{\text{T}}}(p_{\text{T}}) = \frac{1}{N^{\text{reco INEL>0}}_{\text{events}}} \times \frac{dN^{\text{reco INEL>0}}_{\text{part}}}{dp_{\text{T}}}(p_{\text{T}}) \times \frac{1}{\epsilon_{\text{acc.}\times\text{eff.}}(p_{\text{T}})} \times \frac{\epsilon_{\text{event}}}{\epsilon_{\text{split}} \times \epsilon_{\text{signal}}(p_{\text{T}})} \tag{4.13}$$

4.5.2.1 Acceptance×efficiency

The determination of acceptance and efficiency correction factors for the measured raw spectra requires the input from the Monte Carlo data sample with the same selections and signal extraction procedures performed for the real data samples. Here, for each V^0s, the PDG values are cross-checked with the Monte Carlo. The selected V^0s are required to be a primary particle (`mcParticles:: isPhysicalPrimary()`). $\epsilon_{\text{acc.}\times\text{eff.}}$ can be computed by taking the ratios of reconstructed particle yield to the generated particle yield, as follows.

$$\epsilon_{\text{acc.}\times\text{eff.}} = \frac{N_{\text{reco+associated V}^0}(p_{\text{T}})}{N_{\text{gen V}^0,\text{ reco event}}(p_{\text{T}})} \tag{4.14}$$

Figure 4.8 shows the acceptance × efficiency correction factors for K^0_S (left), Λ (middle), and $\bar{\Lambda}$ (right) for INEL > 0 and different flattenicity percentile events in pp collisions

at $\sqrt{s} = 13.6$ TeV. The efficiency is higher for K^0_S, as compared to Λ, and $\bar{\Lambda}$ throughout the p_T regions. Here, the acceptance×efficiency is similar for all the flattenicity percentile classes for all the V^0s. The variation is smaller than 3%. Thus, in this analysis, the acceptance × efficiency is used from the INEL > 0 case and the maximum difference of 3% is taken care of in the systematic uncertainty for individual flattenicity class measurements.

4.5.2.2 Event splitting and event loss

The event loss factor, ϵ_{event}, can be calculated as the ratio of the number of reconstructed events to the number of events with "true" production vertex located within $|z^{\text{true}}_{\text{vtx}}| <$ 10 cm having at least one charged particle produced in $|\eta| < 1$. However, in Run 3, due to continuous data taking with the ALICE detector, the data are not delimited by physics triggers. Here, the data are composed of several constant data streams that are transferred from the computers to the computing systems, which can cause ambiguity in the event reconstruction procedure [96]. For example, one collision can be reconstructed twice. This is called event splitting, which can be quantified in terms of event splitting efficiency, ϵ_{split}, as follows.

$$\epsilon_{\text{split}} = \frac{N^{\text{true, reco INEL>0}}_{\text{event}}}{N^{\text{reco INEL>0}}_{\text{event}}} \tag{4.15}$$

On the other hand, due to the event selection cuts discussed in Section 4.3.1, event loss can happen, which can be quantified in terms of the ratios of the number of reconstructed events that pass the selection criteria in Section 4.3.1 to the number of generated events with at least one charged particle produced in $|\eta| < 1.0$, i.e.,

$$\epsilon_{\text{event}} = \frac{N^{\text{true, reco INEL>0}}_{\text{event}}}{N^{\text{true INEL>0}}_{\text{event}}}. \tag{4.16}$$

4.5.2.3 Signal loss

Similar to event loss, one can expect deviations in the p_T-dependence loss in the signal, which can be quantified using ϵ_{signal}. It is important to note here that ϵ_{signal} can also have contributions from the event loss. Therefore, in Eq. (4.13), the factor $\frac{\epsilon_{\text{event}}}{\epsilon_{\text{split}} \times \epsilon_{\text{signal}}(p_T)}$ along with acceptance × efficiency corrections would lead to a fully corrected spectra. The signal loss can be calculated using the ratios of particle spectra at the generated level after the event selection and the generated particle spectra from true INEL > 0 events,

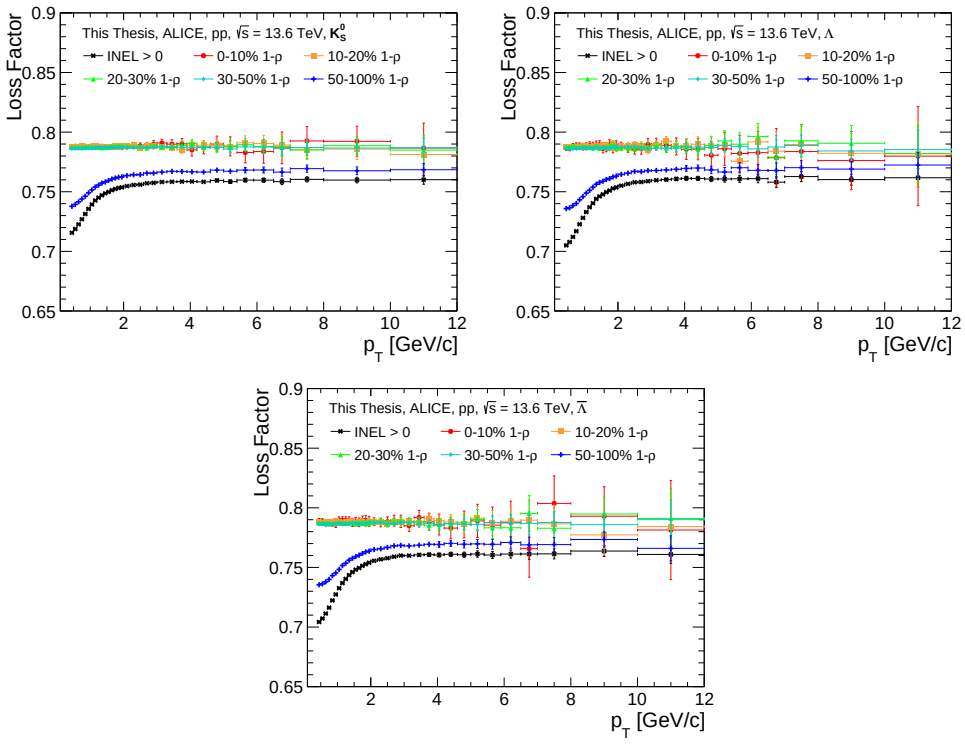

Figure 4.9: p_{T}-dependent signal loss correction factors as a function of flattenicity percentiles for K^0_{S}, Λ, and $\bar{\Lambda}$ in pp collisions at $\sqrt{s} = 13.6$ TeV [89].

as follows.

$$\epsilon_{\mathrm{signal}} = \frac{\frac{dN^{\mathrm{gen}}_{\mathrm{part}}}{dp_{\mathrm{T}}}(\text{reco INEL} > 0)}{\frac{dN^{\mathrm{gen}}_{\mathrm{part}}}{dp_{\mathrm{T}}}(\text{true INEL} > 0)}. \tag{4.17}$$

Figure 4.9 shows the signal loss factor calculated using Eq. (4.17) of K^0_{S}, Λ, and $\bar{\Lambda}$ for INEL > 0 and different classes of flattenicity in pp collisions at $\sqrt{s} = 13.6$ TeV with ALICE. Interestingly, the signal loss correction factors are similar for all the V^0s throughout the p_{T} regions.

4.6 Systematic uncertainties

The measurements performed in experiments always come with two kinds of uncertainties: statistical and systematic. The statistical uncertainties arise as a consequence of a limited number of measurements, which can be improved by increasing the size of the data sample. In contrast, the systematic uncertainties are caused by the imprecision or the bias of the experimental measurement method. Unlike the statistical uncertainties, which can be calculated based on a frequentist approach, the calculation of systematic uncertainties is

not straightforward. One needs to identify all possible sources of systematic uncertainties and finally measure them with reasonable method variations. In the present study, the following sources of systematic uncertainties are identified.

1. **Signal extraction region**: In this analysis, the standard signal region is considered to be within $\mu_{\mathrm{V^0}} \pm 4\sigma_{\mathrm{v^0}}$, whereas the background region is assumed to be linear with a change in invariant mass. The biases coming from the selection of signal and background regions can be tested against the biases of the sideband background estimation procedure by considering wider or narrower signal and background regions. This can be achieved by changing the number of $\sigma_{\mathrm{V^0}}$s to 5 and 3 times for wider and narrower signal and background regions, respectively. Figure 4.10 shows the relative deviation of the wider and narrower signal regions with respect to the standard measurements for the $\mathrm{V^0}$s as a function of different flattenicity classes. The relative deviation is defined as the deviation of the ratio B/A from unity, where B is the different measurement procedure, and A is the standard measurement procedure. From the wider and narrower signal regions, we consider the highest deviation for each p_{T} bin from both the methods, and we denote it as the maximum relative deviation, shown in Fig. 4.10 right column.

2. **Variation of selection criteria**: During the estimation of reconstruction efficiency, it is assumed that in ALICE MC simulations, all the topological and kinematic cuts for the identifications $\mathrm{V^0}$s and the quality of the daughter tracks represent the reality. However, their inaccurate description of the real data can create a bias in the measurements. This bias can be estimated by measuring the sensitivity of the measurements with the variations of topological and kinematic cuts used for selecting the $\mathrm{V^0}$s and the quality of daughter tracks. In this study, such a measurement is performed by making the kinematic and topological cuts tight and loose. This is shown in Table 4.3. Figure 4.11 shows the relative deviation of measurements with loose and tight topological cuts to obtain different $\mathrm{V^0}$s signals. The right column shows the maximum deviation chosen out of the tighter and looser selection cuts.

3. **Acceptance×efficiency correction**: In this analysis, we have used the acceptance

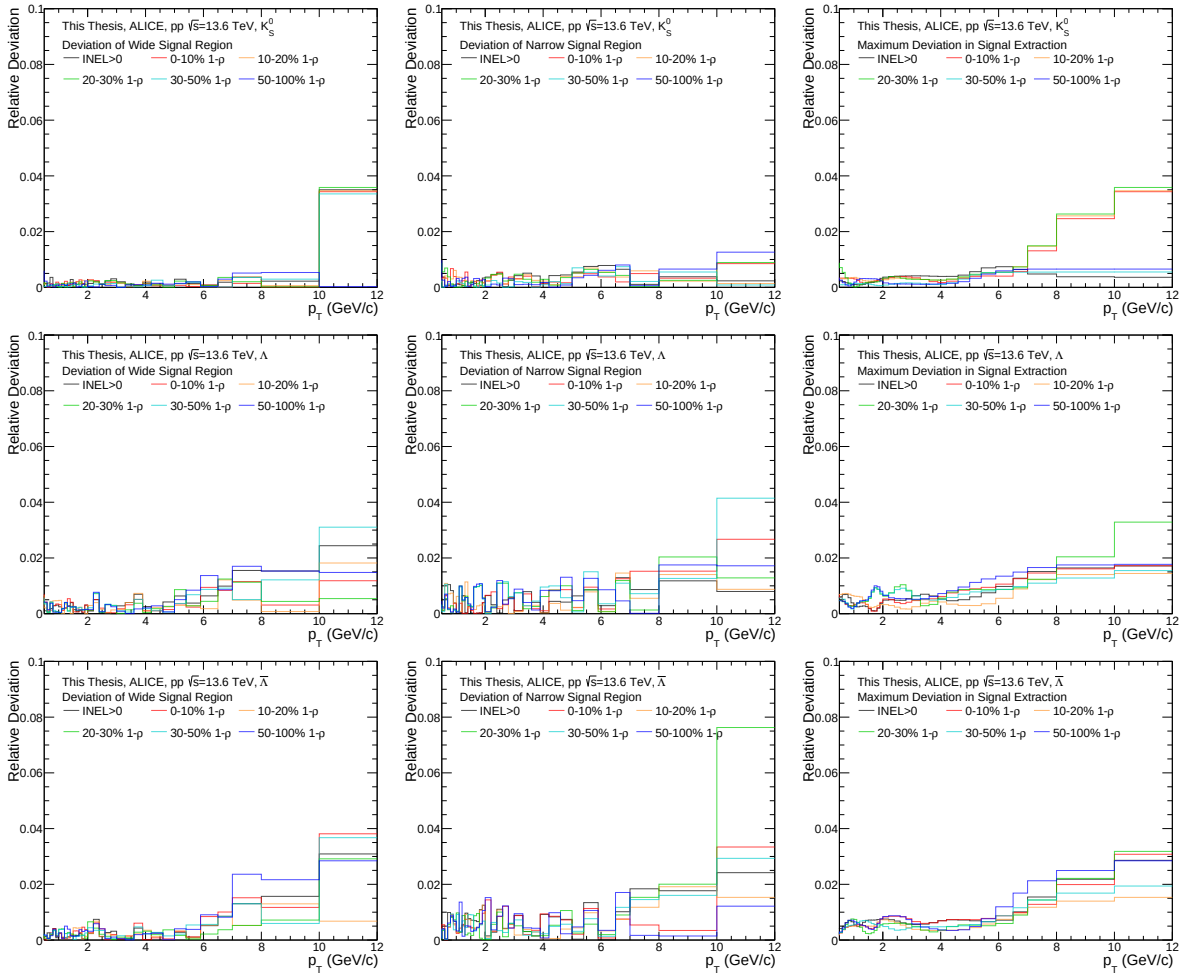

Figure 4.10: p_{T}-dependent relative deviation of measurements performed in wider (left column) and narrower (middle column) region of signal extraction as a function of flattenicity percentiles for K^0_{S} (upper row), Λ (middle row), and $\bar{\Lambda}$ (lower row) in pp collisions at $\sqrt{s} = 13.6$ TeV. The right column shows the maximum relative deviation with respect to the standard measurement, which is considered as the systematic error for the choice of signal region [89].

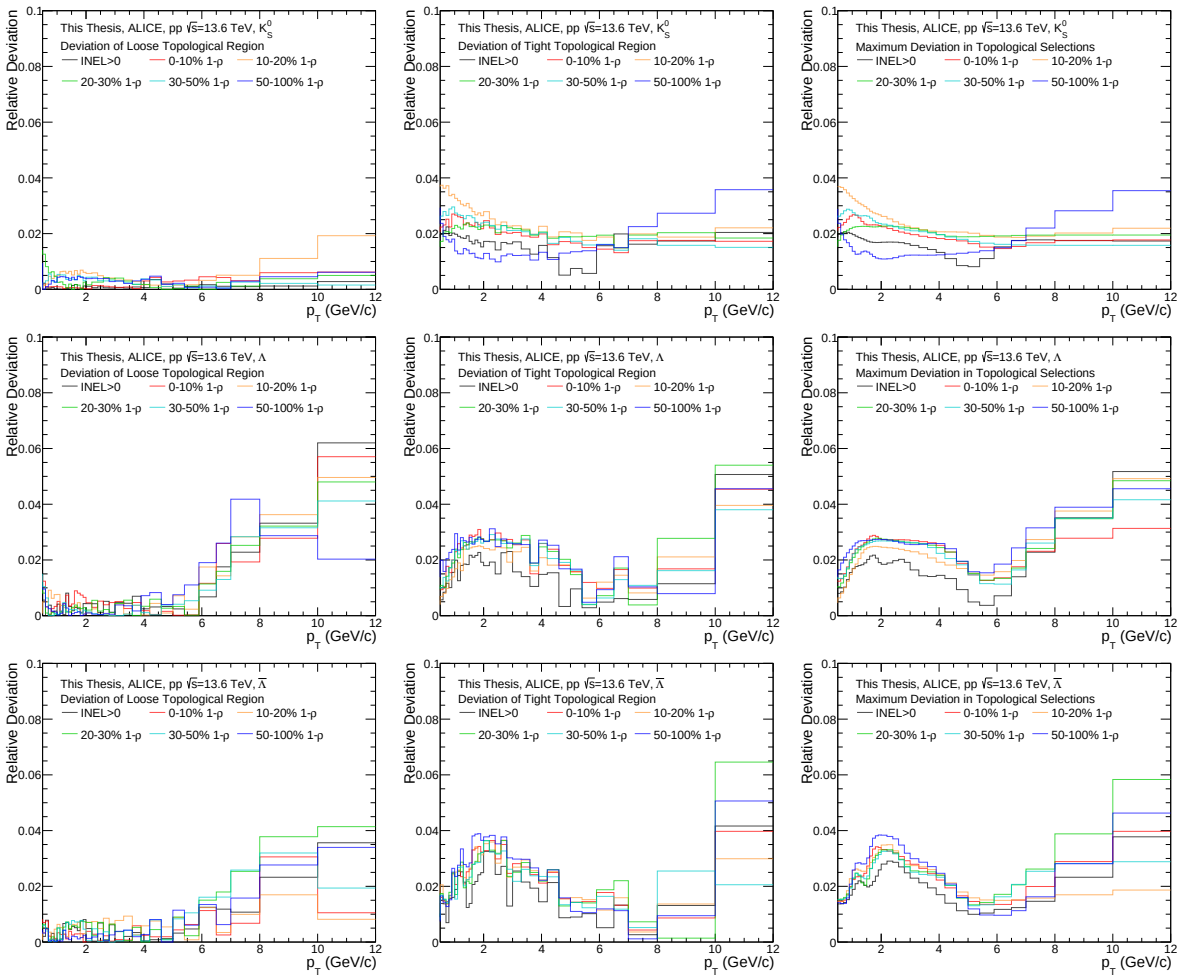

Figure 4.11: p_{T}-dependent relative deviation of measurements performed with loose (left column) and tight (middle column) topological and kinematic cuts as a function of flatenicity percentiles for K^0_{S} (upper row), Λ (middle row), and $\bar{\Lambda}$ (lower row) in pp collisions at $\sqrt{s} = 13.6$ TeV. The right column shows the maximum relative deviation with respect to the standard measurement, which is considered as the systematic error for the choice of signal region [89].

	Cuts		
Observable	**Loose**	**Standard**	**Tight**
DCA Negative Track to PV	> 0.055 cm	> 0.06 cm	> 0.07 cm
DCA Positive Track to PV	> 0.055 cm	> 0.06 cm	> 0.07 cm
TPC dE/dx selection	$< 6\sigma$	$< 5\sigma$	$< 4\sigma$
V^0 Decay Radius	> 0.4 cm	> 0.5 cm	> 0.6 cm
V^0 Cosine of PA	> 0.96 (0.994)	> 0.97 (0.995)	> 0.98 (0.996)
DCA V^0 daughters	< 1.25	< 1.0	< 0.75
Proper Lifetime	< 25 (35) cm	< 20 (30) cm	< 15 (25) cm

Table 4.3: Cut variation parameters for K^0_S (Λ) for the estimation of systematic uncertainties [89].

$\times$ efficiency correction factors from the INEL > 0 to correct the spectra of all the flattenicity classes. Since, the variation of acceptance $\times$ efficiency of individual flattenicity class from the INEL > 0 case is smaller than 3%, we have added this 3% variation in the calculations of systematic uncertainty.

After obtaining the systematic uncertainties from the above-mentioned sources, the net systematic uncertainty is shown in Fig. 4.12 for different classes of flattenicity and for K^0_S, Λ, and $\bar{\Lambda}$, from left to right, respectively.

4.7 Results and discussions

The section starts with a comparison of fully corrected p_T spectra of K^0_S compared with the Run 2 published ALICE results at $\sqrt{s} = 13$ TeV for INEL > 0 case, as shown in Fig. 4.13. Here, around 5% discrepancy between Run 2 and existing Run 3 measurements for K^0_S is observed, which is within the systematic uncertainty, shown in the left panel of Fig. 4.12.

Figure 4.14 shows the corrected p_T spectra for K^0_S (left), and inclusive-$\Lambda + \bar{\Lambda}$ (right) for different percentile classes of flattenicity in pp collisions at $\sqrt{s} = 13.6$ TeV. Here, inclusive $\Lambda + \bar{\Lambda}$ spectra refers to that obtained without the feed-down corrections from Ξ

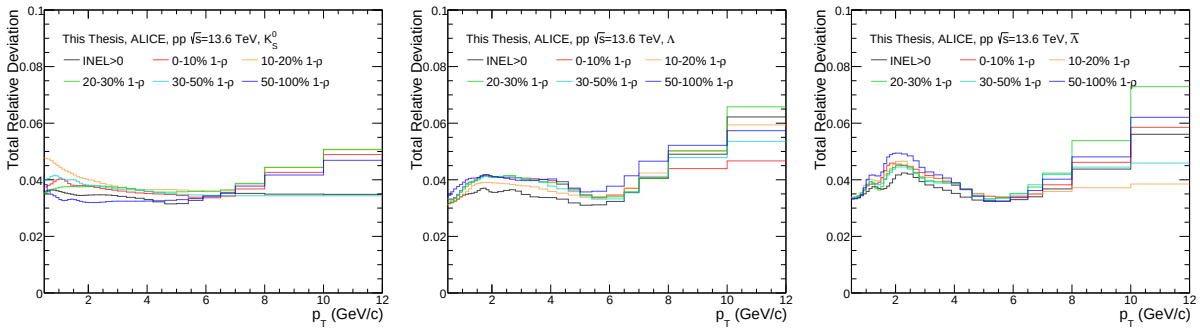

Figure 4.12: p_{T}-dependent total relative deviation of measurements performed with different signal and topological regions as a function of flattenicity percentiles for K^0_{S} (left), Λ (middle), and $\bar{\Lambda}$ (right) in pp collisions at $\sqrt{s}$ = 13.6 TeV with ALICE. An additional 3% systematic uncertainty contribution has been added for the acceptance×efficiency correction [89].

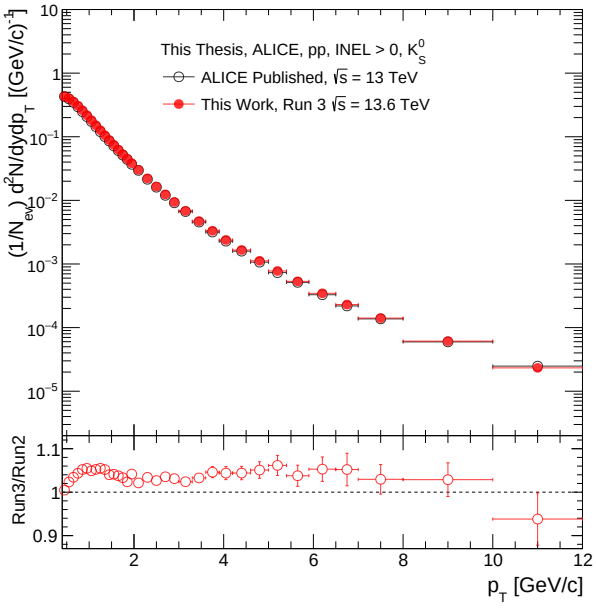

Figure 4.13: Comparison of fully corrected p_{T} spectra for K^0_{S} (left) measured for INEL > 0 events in pp collisions at $\sqrt{s}$ = 13.6 TeV with that of $\sqrt{s}$ = 13 TeV with Run 2 data [89]. The ALICE published results are taken from Ref. [97].

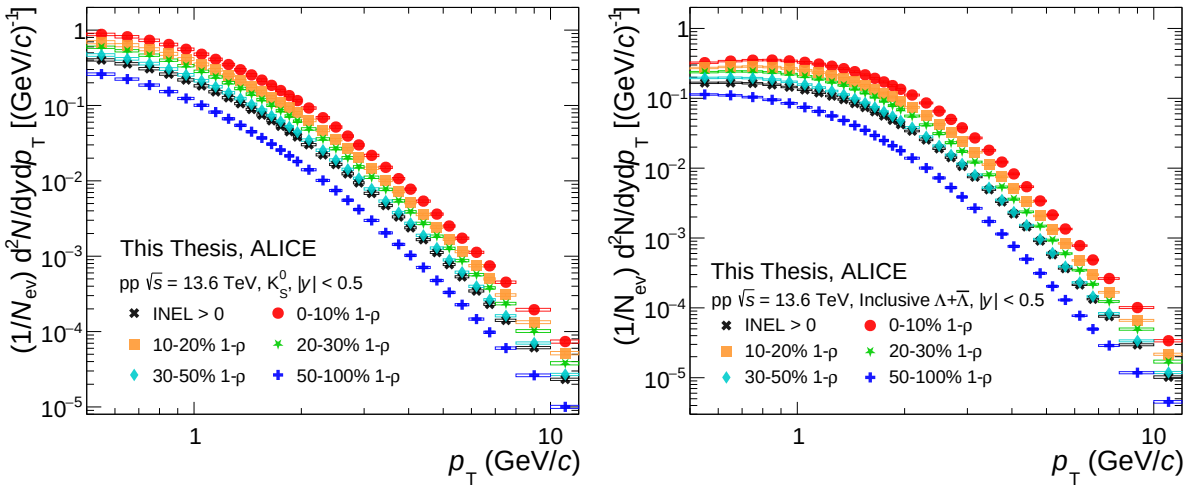

Figure 4.14: Corrected p_{T} spectra for K^0_{S} (left), Λ+$\bar{\Lambda}$ (right) for different percentile classes of flattenicity in pp collisions at $\sqrt{s} = 13.6$ TeV [89, 93].

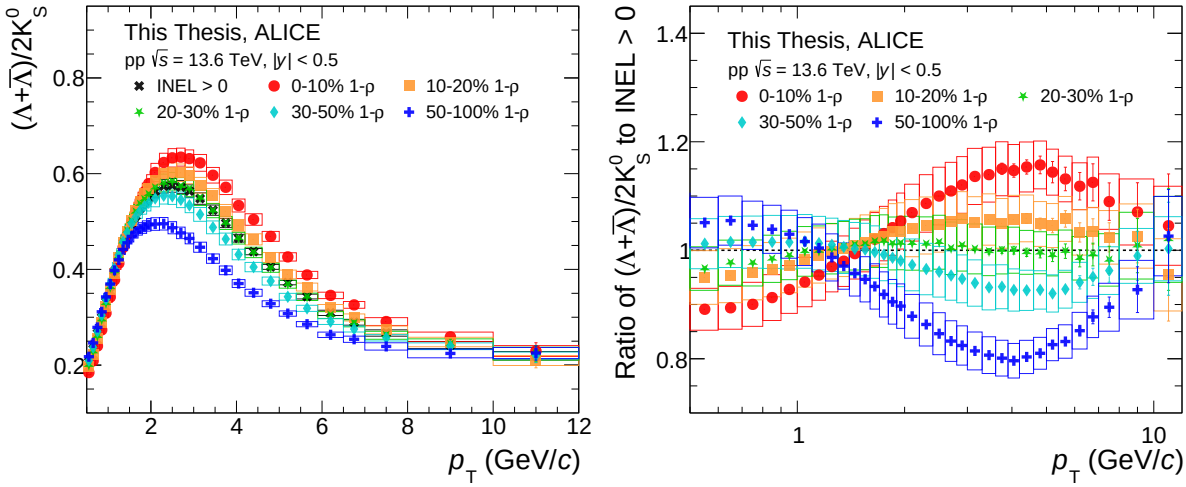

Figure 4.15: Left panel shows the $(\Lambda+\bar{\Lambda})/2K^0_{\mathrm{S}}$ for different flattenicity percentile classes in pp collisions at $\sqrt{s} = 13.6$ TeV with ALICE. The right pane shows the ratio of $(\Lambda+\bar{\Lambda})/2K^0_{\mathrm{S}}$ for each flattenicity class to INEL > 0 case [89, 93].

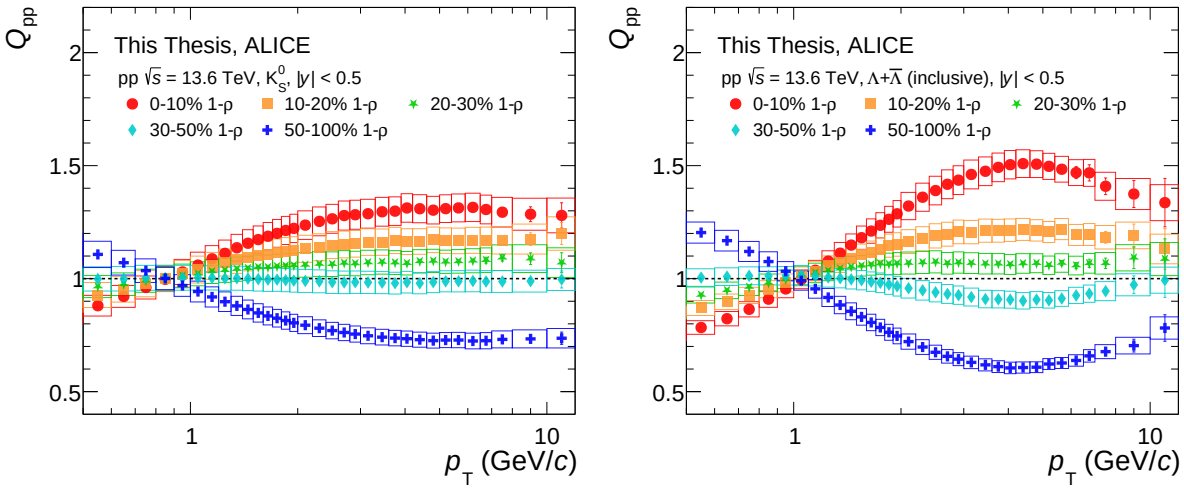

Figure 4.16: Q_{pp} of K^0_{S} (left) and $\Lambda + \bar{\Lambda}$ (right) for different flattenicity percentile classes in pp collisions at $\sqrt{s} = 13.6$ TeV with ALICE [89, 93].

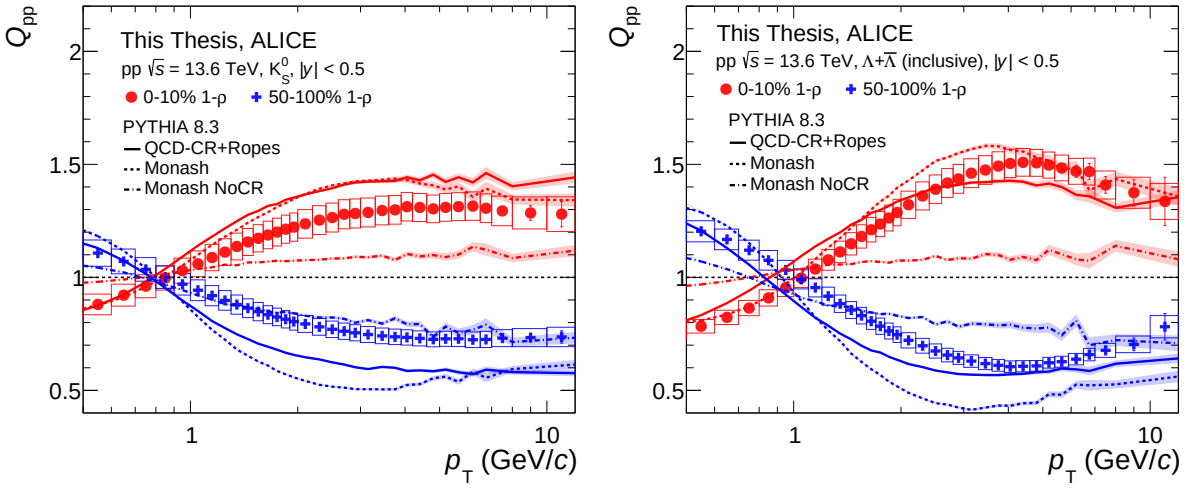

Figure 4.17: Q_{pp} of K^0_{S} (left) and $\Lambda + \bar{\Lambda}$ (right) for different flattenicity percentile classes in pp collisions at $\sqrt{s} = 13.6$ TeV with ALICE compared with results from different tunes of PYTHIA 8 [89, 93].

hadrons. Here, as one moves from lower to higher values of $(1-\rho)$ for all the V^0s, the yield increases, and a hardening in the p_T-spectra is also hinted, which is more prominent for $\Lambda+\bar{\Lambda}$ than that of K^0_S. The p_T spectra for $\Lambda+\bar{\Lambda}$ is harder compared to K^0_S. This can also be observed in the left panel of Fig. 4.15, where $(\Lambda+\bar{\Lambda})/2K^0_S$ is shown as a function of p_T for different classes of flattenicity in pp collisions at $\sqrt{s} = 13.6$ TeV. The peak structure in $(\Lambda+\bar{\Lambda})/2K^0_S$ can arise due to a harder p_T-spectra of $\Lambda+\bar{\Lambda}$ than K^0_S or due to strong regeneration effects, which is absent in pp collisions. Here, within the uncertainties, one can observe a shift in the peak positions of $(\Lambda+\bar{\Lambda})/2K^0_S$ towards lower p_T values as one moves to higher values of $(1-\rho)$ indicating the presence of radial flow signals. These descriptions in the baryon-to-meson ratios are well-described by MPI-based models [57, 58]. To highlight the shift of the peak positions in p_T for different classes of flattenicity, in the right panel of Fig. 4.15, we show the ratio of $(\Lambda+\bar{\Lambda})/2K^0_S$ for each flattenicity classes w.r.t. the INEL > 0 case. As one moves from 50-100% $(1-\rho)$ to 0-10% $(1-\rho)$, the peak position shifts towards a higher p_T region. This indicates the significance of applying flattenicity-based event selection to choose softer events, leading to the broadening of spectra and the observations of radial flow-like signatures.

Figure 4.16 shows Q_{pp}, defined in Eq. (4.1), as a function of transverse momentum for K^0_S (left) and $\Lambda+\bar{\Lambda}$ (right) measured in pp collisions at $\sqrt{s} = 13.6$ TeV. Similar to Fig. 4.15, the left and right panels of Fig. 4.16 show the effect of spectra hardening as a function of charged particle flattenicity. Additionally, towards the higher values of p_T, Q_{pp} is found to converge towards 1, which shows that the measurements performed as a function of charged particle flattenicity are minimally affected by selection bias. It is important to note that, although the feed-down corrections have not been implemented for Λ and $\bar{\Lambda}$, the results shown in right panel of Fig. 4.15 and Fig. 4.16 are independent of feed-down correction. This is because the calculation of these quantities involves the ratio to INEL > 0 case which cancels out the feed-down effects. Results from PYTHIA 8 with Monash and QCD-CR+Ropes (Color Ropes), which have radial flow-like signals, agree qualitatively with the experimental measurements, as shown in Fig. 4.17, while PYTHIA8 Monash NoCR fails to explain the experimental measurements. In Figs. 4.15 (right panel), 4.16 and 4.17, a crossing is observed near $p_T \sim 1$ GeV/c, which arises as a consequence qualitative differences in the p_T-spectra, originating due to the presence of

radial flow in the system. In Fig. 4.16, it is interesting to see that the crossing occurs at a higher p_{T} for $\Lambda + \bar{\Lambda}$ than K^0_{S}. This is because the radial flow affects $\Lambda + \bar{\Lambda}$ strongly as compared to K^0_{S}, thus making the spectra of $\Lambda + \bar{\Lambda}$ harder than that of K^0_{S}, which shifts the crossing point to a slightly higher p_{T} value for $\Lambda + \bar{\Lambda}$. This is validated in the right panel of Fig. 4.17, where the crossing of Q_{pp} for $\Lambda + \bar{\Lambda}$ in the PYTHIA8 Monash NoCR (weak radial flow feature) case occurs at a smaller p_{T} value as compared to Monash and Color Ropes cases.

4.8 Summary

In summary, this analysis aims to measure the neutral strange hadron production as a function of charged particle flattenicity in pp collisions at $\sqrt{s} = 13.6$ TeV with LHC Run 3 of data taking at ALICE. This study aims to probe the strangeness enhancement and radial-flow signatures recently observed in high multiplicity pp collisions.

This chapter discusses first measurements of flattenicity in Run 3 at ALICE. Moreover, the minimum bias and flattenicity dependence of the raw p_{T}-differential yield of K^0_{S}, $\Lambda + \bar{\Lambda}$ are determined. Acceptance $\times$ efficiency, signal and event loss correction factors are calculated and applied to the raw spectra to obtain the corrected p_{T}-spectra of K^0_{S}. Systematic uncertainties from different sources are also calculated. Moreover, the transverse momentum spectra of K^0_{S} ,and $\Lambda+\bar{\Lambda}$ for INEL > 0 events and for different percentile slices of charged particle flattenicity are calculated, which shows that events with larger values of $(1-\rho)$ show stronger spectra hardening. $(\Lambda + \bar{\Lambda})/2K^0_{\mathrm{S}}$ are also measured for different classes of flattenicity to investigate the radial flow signal. The events with $(1-\rho) \to 1$ show stronger signals of radial flow-like effects. The measurement of Q_{pp} yields an interesting observation. Here, towards higher p_{T}, Q_{pp} for both K^0_{S}, and $\Lambda+\bar{\Lambda}$ flattens out. This hints that the selection biases are negligible when event selection is performed based on charged particle flattenicity.

4.9 Appendix

4.9.1 Data sample

1. Data: LHC24_pass1_minBias

   - LHC24af_apass1_sampled

     Run Numbers: 550916, 550889, 550858, 550852, 550848, 550843, 550824, 550819, 550784, 550781, 550778, 550774, 550760, 550756, 550742, 550731, 550728, 550711, 550707, 550691, 550690, 550654, 550653, 550634, 550632, 550630, 550439, 550425, 550424, 550421, 550417, 550412, 550375, 550369, 550367

   - LHC24ag_apass1_sampled

     Run Numbers: 551504, 551498, 551468, 551463, 551427, 551418, 551398, 551394, 551392, 551391, 551389, 551387, 551365, 551296, 551290, 551272, 551260, 551257, 551255, 551232, 551230, 551229, 551221, 551219, 551149, 551127, 551122, 551107, 551105, 551083, 551066, 551027, 551023, 551013, 551008, 551007, 551005, 550997

   - LHC24aj_apass1_sampled

     Run Numbers: 552403, 552402, 552401, 552400, 552384, 552383, 552382, 552381, 552369, 552353, 552341, 552340, 552304, 552285, 552283, 552206, 552205, 552204, 552203, 552201, 552200, 552198, 552197, 552179, 552178, 552177, 552176, 552156, 552142, 552141, 552140, 552139, 552138, 552103, 552102, 552080, 552029, 552005, 551997, 551993, 551992, 551989, 551983, 551982, 551979, 551977, 551958, 551943, 551931, 551926, 551925, 551924, 551923, 551922, 551921, 551894, 551890, 551889, 551877, 551875, 551874, 551856, 551843, 551780, 551761, 551760, 551759

   - LHC24al_apass1_sampled

     Run Numbers: 555308, 555270, 555267, 555259, 555254, 555232, 555226, 555208, 555202, 555187, 555172, 555166, 555160, 555156, 555152, 555150, 555124, 555122, 555121, 555073, 555071, 555047, 555023, 555022, 555020, 554998, 554973, 554970, 554968, 554920, 554898, 554880, 554873, 554837, 554835,

554808, 554791, 554774, 554772, 554768, 554752, 554736, 554732, 554728, 554714, 554703, 554701, 554633, 554615, 554613, 554603, 554588, 554569, 554564, 554558, 554538, 554526, 554524, 554507, 554504, 554495, 554494, 554471, 554462, 554427, 554413, 554408, 554404, 554394, 554354, 554323, 554322, 554316, 554295, 554293, 554261, 554247, 554223, 554208, 554207, 554203, 554201, 554198, 554194, 554098, 554097, 554095, 554094, 554092, 553903, 553880, 553862, 553844, 553825, 553824, 553821, 553819, 553816, 553807, 553785, 553756, 553739, 553702, 553700, 553663, 553660, 553655, 553633, 553610, 553590, 553588, 553555, 553536, 553530, 553512, 553486, 553305, 553299, 553297, 553294, 553274, 553255, 553253, 553250, 553225, 553219, 553193, 553189, 553188, 553187, 553185

- LHC24am_apass1_sampled

  Run Numbers: 555960, 555958, 555933, 555917, 555900, 555860, 555853, 555850, 555801, 555798, 555790, 555789, 555763, 555761, 555759, 555742, 555740, 555723, 555722, 555707, 555705, 555695, 555693, 555676, 555651, 555649, 555612, 555596, 555591, 555575, 555546, 555543, 555540, 555504, 555482, 555478, 555476, 555451, 555443, 555435, 555431, 555411, 555408, 555401, 555374, 555370, 555345, 555344

- LHC24an_apass1_sampled

  Run Numbers: 557926, 557913, 557897, 557876, 557862, 557749, 557744, 557726, 557723, 557717, 557691, 557681, 557659, 557613, 557547, 557531, 557509, 557482, 557481, 557444, 557425, 557415, 557374, 557350, 557339, 557336, 557321, 557299, 557291, 557271, 557251, 557233, 557226, 557149, 557138, 557119, 557118, 557112, 557104, 557074, 557026, 557021, 557019, 557012, 556997, 556981, 556979, 556958, 556954, 556939, 556767, 556741, 556734, 556716, 556680, 556664, 556662, 556641, 556640, 556639, 556562, 556542, 556517, 556497, 556491, 556485, 556482, 556461, 556454, 556437, 556412, 556372, 556370, 556284, 556269, 556248, 556237, 556218, 556210, 556182, 556164, 556160, 556152

- LHC24ao_apass1_sampled

  Run Numbers: 558801, 558783, 558757, 558752, 558750, 558744, 558726, 558685,

558676, 558656, 558633, 558627, 558615, 558606, 558604, 558602, 558551, 558535, 558482, 558449, 558437, 558433, 558422, 558410, 558409, 558406, 558390, 558387, 558383, 558369, 558354, 558330, 558329, 558291, 558288, 558284, 558275, 558273, 558247, 558244, 558221, 558217, 558215, 558182, 558179, 558155, 558153, 558150, 558126, 558124, 558122

2. Monte Carlo (anchored to `LHC24_pass1_minBias`): LHC24f4d (pp)

   Run Numbers: 550367, 550369, 550375, 550412, 550417, 550421, 550424, 550425, 550439, 550630, 550632, 550634, 550653, 550654, 550690, 550691, 550707, 550711, 550728, 550731, 550742, 550756, 550760, 550774, 550778, 550781, 550784, 550819, 550824, 550843, 550848, 550852, 550858, 550889, 550916, 550997, 551005, 551007, 551008, 551013, 551023, 551027, 551066, 551083, 551105, 551107, 551122, 551127, 551149, 551219, 551221, 551229, 551230, 551232, 551255, 551257, 551260, 551272, 551290, 551296, 551365, 551387, 551389, 551391, 551392, 551394, 551398, 551418, 551427, 551463, 551468, 551498, 551504, 551759, 551760, 551761, 551780, 551843, 551856, 551874, 551875, 551877, 551889, 551890, 551894, 551921, 551922, 551923, 551924, 551925, 551926, 551931, 551943, 551958, 551977, 551979, 551982, 551983, 551989, 551992, 551993, 551997, 552005, 552029, 552080, 552102, 552103, 552138, 552139, 552140, 552141, 552142, 552156, 552176, 552177, 552178, 552179, 552197, 552198, 552200, 552201, 552203, 552204, 552205, 552206, 552283, 552285, 552304, 552340, 552341, 552353, 552369, 552381, 552382, 552383, 552384, 552400, 552401, 552402, 552403, 553185, 553187, 553188, 553189, 553193, 553219, 553225, 553250, 553253, 553255, 553274, 553294, 553297, 553299, 553305, 553486, 553512, 553530, 553536, 553555, 553588, 553590, 553610, 553633, 553655, 553660, 553663, 553700, 553702, 553739, 553756, 553785, 553807, 553816, 553819, 553821, 553824, 553825, 553844, 553862, 553880, 553903, 554092, 554094, 554095, 554097, 554098, 554194, 554198, 554201, 554203, 554207, 554208, 554223, 554247, 554261, 554293, 554295, 554316, 554322, 554323, 554354, 554394, 554404, 554408, 554413, 554427, 554462, 554471, 554494, 554495, 554504, 554507, 554524, 554526, 554538, 554558, 554564, 554569, 554588, 554603, 554613, 554615, 554633, 554701, 554703, 554714, 554728, 554732, 554736, 554752, 554768, 554772, 554774, 554791, 554808, 554835, 554837, 554873, 554880, 554898, 554920, 554968, 554970, 554973, 554998, 555020, 555022,

555023, 555047, 555071, 555073, 555121, 555122, 555124, 555150, 555152, 555156, 555160, 555166, 555172, 555187, 555202, 555208, 555226, 555232, 555254, 555259, 555267, 555270, 555308, 555344, 555345, 555370, 555374, 555398, 555401, 555408, 555411, 555431, 555435, 555443, 555451, 555476, 555478, 555482, 555504, 555540, 555543, 555546, 555575, 555591, 555596, 555612, 555649, 555651, 555676, 555693, 555695, 555705, 555707, 555722, 555723, 555740, 555742, 555759, 555761, 555763, 555789, 555790, 555798, 555801, 555850, 555853, 555860, 555881, 555883, 555900, 555917, 555933, 555958, 555960, 555965, 555967, 555976, 556152, 556160, 556164, 556182, 556210, 556218, 556237, 556248, 556269, 556284, 556370, 556372, 556412, 556437, 556454, 556461, 556482, 556485, 556491, 556497, 556517, 556542, 556562, 556639, 556640, 556641, 556662, 556664, 556680, 556716, 556734, 556741, 556767, 556816, 556834, 556872, 556889, 556907, 556909, 556913, 556923, 556939, 556954, 556958, 556979, 556981, 556997, 557012, 557019, 557021, 557026, 557074, 557104, 557112, 557118, 557119, 557138, 557149, 557226, 557233, 557251, 557271, 557291, 557299, 557321, 557336, 557339, 557350, 557374, 557415, 557425, 557444, 557481, 557482, 557509, 557531, 557547, 557613, 557659, 557681, 557691, 557717, 557723, 557726, 557744, 557749, 557862, 557876, 557897, 557913, 557926, 558122, 558124, 558126, 558150, 558153, 558155, 558179, 558182, 558215, 558217, 558221, 558244, 558247, 558273, 558275, 558284, 558288, 558291, 558327, 558329, 558330, 558354, 558369, 558383, 558387, 558390, 558406, 558409, 558410, 558422, 558433, 558437, 558449, 558482, 558535, 558551, 558602, 558604, 558606, 558615, 558627, 558633, 558656, 558676, 558685, 558726, 558744, 558750, 558752, 558757, 558783, 558801

Chapter 5

Exploring collectivity in heavy-ion collisions using event-shape engineering

Based on:

1. *S. Prasad, N. Mallick, D. Behera, R. Sahoo and S. Tripathy, "Event topology and global observables in heavy-ion collisions at the Large Hadron Collider", Sci. Rep. 12, 3917 (2022).*

2. *S. Prasad, N. Mallick, S. Tripathy, and R. Sahoo, "Probing initial geometrical anisotropy and final azimuthal anisotropy in heavy-ion collisions at Large Hadron Collider energies through event-shape engineering", Phys. Rev. D 107, 074011 (2023).*

3. *S. Prasad, A. Menon. K. R, R. Sahoo, and N. Mallick, "Higher order flow coefficients – A Messenger of QCD medium formed in heavy-ion collisions at the Large Hadron Collider", Phys. Lett. B 868, 139753 (2025).*

5.1 Introduction and motivation

The event shape studies at the GeV and TeV energies, due to their ability to segregate the p-QCD-dominated hard events from soft-QCD-dominated isotropic events, have received

some level of importance in elementary and hadronic collisions. In contrast, in heavy-ion collisions, because of a dense medium formation, event topology techniques like transverse spherocity, sphericity, R_{T}, etc., are not explored. This chapter discusses some of the important applications of event shape classifiers in heavy-ion collisions.

One of the traditional event-shape classifiers used in heavy-ion collisions is the reduced flow vectors (q_n), defined as follows [98, 99]:

$$q_n = \frac{|Q_n|}{\sqrt{M}}, \tag{5.1}$$

where,

$$Q_n = \sum_{j=1}^{M} e^{in\phi_j} \tag{5.2}$$

Here, M is the total number of charged particles in a given rapidity region, ϕ_j is the azimuthal angle of the jth charged particle. Q_n is often referred to as the flow vector. Primarily, q_n are used to study nth order anisotropic flow coefficients (v_n) as they possess significant correlations with them [100]. In fact, at large multiplicities, v_n can be expanded in terms of corresponding q_n, as a linear equation [100]. However, there is one caveat: with a decrease in multiplicity, correlations between q_n and v_n get weaker [100]. Although this effect is negligible for central to mid-central Pb–Pb collisions at the LHC, the implications of q_n vectors at low-multiplicity environments need special care. Further, for the new collision systems, such as Ne-Ne and O-O at the LHC, one needs to be cautious before applying q_n based event shape selections. Thus, it is important to look for new event classifiers, which can be efficient in both high and low multiplicity environments. One such event classifier is transverse spherocity[1] (S_0) [34, 58, 101–103], which is widely used in proton-proton collisions, and a few studies hint at its applicability in heavy-ion collisions [22, 104–108].

One of the important properties of QGP, collective flow, is often studied with radial flow of the system and anisotropic flow coefficients. The anisotropic flow coefficients are also related to the geometry of the final state particles' momentum distribution. The collision overlap region in non-central heavy-ion collisions is almond-shaped, which reflects as finite elliptic flow (v_2) in the final state. Similarly, the fluctuations in the position of the participating nucleons lead to density fluctuations in the collision overlap region

[1]See Chapter 2 for definition.

and anisotropic flow coefficients of third (triangular flow, v_3) and higher order (v_n for $n \geq 4$) are generated. These anisotropic flow coefficients of different orders are sensitive to transport properties of the system formed in heavy-ion collisions. The sensitivity differs for different orders of anisotropic flow coefficients. Elliptic flow, v_2, is least sensitive to system response via transport properties, while the sensitivity increases with an increase of n in v_n. However, v_2 and v_3 interfere with the measurements of higher order v_n. v_4 and v_5 can arise from the initial eccentricities of similar order and non-linear mixing of v_2 and v_3. In fact, the measured v_4 can be expressed as linear contribution from ϵ_4, and a nonlinear contribution from ϵ_2 or v_2, i.e. [109, 110],

$$\begin{aligned} v_4 e^{i4\Phi_4} &= a_0 \epsilon_4 e^{i4\psi_4} + a_1 (\epsilon_2 e^{i2\psi_2})^2 + \dots \\ &= c_0 e^{i4\psi_4} + c_1 (v_2 e^{i2\Phi_2})^2 + \dots . \end{aligned} \tag{5.3}$$

Here, Φ_n is called event plane angle and $c_0 = a_0\epsilon_4$ is the linear component of v_4. Moreover, a_0, a_1 and c_1 vary weakly with collision centrality. This nonlinear contribution of v_2 in the measured value of v_4 led to strong centrality dependence of the correlation between ψ_2 and ψ_4 [109]. Similar to v_4, v_5 has linear contributions from ϵ_5 and nonlinear contributions from both v_2 and v_3 [109, 110]:

$$\begin{aligned} v_5 e^{i5\Phi_5} &= a_0 \epsilon_5 e^{i5\psi_5} + a_1 \epsilon_2 e^{i2\psi_2} \epsilon_3 e^{i3\psi_3} + \dots \\ &= c_0 e^{i5\psi_5} + c_1 v_2 v_3 e^{i(2\Phi_2 + 3\Phi_3)} + \dots \end{aligned} \tag{5.4}$$

This nonlinear contributions of v_2 and v_3 in the measured v_5 led to the observed event plane correlations involving ψ_2, ψ_3, and ψ_5 in experiments [111]. This measurement was performed using the event plane method, where correlations among the anisotropic flow coefficients affect corresponding correlations among symmetry plane angle, which is absent for correlations estimated using the Gaussian estimator method [112]. Therefore, it is necessary to decouple the linear and non-linear contributions in the measured signal of higher-order harmonics. The event shape engineering techniques are one of the ways to separate the non-linear contributions of v_2 and v_3 from v_4 and v_5.

The chapter is organised as follows. We start with a brief introduction and motivation for the study in Section 5.1. The event generation using a multi-phase transport model is discussed in Section 5.2. The methodology of estimation of anisotropic flow coefficients

is shown in Section 5.3. The results are presented in Section 5.4 along with necessary discussions. Finally, the findings are summarised in Section 5.5.

5.2 A multi-phase transport model (AMPT)

AMPT is a widely used Monte Carlo event generator primarily used to simulate A-A and p-A collisions at the RHIC and LHC energies [113, 114]. AMPT has four primary physics components that mimic different evolution stages of heavy-ion collisions, which are listed and discussed as follows.

- **Initialisation of collisions**: The initialisation of collisions in AMPT is performed using the heavy-ion jet interaction generator (HIJING) [115]. In this model, a differential production cross-section of minijet partons in pp collisions is calculated and converted into p-A and A-A collisions by incorporating shadowing and nuclear overlap functions from the inbuilt Glauber Model [116].

- **Parton transport**: After the initialisation of the collisions, the produced partons are transported through Zhang's parton cascade (ZPC) model [117]. ZPC includes partonic interactions via two-body elastic scatterings. The parton scattering cross-sections are obtained from p-QCD with screening masses. In the string melting version of AMPT (AMPT-SM), the colored strings formed during the initialisation of collisions melt into low-momentum partons.

- **Hadronisation**: After the parton transport, the partons are hadronised to form hadrons. AMPT has two different models for hadronisation. In the default version of AMPT, the transported partons are recombined with their parent strings and hadronise via the Lund string fragmentation model [60]. In the AMPT-SM model, the transported partons hadronise via the quark coalescence mechanism [118].

- **Hadron transport**: In this stage, the produced hadrons undergo hadron transport using a relativistic transport (ART) model [119, 120]. ART model includes meson-meson, baryon-baryon and meson-baryon interactions.

Although the default model of AMPT can well describe particle spectra at both SPS and RHIC energies, it significantly underestimates the particle elliptic flow at the RHIC

energies. This is because in the default version of AMPT, only minijet partons participate in the parton transport, which makes the parton density relatively lower to produce any medium effects. On the other hand, in the AMPT-SM model, the excited strings are converted to partons and are combined with minijet partons to mimic the necessary medium effect. Moreover, the coalescence mechanism in the AMPT-SM model is also responsible for propagating the partonic flow to hadrons. Thus, the results shown in this chapter are based on AMPT-SM models, which are used to simulate Pb-Pb collisions at $\sqrt{s}_{\rm NN} = 5.02$ TeV.

5.3 Methodology

In this section, we discuss the procedures to estimate anisotropic flow coefficients and initial eccentricities.

5.3.1 Anisotropic flow

Anisotropic flow can quantify the azimuthal momentum anisotropy of the final state particles. It is expressed in terms of the coefficients of the Fourier expansion of the azimuthal distribution of the final state particles in momentum space, given by [23];

$$\frac{dN}{d\phi} \propto 1 + 2\sum_{n=1}^{\infty} v_n \cos[n(\phi - \psi_n)], \tag{5.5}$$

where, ϕ and ψ_n are the azimuthal and nth harmonic symmetry plane angles [23, 121]. n denotes the order of the harmonics, and the coefficients v_n quantify the nth order anisotropic flow coefficients, which can be calculated using the following equation [22, 122, 123]:

$$v_n = \langle \cos[n(\phi - \psi_n)] \rangle \tag{5.6}$$

Eq. (5.6) is prone to contributions from non-flow effects. Further, the experimental measurements of ψ_n are not trivial, which attests to the need for a new method of estimating anisotropic flow coefficients. Moreover, since in this chapter I am dealing with different topological events, therefore, in order to see the fair dependence of event topology, I shall use two-particle correlation and multi-particle cumulants method to study the anisotropic flow coefficients, which are discussed below in detail.

5.3.1.1 Two-particle correlations

The two-particle correlation method is one of the few methods that can deal with the non-flow effects caused by jets and resonance decays by implementing a proper relative pseudorapidity ($\Delta\eta$) cut between the pairs of particles [100, 124, 125]. Additionally, this method does not need ψ_n to calculate v_n, which is not trivial in experiments. The following steps are involved in calculating the two-particle correlation function.

- Two sets of particles based on their p_{T} are composed, which are denoted by labels 'a' and 'b'.
- Each particle in 'a' pairs with that of in 'b'.
- The relative pseudorapidities ($\Delta\eta = \eta_a - \eta_b$) and relative azimuthal angles ($\Delta\phi = \phi_a - \phi_b$) of particle pairs are calculated.
- The same event pair, $S(\Delta\eta, \Delta\phi)$, is calculated as the particle pair number distribution from the same event ('a' and 'b' belong to the same event) as a function of $\Delta\eta$, and $\Delta\phi$.
- The mixed-event pair distribution ($B(\Delta\eta, \Delta\phi)$) is calculated as the number distribution of particle pairs from 'a' and 'b', where 'b' belong to five randomly chosen events which are different from that of 'a'.
- Two-particle correlation function ($C(\Delta\eta, \Delta\phi)$) is calculated as the ratio of $S(\Delta\eta, \Delta\phi)$ to $B(\Delta\eta, \Delta\phi)$, which improves the pair acceptance and ensures no non-uniformity.

To remove the contribution of non-flow, a $\Delta\eta$ cut ($2 \leq |\Delta\eta| \leq 5$) in $S(\Delta\eta, \Delta\phi)$ and $B(\Delta\eta, \Delta\phi)$ is applied which is projected to $S(\Delta\phi)$ and $B(\Delta\phi)$ distributions, respectively. Further, the ratio, $C(\Delta\phi)$, is calculated, which is known as the 1D two-particle correlation function and can be expressed as follows.

$$C(\Delta\phi) = \frac{dN_{\mathrm{pairs}}}{d\Delta\phi} = A \times \frac{S(\Delta\phi)}{B(\Delta\phi)} = A \times \frac{\int S(\Delta\eta, \Delta\phi) d\Delta\eta}{\int B(\Delta\eta, \Delta\phi) d\Delta\eta} \tag{5.7}$$

where $A = \mathrm{N}_{\mathrm{pairs}}^{\mathrm{mixed}}/\mathrm{N}_{\mathrm{pairs}}^{\mathrm{same}}$ is the normalisation constant. $\mathrm{N}_{\mathrm{pairs}}^{\mathrm{mixed}}$ and $\mathrm{N}_{\mathrm{pairs}}^{\mathrm{same}}$ are the number of mixed event and same event pairs, respectively. $\Delta\phi$ can be Fourier expanded as follows:

$$C(\Delta\phi) = \frac{dN_{\mathrm{pairs}}}{d\Delta\phi} \propto [1 + 2\sum_{n=1}^{\infty} v_{n,n}(p_{\mathrm{T}}^a, p_{\mathrm{T}}^b) \cos n\Delta\phi]. \tag{5.8}$$

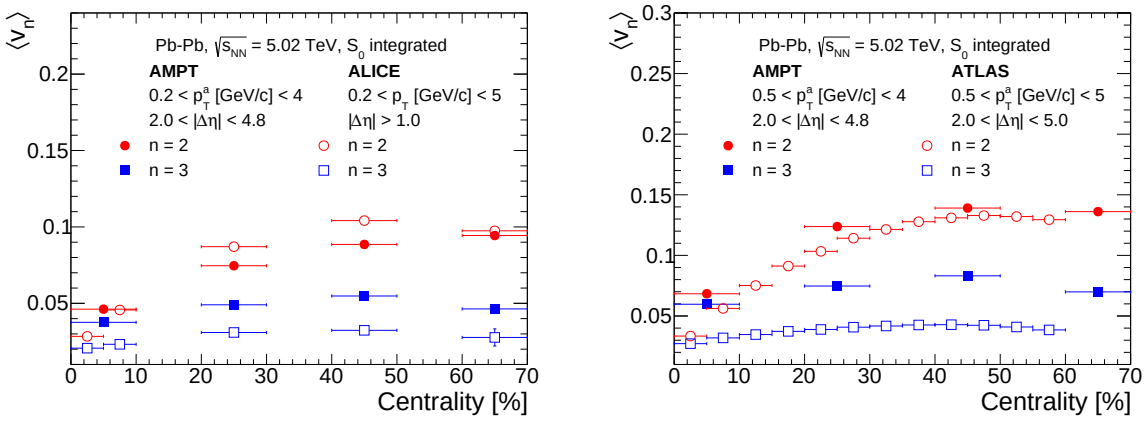

Figure 5.1: $\langle v_n \rangle$ vs centrality in Pb–Pb collisions at $\sqrt{s_{NN}}$ = 5.02 TeV using AMPT compared with similar measurements from ALICE [24] (left) and ATLAS [126] (right) [22].

Here, $v_{n,n}$ are called two-particle flow coefficients, which can be calculated by the discrete Fourier transformation as:

$$v_{n,n}(p_T^a, p_T^b) = \langle \cos n\Delta\phi \rangle = \frac{\sum_{m=1}^{N} \cos(n\Delta\phi_m) C(\Delta\phi_m)}{\sum_{m=1}^{N} C(\Delta\phi_m)}, \tag{5.9}$$

where N (=200) is the number of bins in range $-\pi/2 < \Delta\phi < 3\pi/2$ of $\Delta\phi$ distribution. Anisotropic flow coefficients shown in Eq. 5.5 contributes to Eq. 5.8 as:

$$C(\Delta\phi) \propto [1 + 2\sum_{n=1}^{\infty} v_n(p_T^a) v_n(p_T^b) \cos n\Delta\phi] \tag{5.10}$$

In Eq. 5.10, symmetry plane angles cancel out, leaving only the dependence on azimuthal angle of particle pairs. If one assumes that the anisotropic flow is driven by the collectivity of the system, then the two-particle flow coefficient ($v_{n,n}$) should be the product of two single-particle flow coefficients, as follows.

$$v_{n,n}(p_T^a, p_T^b) = v_n(p_T^a) v_n(p_T^b) \tag{5.11}$$

Contrariwise, v_n can be calculated from $v_{n,n}$ by using the following expression

$$v_n(p_T^a) = \frac{v_{n,n}(p_T^a, p_T^b)}{\sqrt{v_{n,n}(p_T^b, p_T^b)}} \tag{5.12}$$

Note that a negative value of $v_{n,n}(p_T^b, p_T^b)$ which can arise due to large fluctuations and non-flow contributions, in Eq. 5.12 can make $v_n(p_T^a)$ imaginary which is not physical. The correlation functions and the anisotropic flow coefficients of different orders are calculated

in the pseudorapidity gap of $2 < |\Delta\eta| < 4.8$ with particles having $0.5 < p_{\mathrm{T}} < 5$ GeV/c, when using the two-particle correlation method.

Figure 5.1 shows $\langle v_n \rangle$ as a function of centrality in Pb–Pb collisions at $\sqrt{s_{\mathrm{NN}}} = 5.02$ TeV using AMPT compared with similar measurements from ALICE [24] (left) and ATLAS [126] (right) [22]. In the left panel, $\langle v_2 \rangle$ from AMPT using two-particle correlation methods underestimates the ALICE measurements. However, $\langle v_3 \rangle$ from AMPT overestimates the measurements from the ALICE experiment. In contrast, the right panel shows an overestimation in both $\langle v_2 \rangle$ and $\langle v_3 \rangle$ (larger for $\langle v_3 \rangle$) measurements from AMPT with those of ATLAS measurements.

5.3.1.2 Multi-particle cumulant method

Similar to multi-particle correlations, the multi-particle cumulant method, which is usually used to calculate the anisotropic flow coefficients with reduced contributions from non-flow sources, by implementing a suitable $\Delta\eta$ cut. Since the multi-particle cumulants are faster, which rely upon the flow vectors of the events instead of calculating particle correlations of individual particle pairs, it is a preferable method to calculate higher moments of flow coefficients, which include but are not limited to flow fluctuations [127–129]. Since we aim to estimate the anisotropic flow and its fluctuations, we measure two- and four-particle cumulants, estimated using the flow vector (Q_n) defined in Eq. (5.2). We start with the calculations of single-event average two- and four-particle correlation function using the following expressions.

$$\begin{aligned} \langle 2 \rangle &= \frac{|Q_n|^2 - M}{M(M-1)}, \\ \langle 4 \rangle &= \frac{|Q_n|^4 + |Q_{2n}|^2 - 2 \cdot \mathrm{Re}[Q_{2n} Q_n^* Q_n^*]}{M(M-1)(M-2)(M-3)} \\ &\quad - 2\frac{2(M-2) \cdot |Q_n|^2 - M(M-3)}{M(M-1)(M-2)(M-3)} \end{aligned} \tag{5.13}$$

The event-average correlation function can be calculated using the following equation.

$$\begin{aligned} \langle\langle 2 \rangle\rangle &= \frac{\sum_{i=1}^{N_{\mathrm{ev}}} (W_{\langle 2 \rangle})_i \langle 2 \rangle_i}{\sum_{i=1}^{N_{\mathrm{ev}}} (W_{\langle 2 \rangle})_i}, \\ \langle\langle 4 \rangle\rangle &= \frac{\sum_{i=1}^{N_{\mathrm{ev}}} (W_{\langle 4 \rangle})_i \langle 4 \rangle_i}{\sum_{i=1}^{N_{\mathrm{ev}}} (W_{\langle 4 \rangle})_i}. \end{aligned} \tag{5.14}$$

Here, $\langle\langle \dots \rangle\rangle$ stands for the average over all the charged hadrons of all the events. The superscript, '*', stands for the complex conjugate, and $N_{\rm ev}$ is the total number of events. $(W_{\langle 2\rangle})_i$ and $(W_{\langle 4\rangle})_i$ are the weight factors for the $i^{\rm th}$ event, which considers the number of individual two- and four-particle combinations in the event of multiplicity M. $W_{\langle 2\rangle}$ and $W_{\langle 4\rangle}$ are calculated using the following equations.

$$\begin{aligned} W_{\langle 2\rangle} &= M(M-1), \\ W_{\langle 4\rangle} &= M(M-1)(M-2)(M-3). \end{aligned} \tag{5.15}$$

The two- and four-particle cumulants are calculated as:

$$\begin{aligned} c_n\{2\} &= \langle\langle 2\rangle\rangle, \\ c_n\{4\} &= \langle\langle 4\rangle\rangle - 2\cdot\langle\langle 2\rangle\rangle^2, \end{aligned} \tag{5.16}$$

Consequently, the reference flow of the charged particles can be estimated using the following expression.

$$\begin{aligned} v_n\{2\} &= \sqrt{c_n\{2\}}, \\ v_n\{4\} &= \sqrt[4]{-c_n\{4\}}. \end{aligned} \tag{5.17}$$

To estimate the $p_{\rm T}$ or η-differential flow of the particles of interest (POIs), the p_n and t_n vectors for specific kinematic range and/or for specific hadron species are defined as follows:

$$\begin{aligned} p_n &= \sum_{j=1}^{m_p} e^{in\phi_j}, \\ t_n &= \sum_{j=1}^{m_q} e^{in\phi_j}, \end{aligned} \tag{5.18}$$

Where m_p is the multiplicity of the particles which are labelled as POIs, and m_t is the total number of particles considered as both reference flow particles (RFPs) and POIs. To quantify the collective motion of the system and establish the orientation of the event plane, RFPs serve as a reference frame for POIs. The single-event average differential two- and four-particle correlation functions are given as follows.

$$\begin{aligned} \langle 2^{'}\rangle &= \frac{p_n Q_n^* - m_t}{m_p M - m_t}, \\ \langle 4^{'}\rangle &= [p_n Q_n Q_n^* Q_n^* - t_{2n} Q_n^* Q_n^* - p_n Q_n Q_{2n}^* \\ &\quad - 2\cdot M p_n Q_n^* - 2\cdot m_q |Q_n|^2 + 7\cdot q_n Q_n^* - Q_n t_n^* \\ &\quad + t_{2n} Q_{2n}^* + 2\cdot p_n Q_n^* + 2\cdot m_t M - 6\cdot m_t] \\ &\quad / \left[(m_p M - 3m_t(M-1)(M-2)\right] \end{aligned} \tag{5.19}$$

Similarly, the event-average two- and four-particle differential correlations are estimated as follows.

$$\begin{aligned}\langle\langle 2^{'}\rangle\rangle &= \frac{\sum_{i=1}^{N_{\rm ev}}(w_{\langle 2'\rangle})_i\langle 2^{'}\rangle_i}{\sum_{i=1}^{N_{\rm ev}}(w_{\langle 2'\rangle})_i},\\ \langle\langle 4^{'}\rangle\rangle &= \frac{\sum_{i=1}^{N_{\rm ev}}(w_{\langle 4'\rangle})_i\langle 4^{'}\rangle_i}{\sum_{i=1}^{N_{\rm ev}}(w_{\langle 4'\rangle})_i}.\end{aligned} \tag{5.20}$$

Here, $w_{\langle 2'\rangle}$ and $w_{\langle 4'\rangle}$ are the weights for two- and four-particle cumulants, respectively, and are calculated as follows.

$$\begin{aligned}w_{\langle 2'\rangle} &= m_p M - m_t,\\ w_{\langle 4'\rangle} &= (m_p M - 3m_t)(M-1)(M-2)\end{aligned} \tag{5.21}$$

Consequently, the two- and four-particle differential cumulants are calculated using the following expressions.

$$\begin{aligned}d_n\{2\} &= \langle\langle 2^{'}\rangle\rangle,\\ d_n\{4\} &= \langle\langle 4^{'}\rangle\rangle - 2\langle\langle 2^{'}\rangle\rangle\langle\langle 2\rangle\rangle.\end{aligned} \tag{5.22}$$

Finally, the $p_{\rm T}$-differential flow $v_n(p_{\rm T})$ using two- and four-particle cumulants are given as:

$$\begin{aligned}v_n\{2\}(p_{\rm T}) &= \frac{d_n\{2\}}{\sqrt{c_n\{2\}}},\\ v_n\{4\}(p_{\rm T}) &= -\frac{d_n\{4\}}{\sqrt[4]{(-c_n\{4\})^3}}.\end{aligned} \tag{5.23}$$

The v_n calculated from the two-particle Q-Cumulant method, as shown in Eq. (5.23), contains contributions from non-flow. To get rid of this, a pseudorapidity gap between the particles in the two-particle Q-cumulant method can be introduced [130–134]. Accordingly, the whole event can be divided into two sub-events [135–137], namely, A and B, separated by a $|\Delta\eta|$ gap. This modifies Eq. (5.13) as follows:

$$\langle 2\rangle_{\Delta\eta} = \frac{Q_n^A \cdot Q_n^{B*}}{M_A \cdot M_B}. \tag{5.24}$$

Here, Q_n^A and Q_n^B are the flow vectors of the sub-event A and B, respectively. M_A and M_B are the corresponding particle multiplicities. The two-particle Q-cumulant with a $|\Delta\eta|$ gap is calculated as follows.

$$c_n\{2, |\Delta\eta|\} = \langle\langle 2\rangle\rangle_{\Delta\eta}. \tag{5.25}$$

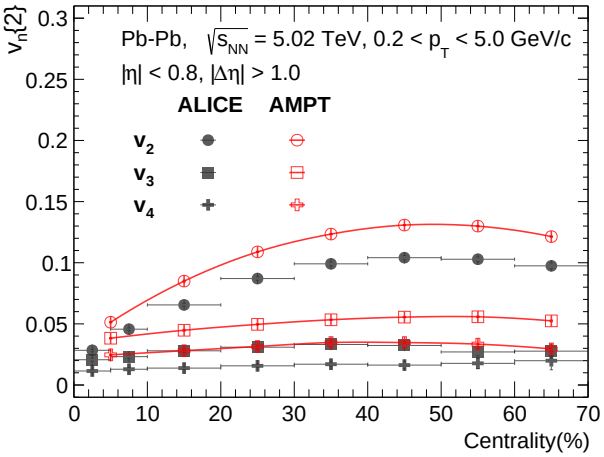

Figure 5.2: $v_n\{2\}$ vs centrality in Pb–Pb collisions at $\sqrt{s_{\rm NN}}$ = 5.02 TeV using AMPT compared with ALICE measurements [24, 108].

There will be no overlap between POIs and RFPs if we select RFPs from one subevent and POIs from the other. Thus Eq. (5.19) is modified as follows,

$$\langle 2^{'} \rangle_{\Delta\eta} = \frac{p_{n,A} Q^{*}_{n,B}}{m_{p,A} M_B}, \tag{5.26}$$

and consequently, the differential two-particle cumulant is:

$$d_n\{2, |\Delta\eta|\} = \langle\langle 2^{'} \rangle\rangle_{\Delta\eta}. \tag{5.27}$$

The $p_{\rm T}$-differential flow from the two-particle cumulant method is calculated by inserting the two-particle reference flow with the η gap into the differential two-particle cumulant, which is shown as follows.

$$v_n\{2, |\Delta\eta|\}(p_{\rm T}) = \frac{d_n\{2, |\Delta\eta|\}}{\sqrt{c_n\{2, |\Delta\eta|\}}}. \tag{5.28}$$

Assuming, small and Gaussian-like anisotropic flow fluctuations (σ_{v_n}), the mean ($\langle v_n \rangle$) and σ_{v_n} can be represented in terms of $v_n\{2, |\Delta\eta|\}$ and $v_n\{4\}$, as follows [138, 139].

$$\langle v_n \rangle = \sqrt{\frac{v_n^2\{2, |\Delta\eta|\} + v_n^2\{4\}}{2}} \tag{5.29}$$

$$\sigma_{v_n} = \sqrt{\frac{v_n^2\{2, |\Delta\eta|\} - v_n^2\{4\}}{2}} \tag{5.30}$$

Using Eqs. (5.29), and (5.30), the relative anisotropic flow fluctuation ($F(v_n)$) is estimated as follows.

$$F(v_n) = \frac{\sigma_{v_n}}{\langle v_n \rangle} \tag{5.31}$$

The charged hadrons within the pseudorapidity region, $|\eta| < 2.5$ are used for the two- and four-particle Q-cumulants method. The charged hadrons within $|\eta| < 2.5$ and $0.2 < p_{\mathrm{T}} < 4.0$ GeV/c constitute the RFPs. A pseudorapidity gap, $|\Delta\eta| > 1.0$ in the two-subevent method, is applied to reduce the non-flow contributions from the two-particle Q-cumulant method.

Figure 5.2 compares the $v_n\{2\}$ as a function of centrality measured from AMPT with that of ALICE in a similar kinematic region using the two-particle cumulant method. One finds that AMPT provides an overestimation of anisotropic flow coefficients; however, it retains overall a good qualitative description of the flow coefficients.

5.3.2 Eccentricity and triangularity

The collision overlap region in a non-central heavy-ion collision is almond-shaped, which leads to the formation of a large pressure gradient, and the initial geometry during the collisions is reflected in the final state momentum space azimuthal anisotropy. The anisotropy in the spatial distribution of the participating nucleons can be quantified by the eccentricity (ϵ_2), triangularity (ϵ_3), etc. The eccentricity quantifies how elliptical the medium is and is dominantly generated because of nuclear overlap. Similarly, trangularity describes the triangular geometry of the nuclear overlap region during the collision and primarily arises due to event-by-event fluctuations in the participant nucleon positions [140]. In this thesis, AMPT model is used study ϵ_2 and ϵ_3 having followed the notations used in [21]. ϵ_{n} of the collision overlap region can be calculated as follows [21]:

$$\epsilon_n = \frac{\sqrt{\langle r^n cos(n\phi_{\mathrm{part}})\rangle^2 + \langle r^n \sin(n\phi_{\mathrm{part}})\rangle^2}}{\langle r^n \rangle}. \tag{5.32}$$

Here, r and ϕ_{part} are the polar position co-ordinates of the participant nucleons. The angular brackets, "$\langle ... \rangle$" represent the average taken over all the participant nucleons in an event. Likewise, the average of ϵ_n over all the events is denoted as $\langle \epsilon_n \rangle$. Similar to anisotropic flow fluctuations, one can quantify the eccentricity fluctuations (σ_{ϵ_2}), as follows.

$$\sigma_{\epsilon_2} = \sqrt{\langle \epsilon_2^2 \rangle - \langle \epsilon_2 \rangle^2} \tag{5.33}$$

Consequently, one can obtain relative eccentricity fluctuations as [141, 142]:

$$F(\epsilon_2) = \frac{\sigma_{\epsilon_2}}{\langle \epsilon_2 \rangle} \tag{5.34}$$

5.4 Results

In Chapter 2, we extensively discussed transverse spherocity in pp collisions with other event classifiers. In this chapter, we shall use transverse spherocity in Pb-Pb collisions to study some of its properties. We start with a distribution of transverse spherocity in Pb–Pb collisions at $\sqrt{s_{\rm NN}} = 5.02$ TeV for different centrality classes using AMPT compared with that of obtained in pp collisions at $\sqrt{s} = 13$ TeV for different multiplicity classes using PYTHIA8, as shown in the upper and lower panels of Fig. 5.3, respectively. With an increase in multiplicity/centrality of collision, the S_0 distribution shifts towards the isotropic limit, i.e., $S_0 \to 1$. However, in Pb–Pb collisions, the distribution of S_0 is mostly towards the isotropic limit, irrespective of the centrality classes. This hints that S_0 is influenced by the final state multiplicity of the event. Moreover, the extreme 20% events in the S_0 distribution can no longer be referred to as jet or isotropic topology due to the large multiplicity in heavy-ion collisions. Thus, throughout this chapter, we shall use low-S_0 and high-S_0 notation for the events having the smallest and largest 20% value in the S_0 distribution. Table 5.1 shows the S_0 cuts for high-S_0 and low-S_0 events for different centrality classes in Pb–Pb collisions at $\sqrt{s_{\rm NN}} = 5.02$ TeV using AMPT.

5.4.1 S_0 versus q_2

Moving ahead, the correlation between $\langle q_n \rangle$ and S_0 for different centrality classes in Pb–Pb collisions at $\sqrt{s_{\rm NN}} = 5.02$ TeV using AMPT is shown in Fig. 5.4. Here, clearly S_0 possesses an anticorrelation with q_2 and a positive correlation with q_3. It is important to note that S_0 possesses a stronger anticorrelation with q_2 than the positive correlation with q_3, which is weak. Moreover, the strength of this (anti-)correlation of S_0 with q_n depends upon collision centrality, which is stronger for (40-50)% centrality than (60-70)% centrality. This is attributed to the statistical smearing of q_n due to the lowering of multiplicity towards the peripheral collisions.

Table 5.1: Low-S_0 and high-S_0 event selection cuts on spherocity distribution for different centrality classes in Pb–Pb collisions at $\sqrt{s_{\rm NN}} = 5.02$ TeV [22, 105].

Centrality (%)	Low-S_0	High-S_0
0-10	0 – 0.880	0.953 – 1
10-20	0 – 0.813	0.914 – 1
20-30	0 – 0.760	0.882 – 1
30-40	0 – 0.735	0.869 – 1
40-50	0 – 0.716	0.865 – 1
50-60	0 – 0.710	0.870 – 1
60-70	0 – 0.707	0.873 – 1

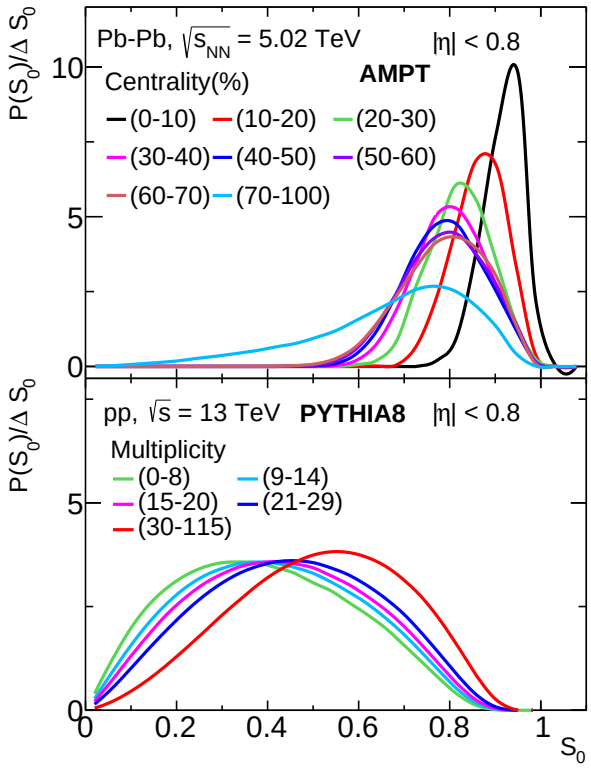

Figure 5.3: Transverse spherocity (S_0) distribution in Pb-Pb (upper) and pp (lower) collisions for different centrality and multiplicity classes, respectively [105].

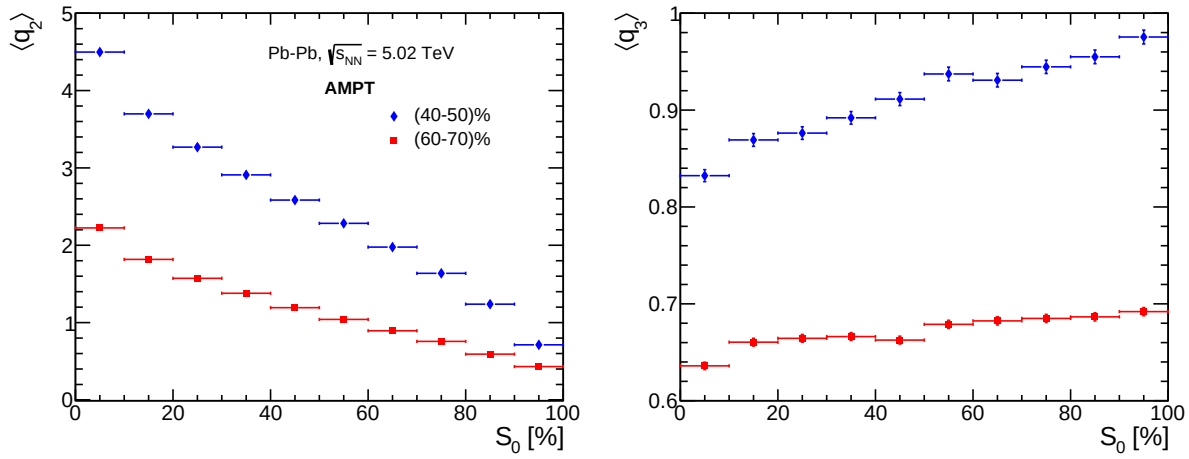

Figure 5.4: $\langle q_2 \rangle$ (left) and $\langle q_3 \rangle$ (right) as a function of S_0 percentiles in Pb–Pb collisions at $\sqrt{s_{NN}} = 5.02$ TeV using AMPT model [22].

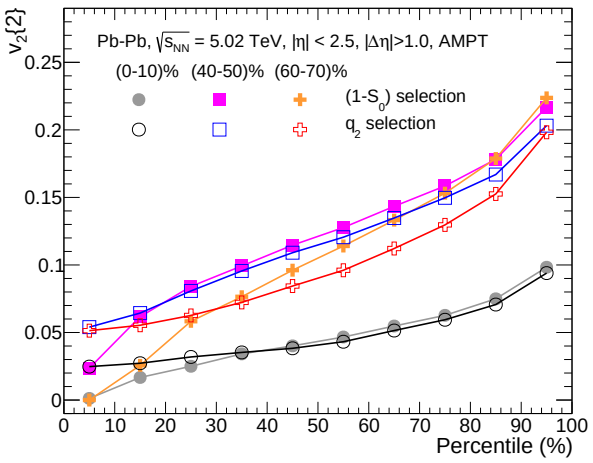

Figure 5.5: v_2 versus q_2 and $(1 - S_0)$ percentiles for different centrality classes in Pb–Pb collisions at $\sqrt{s_{NN}} = 5.02$ TeV using AMPT [108].

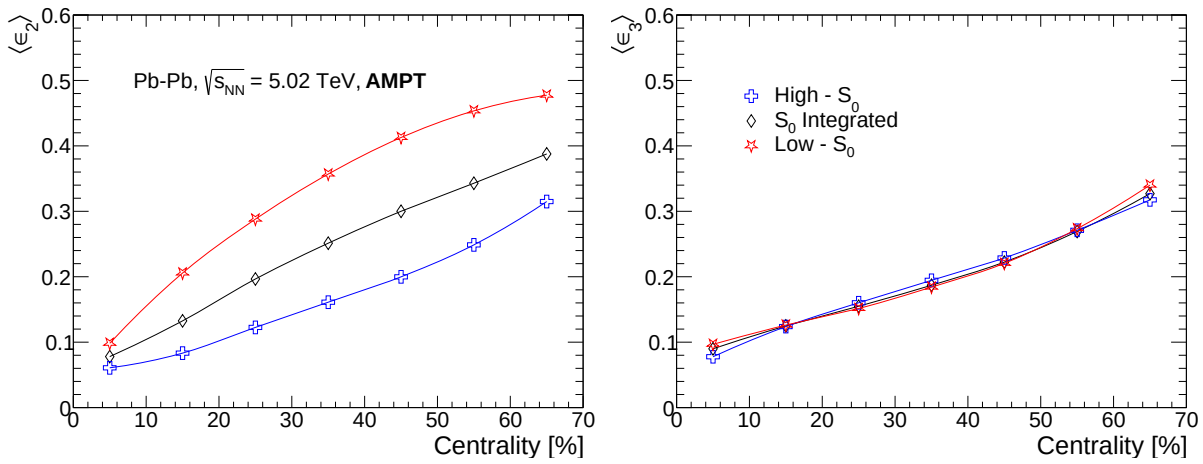

Figure 5.6: $\langle\varepsilon_2\rangle$ (left) and $\langle\varepsilon_3\rangle$ (right) as a function of centrality for S_0 classes in Pb–Pb collisions at $\sqrt{s_{\rm NN}} = 5.02$ TeV using AMPT [22, 143].

To test the event selection using S_0 against that of q_2 for the study of anisotropic flow coefficients, Fig. 5.5 shows $v_2\{2\}$ as a function of percentiles of q_2 and $(1 - S_0)$ in Pb–Pb collisions at $\sqrt{s_{\rm NN}} = 5.02$ TeV using AMPT. Here, we have kept $(1 - S_0)$ percentiles instead of S_0, to keep the measurement of v_2 consistent with that of q_2. It is interesting to note that, throughout the centrality classes, S_0 probes broader v_2 values in comparison to those of q_2. Moreover, the event selection with q_2 gets worse from central to peripheral collisions, where the difference between the maximum and minimum values of $v_2\{2\}$ for extreme q_2 values reduces from a factor of 3.8 in most central to 3.6 in mid-central and peripheral collisions. On the other hand, with S_0, the event selection is better than that of q_2.

5.4.2 S_0 dependence of ϵ_n

Now that, the event selection capability of S_0 against that of q_2 has been discussed, the section moves towards discussing the initial eccentricity and triangularity as a function of centrality for different S_0 events. Fig. 5.6 shows $\langle\epsilon_2\rangle$ (left) and $\langle\epsilon_3\rangle$ (right) as a function of centrality for different classes of S_0 in Pb–Pb collisions at $\sqrt{s_{\rm NN}} = 5.02$ TeV using AMPT. One can observe a clear dependence of S_0 and centrality on both $\langle\epsilon_2\rangle$ and $\langle\epsilon_3\rangle$, which increases from central to peripheral collisions. This is because, in central collisions, the nuclear overlap region is more spatially isotropic compared to that in peripheral collisions. This results in smaller values of $\langle\epsilon_n\rangle$ in most central collisions. However, as

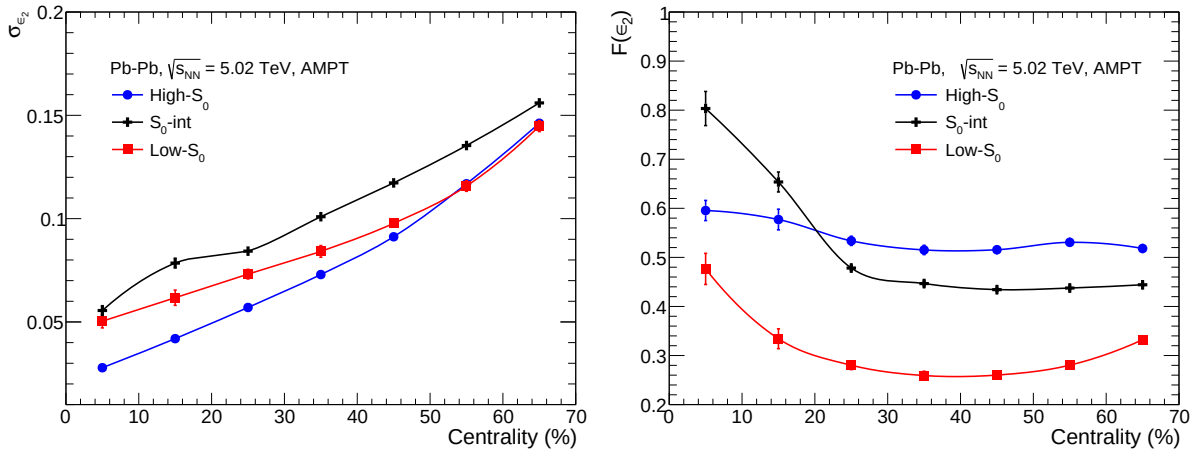

Figure 5.7: Centrality dependence of σ_{ϵ_2} (left) and $F(\epsilon_2)$ (right) for different S_0 classes in Pb–Pb collisions at $\sqrt{s_{\rm NN}} = 5.02$ TeV using AMPT [108].

one moves towards the peripheral collisions, the collision overlap region gets spatially anisotropic, which results in higher values of $\langle\epsilon_n\rangle$. For a specific centrality class, one finds a lower $\langle\epsilon_2\rangle$ for high-S_0 events than that of low-S_0 case. This hints that S_0 is a good event shape observable which is capable of distinguishing events based on the initial geometry. Moreover, since the effects from density fluctuations dominate ϵ_n for $n > 2$, no significant S_0 dependence is observed.

Interestingly, one observes a finite spherocity dependence on eccentricity fluctuation (σ_{ϵ_2}), as shown in the left panel of Fig. 5.7, where the centrality and S_0 dependence of σ_{ϵ_2} in Pb-Pb collisions at $\sqrt{s_{\rm NN}} = 5.02$ TeV using AMPT is presented. When one moves from central to peripheral collisions, corresponding σ_{ϵ_2} increases due to a decrease in the number of participating nucleons ($N_{\rm part}$), as shown in Fig 5.8, which contributes to event-by-event ϵ_2. Moreover, throughout the centrality classes, S_0-integrated events possess the largest values of σ_{ϵ_2}. This is because, σ_{ϵ_2} is related to the width of the ϵ_2, distribution which is broader when no S_0 selection is applied in comparison to when S_0 selection is applied to bias the ϵ_2 distribution towards a particular value, thus lowering the σ_{ϵ_2}. Furthermore, the low-S_0 events have larger σ_{ϵ_2} than that of high-S_0 events in (0-50)% centrality region. This is attributed to a lower $\langle N_{\rm part}\rangle$ for low-S_0 events, shown in Fig. 5.8, which leads to large fluctuations for the low-S_0 case.

The study is further extended to include the S_0-dependence of relative eccentricity fluctuations ($F(\epsilon_2)$), which is shown in the right panel of Fig. 5.7. It shows the S_0 and

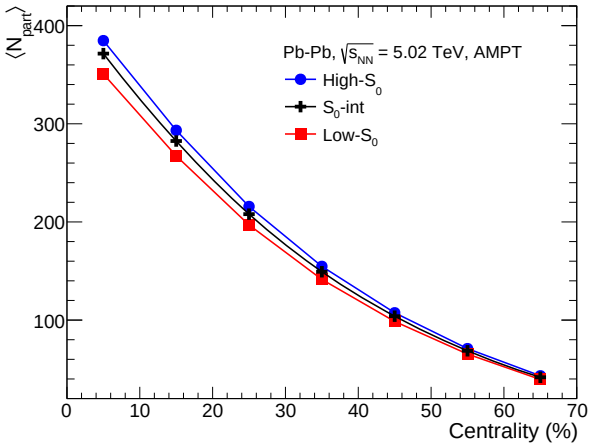

Figure 5.8: Centrality dependence of $\langle N_{\rm part} \rangle$ for different S_0 classes in Pb–Pb collisions at $\sqrt{s_{\rm NN}} = 5.02$ TeV using AMPT [108].

centrality dependence of $F(\epsilon_2)$ in Pb–Pb collisions at $\sqrt{s_{\rm NN}} = 5.02$ TeV using AMPT. Irrespective of S_0 class, $F(\epsilon_2)$ decreases as one moves from central to mid-central collisions. Thereafter, $F(\epsilon_2)$ remains nearly unchanged for S_0-integrated and high-S_0 events till peripheral collisions. In contrast, in the low-S_0 events, a rise of $F(\epsilon_2)$ begins towards the peripheral collisions. Within (0-20)% centrality class, S_0-integrated events are shown to possess the highest $F(\epsilon_2)$, while the low-S_0 class has the smallest $F(\epsilon_2)$ throughout the collision centrality. However, $F(\epsilon_2)$ for the S_0-int events lies between the high and low-S_0 events in the (20-70)% centrality. This is because, in central collisions, the value of ϵ_2 is driven dominantly by event-by-event density fluctuations. Thus, a higher value of σ_{ϵ_2} and lower $\langle \epsilon_2 \rangle$ for the S_0-int case in central collisions lead to a large $F(\epsilon_2)$. In comparison, large $\langle \epsilon_2 \rangle$ for the low-S_0 events makes $F(\epsilon_2)$ small. However, as one approaches the mid-central collisions, the difference in σ_{ϵ_2} for different S_0 classes is negligibly smaller than that of $\langle \epsilon_2 \rangle$, which drives the measured $F(\epsilon_2)$. High-S_0 and low-S_0 events have significant and distinct values of $F(\epsilon_2)$ across the centrality, which affirms that the S_0 can be useful to study initial state geometry and fluctuations.

5.4.3 S_0 dependence of v_2 and $F(v_2)$

Figure 5.9 shows two-particle azimuthal correlation function for different centrality and S_0 classes in Pb–Pb collisions at $\sqrt{s_{\rm NN}} = 5.02$ TeV using AMPT [22]. At a first glance, it is clear that the azimuthal correlations are stronger for (40-50)% centrality, shown in the

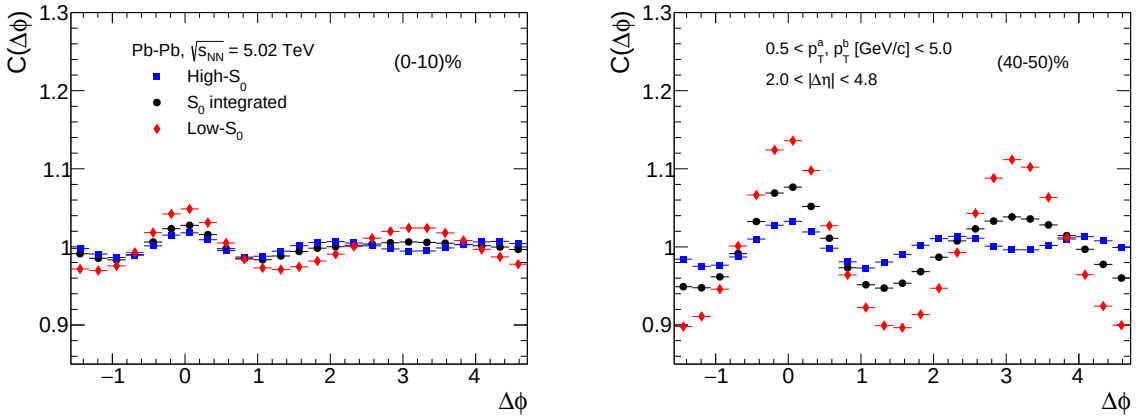

Figure 5.9: One dimensional two-particle correlation function for different S_0 and centrality classes in Pb–Pb collisions at $\sqrt{s_{\rm NN}} = 5.02$ TeV using AMPT [22].

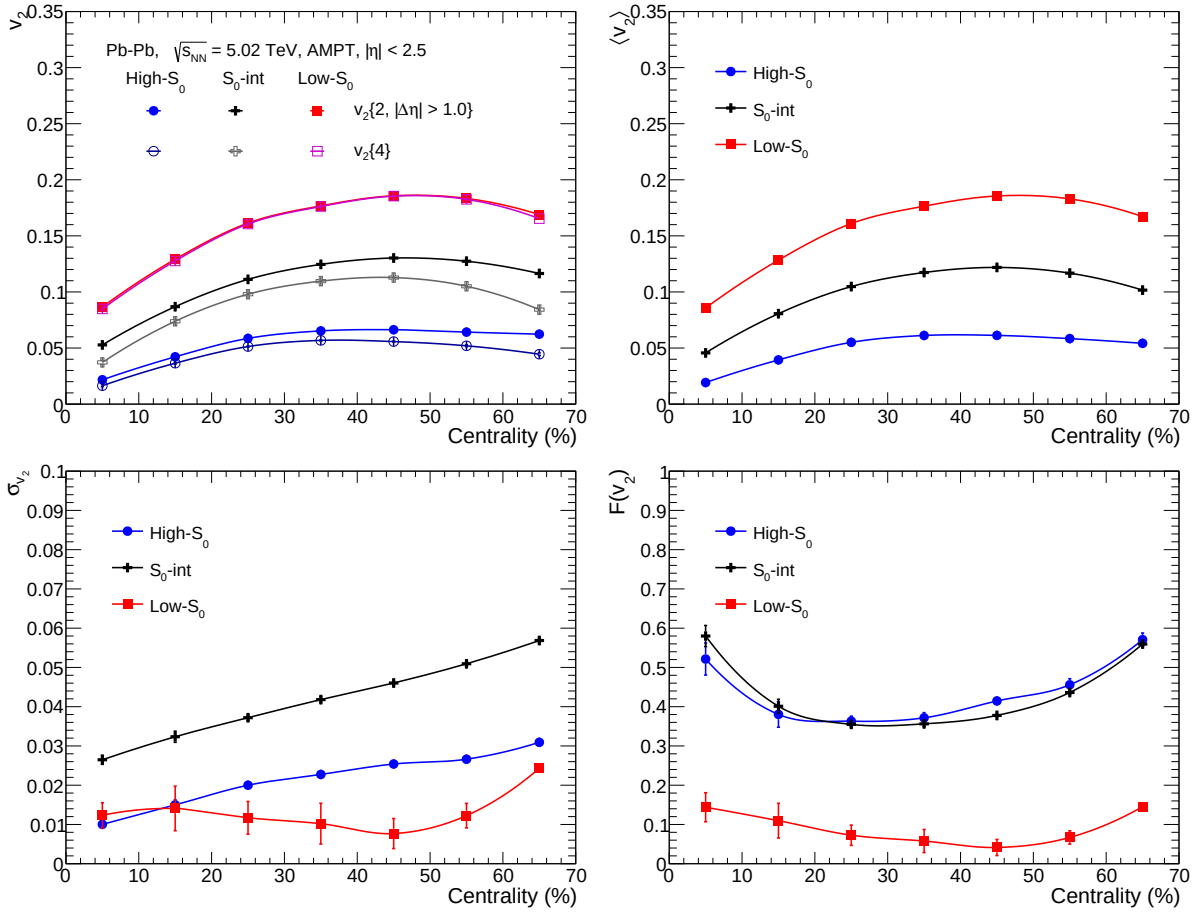

Figure 5.10: Centrality dependence of v_2 (upper left), $\langle v_2 \rangle$ (upper right), σ_{v_2} (lower left), and $F(v_2)$ (lower right), estimated using multi-particle Q-cumulant method, for different classes of S_0 in Pb–Pb collisions at $\sqrt{s_{\rm NN}} = 5.02$ TeV using AMPT [108].

right panel of Fig 5.9 than that of (0-10)% centrality, shown in the left panel, irrespective of the spherocity selection. Moreover, low-S_0 events show a stronger two-peak structure around $\phi \sim 0$ and $\phi \sim \pi$ than that of S_0-integrated events, which implies the dominance of elliptic flow in low-S_0 events. In contrast, high-S_0 events show a three-peak structure, which becomes prominent for (40-50)% central class than (0-10)% centrality, indicating significant contributions from triangular flow.

Figure 5.10 shows centrality and S_0 dependence of v_2 (upper left), $\langle v_2 \rangle$ (upper right), σ_{v_2} (lower left), and $F(v_2)$ (lower right), estimated using multi-particle Q-cumulant method, in Pb–Pb collisions at $\sqrt{s_{\rm NN}} = 5.02$ TeV using AMPT [108]. In the upper left panel of Fig. 5.10, one finds a large difference in the measured values of $v_2\{2\}$ and $v_2\{4\}$ for the S_0-integrated case, which naively indicates large elliptic flow fluctuations for the S_0-integrated case attributed to the wide distributions of elliptic flow in the absence of event-shape selection [144]. However, the difference in the measured value of v_2 from two and four particle cumulants decreases when an S_0 selection is applied. The difference is smaller for high-S_0 events than that of S_0-integrated events, and is negligibly small for the low-S_0 events. Moreover, this difference between $v_2\{2\}$ and $v_2\{4\}$ gradually increases irrespective of S_0 class from (0-10)% centrality to (60-70)% centrality. The upper right panel of Fig. 5.10 shows the $\langle v_2 \rangle$, estimated using Eq. (5.29), for different centrality and S_0 classes in Pb–Pb collisions using AMPT. The centrality and spherocity dependence of $\langle v_2 \rangle$ is similar to that of $v_2\{4\}$, as shown in the upper left panel of Fig. 5.10.

The lower left panel of Fig. 5.10 shows σ_{v_2} as a function of centrality for different S_0 classes in Pb–Pb collisions at $\sqrt{s_{\rm NN}} = 5.02$ TeV using AMPT. σ_{v_2} rises from central to peripheral collisions, which is attributed to a decrease in multiplicity towards the peripheral collisions [145]. σ_{v_2} follows a similar centrality dependence in high-S_0 and S_0-integrated cases. Moreover, σ_{v_2} is the largest for the S_0-integrated events, followed by high-S_0 and smallest for the low-S_0 events. Since the high-S_0 events have dominating circular geometry in the transverse momentum plane, the measured v_2 has large event-by-event fluctuations. In contrast, the low-S_0 events have smaller v_2 fluctuations due to the dominance of large elliptic geometry. Interestingly, S_0 can simultaneously choose events with large v_2 small σ_{v_2}.

In the lower right panel of Fig. 5.10, $F(v_2)$ as a function of centrality and S_0 is shown for

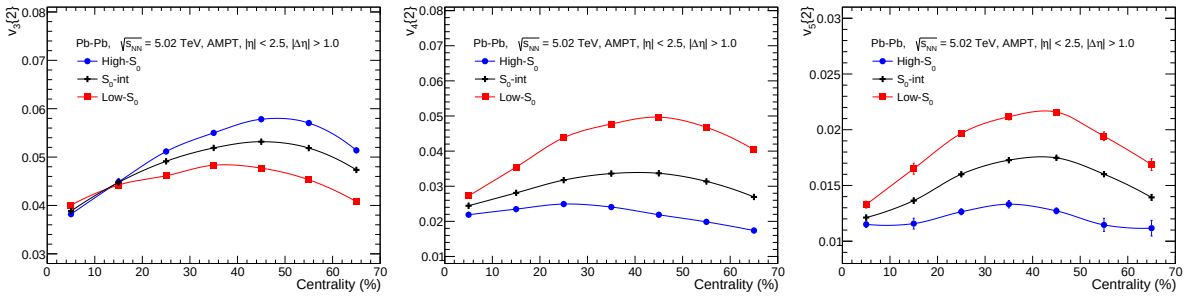

Figure 5.11: Centrality dependence of $v_3\{2\}$ (left), $v_4\{2\}$ (middle) and $v_5\{2\}$ (right) for different S_0 classes in Pb–Pb collisions at $\sqrt{s_{\rm NN}} = 5.02$ TeV using AMPT [108].

Pb–Pb collisions at $\sqrt{s_{\rm NN}} = 5.02$ TeV using AMPT. Here, $F(v_2)$ shows a minimum near the mid-central collisions and possesses large values towards the central and peripheral collisions. This behaviour of $F(v_2)$ is in agreement with experimental measurements shown in Refs. [145–147]. The observed large $F(v_2)$ in the central collisions signifies that v_2 has dominating contributions from flow fluctuations, which results from large initial eccentricity fluctuations, shown in Fig. 5.7. Moreover, a small final state charged particle multiplicity can lead to large fluctuations in the peripheral collisions. In comparison, the mid-central collisions have an elliptic collision overlap region and possess large particle multiplicity, which results in a smaller $F(v_2)$ in the mid-central collisions. One observes a significant dependence of $F(v_2)$ on S_0-based event selection. The low-S_0 events, which have a higher v_2 leads to smallest $F(v_2)$. Additionally, $F(v_2)$ for the S_0-integrated and high-S_0 cases are close. Here, the high-S_0 events possess a larger $F(v_2)$ in the off-central collisions. These features of the S_0 dependence of $F(v_2)$ are found to have propagated significantly from the initial collision geometry and fluctuations.

5.4.4 S_0 dependence of v_3, v_4 and v_5

Figure 5.11 shows the centrality and spherocity dependence of $v_3\{2\}$ (left), $v_4\{2\}$ (middle) and $v_5\{2\}$ (right) in Pb–Pb collisions at $\sqrt{s_{\rm NN}} = 5.02$ TeV using AMPT [108]. v_n increases from central to mid-central collisions to attain a maximum, and then starts to decrease towards the peripheral collisions. The smaller values of v_n in the central and peripheral collisions are attributed to the isotropic collision overlap region and a smaller number of particle yields, respectively. Additionally, from Fig. 5.10 and Fig. 5.11, it is clear

that $v_2 > v_3 > v_4 > v_5$ ordering is well respected for the S_0-integrated events. This implies that v_2 has the largest contribution to momentum space azimuthal anisotropy, where contributions from v_n decrease with increasing n. Moreover, v_n, except for $n = 3$, are larger for the low-S_0 events and smaller for high-S_0 events. In contrast, v_3 is found to be higher for the high-S_0 events and smaller for the low-S_0 events. This opposite trend of v_3, compared to other v_n, as a function of S_0 is attributed to anticorrelation between v_2 and v_3 [100]. Moreover, since, $v_4\{2\}$ has non-linear contributions from v_2. Therefore, the anti-correlation between $v_2\{2\}$ and S_0 is reflected in S_0 dependence of $v_4\{2\}$. Similarly, $v_5\{2\}$ possesses contributions from both $v_2\{2\}$ and $v_3\{2\}$, which is shown in Eq. (5.4). Since, throughout the centrality, $v_2 > v_3$, one would expect v_5 to have a larger contribution from v_2 than v_3. Since the anti-correlation between $v_2\{2\}$ and S_0 stronger that of positive correlation between $v_3\{2\}$ and S_0, $v_5\{2\}$ shows anti-correlation behavior with event selection based on S_0.

5.4.5 S_0 dependence of $v_n/\sqrt{\langle\epsilon_n^2\rangle}$

The study of the ratio v_n/ϵ_n is one of the ways to characterise the medium response to the evolution of v_n from ϵ_n. Figure 5.12 shows the centrality and spherocity dependence of $v_n\{2\}/\sqrt{\langle\epsilon_n^2\rangle}$ in Pb–Pb collisions at $\sqrt{s_{\rm NN}} = 5.02$ TeV using AMPT. The upper left panel shows a significant S_0 and centrality dependence on $v_2\{2\}/\sqrt{\langle\epsilon_2^2\rangle}$, which decreases with a decrease in collision centrality. This decrease is attributed to the reduced number of participants towards the peripheral collisions, which impacts the evolution of ϵ_2 to v_2 strongly. $v_2\{2\}/\sqrt{\langle\epsilon_2^2\rangle}$ is observed to be higher for the low-S_0 events than the high-S_0 events, while it is expected to be higher for high-S_0 events because of larger multiplicity as compared to low-S_0 events [105]. The observed S_0 dependence of $v_2\{2\}/\sqrt{\langle\epsilon_2^2\rangle}$ can be attributed to the following possible scenario. Firstly, the large number of soft partonic interactions in the high-S_0 events drives the system towards isotropisation, which is expected to affect the transformation from ϵ_2 to v_2. Additionally, the system's response to the elliptic flow originating from geometrical anisotropy varies from that of the elliptic flow arising due to initial density fluctuations. This is anticipated since a smaller $v_2\{2\}/\sqrt{\langle\epsilon_2^2\rangle}$ is observed for the events where the event-by-event fluctuations dominate the measured value of v_2. Moreover, a decrease of $v_2\{2\}/\sqrt{\langle\epsilon_2^2\rangle}$ in the most central collisions of high-S_0 events is

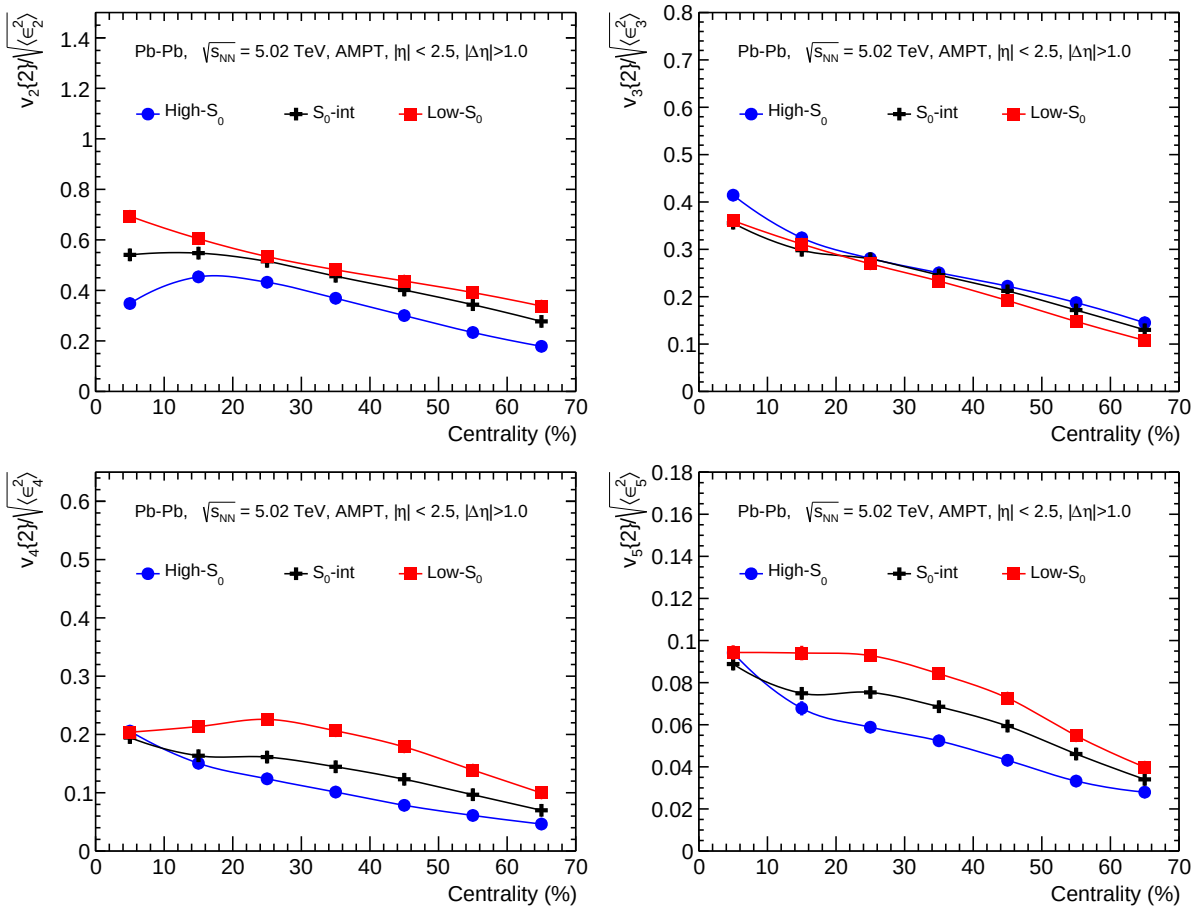

Figure 5.12: Centrality and S_0 dependence of $v_n\{2\}/\sqrt{\langle\epsilon_n^2\rangle}$, with n=2, 3, 4, and 5, in Pb-Pb collisions at $\sqrt{s_{NN}} = 5.02$ TeV using AMPT [108].

observed. From this observation, it can be inferred that the events having large $F(v_2)$ are sensitive to the system response to the evolution from ϵ_2 to v_2 than the events having smaller $F(v_2)$. In the upper right panel of Fig. 5.12, centrality dependence of $v_3\{2\}/\sqrt{\langle\epsilon_3^2\rangle}$ is shown for different S_0 classes in Pb–Pb collisions at $\sqrt{s_{\rm NN}} = 5.02$ TeV using AMPT. $v_3\{2\}/\sqrt{\langle\epsilon_3^2\rangle}$ shows a similar centrality dependence as $v_2\{2\}/\sqrt{\langle\epsilon_2^2\rangle}$, which decreases from central to peripheral collisions. Nevertheless, $v_3\{2\}/\sqrt{\langle\epsilon_3^2\rangle}$ varies weakly for different S_0 classes, which may arise due to anti-correlations between v_2 and v_3. The lower panels show the centrality and S_0 dependence of $v_4\{2\}/\sqrt{\langle\epsilon_4^2\rangle}$ (left) and $v_5\{2\}/\sqrt{\langle\epsilon_5^2\rangle}$ (right). Here, both $v_4\{2\}/\sqrt{\langle\epsilon_4^2\rangle}$ and $v_5\{2\}/\sqrt{\langle\epsilon_5^2\rangle}$ show similar centrality and S_0 dependence, which decreases with decrease in collision centrality and becomes smaller for high-S_0 events. The high-S_0 events having smaller contribution from v_2, both $v_4\{2\}/\sqrt{\langle\epsilon_4^2\rangle}$ and $v_5\{2\}/\sqrt{\langle\epsilon_5^2\rangle}$ show a monotonic decreasing behavior when going from central to peripheral collisions. Moreover, the high-S_0 events show stronger centrality dependence of $v_4\{2\}/\sqrt{\langle\epsilon_4^2\rangle}$ and $v_5\{2\}/\sqrt{\langle\epsilon_5^2\rangle}$, which is similar to stronger viscous-damping effects, shown in hydrodynamic models [148–150]. For low-S_0 case, $v_4\{2\}/\sqrt{\langle\epsilon_4^2\rangle}$ shows a small bump in (20-30)% centrality. This is expected because of the competing effects of damping (similar to high-S_0 events) and dominating effects from v_2. However, $v_5\{2\}/\sqrt{\langle\epsilon_5^2\rangle}$ shows a saturation behavior in (0-30)% centrality for the low-S_0 events, since the damping effects are stronger for $v_5\{2\}/\sqrt{\langle\epsilon_5^2\rangle}$ than that of $v_4\{2\}/\sqrt{\langle\epsilon_4^2\rangle}$, and $v_5\{2\}/\sqrt{\langle\epsilon_5^2\rangle}$ is possess a smaller contribution from v_2.

5.4.6 S_0 versus $p_{\rm T}$-differential v_n

Figure 5.13 shows $p_{\rm T}$-differential $v_2\{2\}$, $v_3\{2\}$, $v_4\{2\}$, and $v_5\{2\}$ (from top to bottom), estimated using two-particle Q-cumulant method, in (0-10)% (left) and (40-50)% (right) centrality classes for different classes of transverse spherocity in Pb–Pb collisions at $\sqrt{s_{\rm NN}} = 5.02$ TeV using AMPT. Here, v_n increases from low to intermediate $p_{\rm T}$ regions and decreases towards the high-$p_{\rm T}$ region, which is similar to experimental measurements shown in Ref. [24]. For S_0-int case, v_2 is higher for (40-50)% centrality than (0-10)% centrality. Further, except for v_2, the spherocity dependence is not visible for the (0-10)% centrality class. However, v_n shows a modest S_0 dependence for (40-50)% centrality. It is important to note that, for high-S_0 events, v_3 is higher than v_2, in the intermediate to

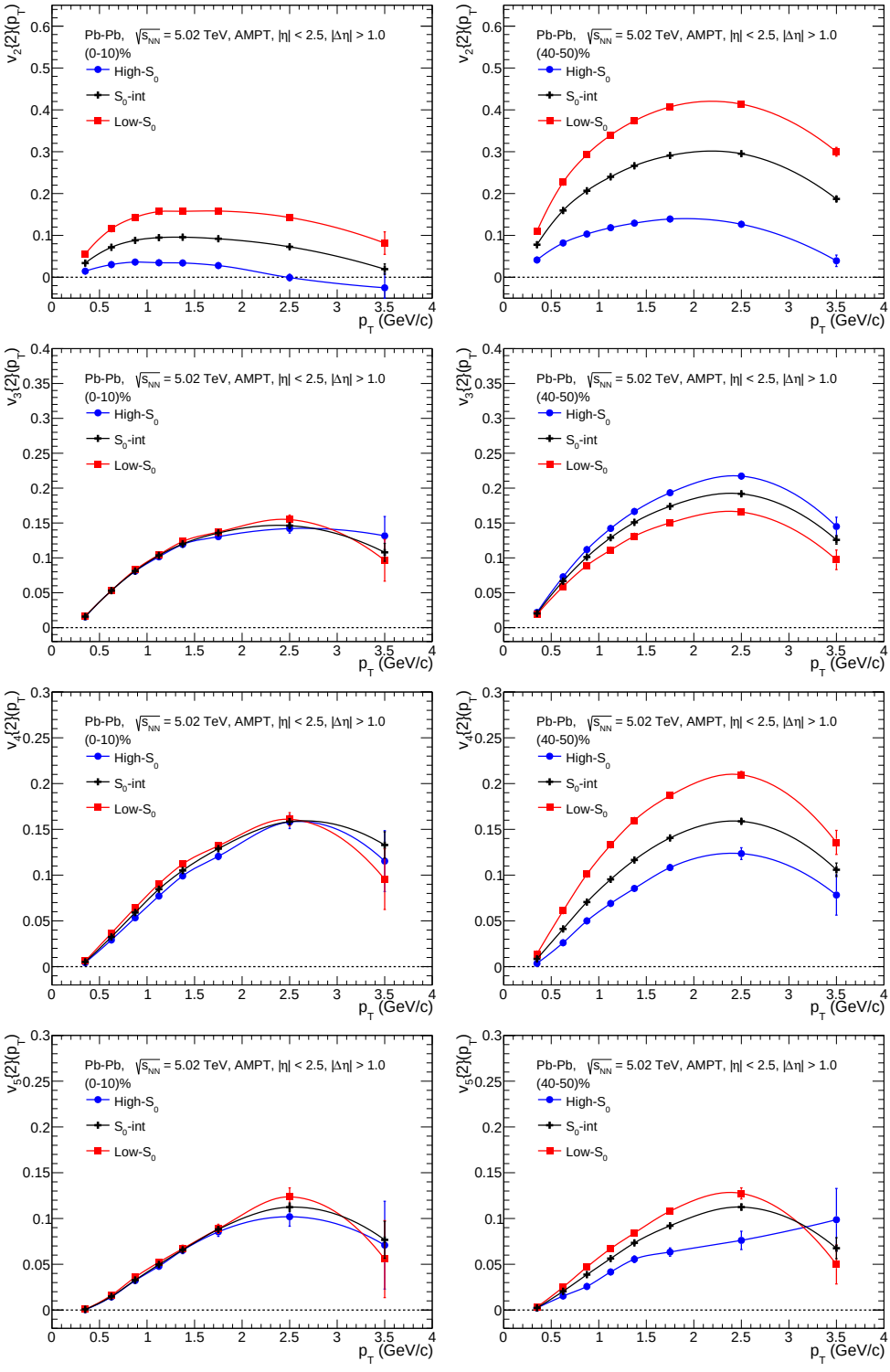

Figure 5.13: p_{T}-differential $v_2\{2\}$, $v_3\{2\}$, $v_4\{2\}$ and $v_5\{2\}$ in (0-10)% (left) and (40-50)% (right) centrality classes for high-S_0, S_0-integrated and low-S_0 events in Pb–Pb collisions at $\sqrt{s_{\mathrm{NN}}} = 5.02$ TeV using AMPT [108].

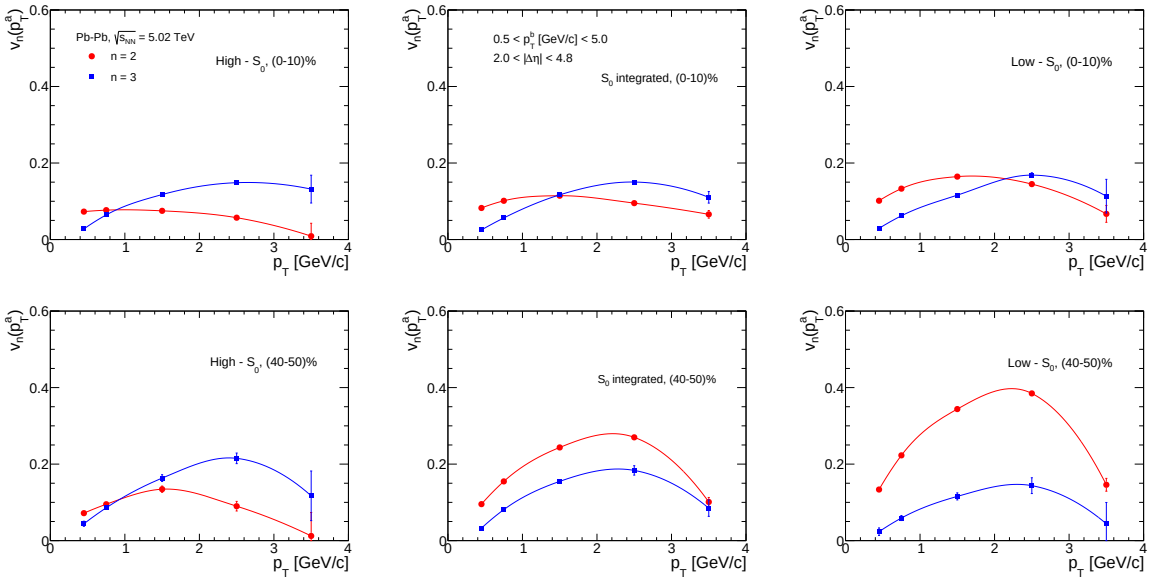

Figure 5.14: p_{T}-differential v_2 and v_3 flow for high-S_0 (left), S_0 integrated (middle) and low-S_0 (right) events in Pb–Pb collisions at $\sqrt{s_{\mathrm{NN}}}$ = 5.02 TeV for (0-10)% (top) and (40-50)% (bottom) centrality classes using AMPT [22].

high-p_{T} regions. The interplay between v_2 and v_3 as a function of p_{T} is shown in Fig. 5.14, estimated using the two-particle correlation method.

Figure 5.14 shows the centrality (upper to lower) and spherocity (left to right) dependence of p_{T}-differential v_2 and v_3 in Pb–Pb collisions at $\sqrt{s_{\mathrm{NN}}} = 5.02$ TeV using AMPT. From the figures, it is clear that v_3 starts to dominate over v_2 after a certain p_{T}, which varies when the centrality of collision is changed. Interestingly, transverse spherocity also has a role to play, where for the high-S_0 events, the crossing is earlier than that of low-S_0 events. The crossing in p_{T} between v_2 and v_3 is is denoted as $p_{\mathrm{T}}^{\mathrm{cross}}$, which quantifies the dominance of geometry versus fluctuations for a particular class of transverse spherocity and centrality. Both v_2, and v_3, shown in Fig. 5.14 are fitted with a polynomial, and corresponding $p_{\mathrm{T}}^{\mathrm{cross}}$ is extracted as a function of centrality and transverse spherocity, which is shown in Fig. 5.15. It is interesting to see that, for S_0-integrated and low-S_0 events, $p_{\mathrm{T}}^{\mathrm{cross}}$ increases with a decrease in collision centrality. In contrast, $p_{\mathrm{T}}^{\mathrm{cross}}$ remains nearly unchanged for high-S_0 events. This depicts the dominance of triangular flow in high-S_0 events irrespective of centrality class.

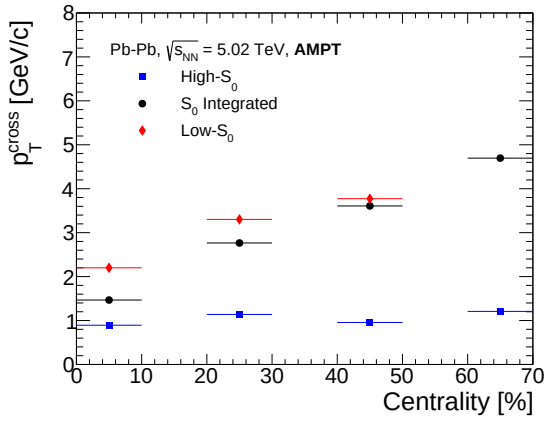

Figure 5.15: Transverse momentum value corresponding to crossing between v_2 and v_3 (p_T^{cross}) as a function of centrality for different spherocity cuts for Pb–Pb collisions at $\sqrt{s_{NN}}$ = 5.02 TeV using AMPT [22].

5.4.7 Kinetic freeze-out parameters

One of the major components of the collectivity of the system formed in heavy-ion collisions is the radial flow, which provides an additional boost to the particles produced in heavy-ion collisions. The boost is different for baryons than for mesons, and different for different masses of the particles. The particle spectra at the freeze-out retain the information of radial flow. This section explores the spherocity dependence of radial flow of the system, which is quantified by the transverse radial flow velocity extracted from the identified particle spectra, extracted by a simultaneous fit of the Boltzmann-Gibbs blastwave (BGBW) distribution [151]. Using BGBW, one can extract the transverse radial flow velocity (β_T) and kinetic freeze-out temperature (T_{kin}) of the system formed in heavy-ion collisions. The p_T-differential yield in the BGBW framework can be given as:

$$\frac{d^2N}{dp_T dy}\bigg|_{y=0} = C\ p_T\ m_T \int_0^{R_0} r\ dr\ K_1\Big(\frac{m_T\ \cosh\rho}{T_{kin}}\Big) I_0\Big(\frac{p_T\ \sinh\rho}{T_{kin}}\Big). \tag{5.35}$$

Here, $K_1\Big(\frac{m_T\ \cosh\rho}{T_{kin}}\Big)$ and $I_0\Big(\frac{p_T\ \sinh\rho}{T_{kin}}\Big)$ are modified Bessel's functions, given as follows:

$$K_1\Big(\frac{m_T\ \cosh\rho}{T_{kin}}\Big) = \int_0^{\infty} \cosh y\ \exp\Big(-\frac{m_T\ \cosh y\ \cosh\rho}{T_{kin}}\Big) dy,$$

$$I_0\Big(\frac{p_T\ \sinh\rho}{T_{kin}}\Big) = \frac{1}{2\pi}\int_0^{2\pi} \exp\Big(\frac{p_T\ \sinh\rho\ \cos\phi}{T_{kin}}\Big) d\phi,$$

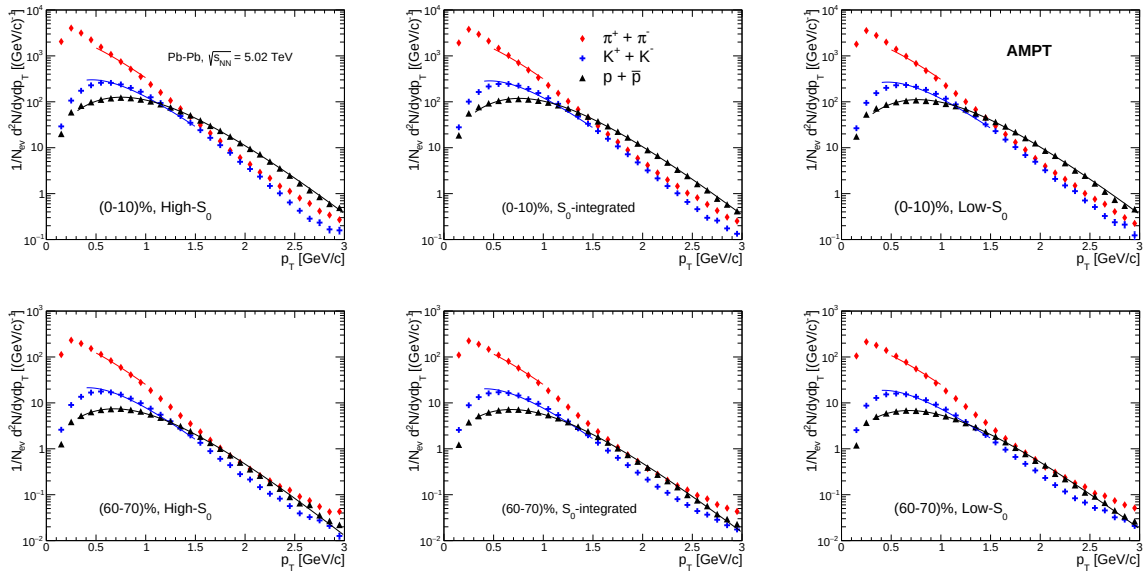

Figure 5.16: Identified particles' p_{T} spectra fitted with Boltzmann-Gibbs blastwave function for different S_0 classes, from left to right, and centrality classes in Pb-Pb collisions at $\sqrt{s_{\mathrm{NN}}} = 5.02$ TeV [105].

where $\rho = \tanh^{-1}\beta_{\mathrm{T}}$ and $\beta_{\mathrm{T}} = \beta_{\mathrm{s}}\xi^{\mathrm{n}}$ [151–153]. $\xi = (r/R_0)$, and β_{s} is the maximum surface velocity, r is the radial distance, and R_0 is the maximum radius of the system at the freeze-out. In the BGBW framework, the particles which are closer to the center are assumed to move slower than the ones at the edges. The mean transverse radial flow velocity is given by [154],

$$\langle\beta_{\mathrm{T}}\rangle = \frac{\int \beta_s \xi^n \xi \, d\xi}{\int \xi \, d\xi} = \Big(\frac{2}{2+n}\Big)\beta_s. \tag{5.36}$$

Figure 5.16 shows the simultaneous fitting of the BGBW function to the identified particles' p_{T}-spectra in different spherocity and centrality classes. The fitting ranges in p_{T} for the charged pions, kaons and protons are (0.5 - 1) GeV/c, (0.4 - 1.5) GeV/c and (0.3 - 3) GeV/c, respectively. The fitting is performed using χ^2 minimisation procedure keeping $\mathrm{T_{kin}}$, β_{s} and n as free parameters.

Figure 5.17 shows the $\mathrm{T_{kin}}$ versus $\langle\beta_{\mathrm{T}}\rangle$ for different spherocity classes in Pb-Pb collisions at $\sqrt{s_{\mathrm{NN}}} = 5.02$ TeV using AMPT. The kinetic freeze-out parameters are found to have significant dependence on S_0. The high-S_0 events, dominated by a large number of soft particles, which require more time to reach the freeze-out, possess lower T_{kin} compared to low-S_0 events. On the other hand, a dense system in high-S_0 events, increases

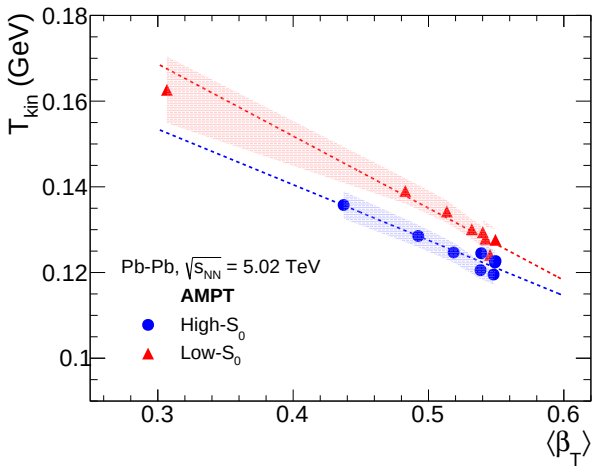

Figure 5.17: Kinetic freeze-out temperature versus transverse radial flow velocity for different S_0 classes in Pb-Pb collisions at $\sqrt{s_{\rm NN}} = 5.02$ TeV [105].

the radial boost of the particles, which is reflected in comparatively larger $\langle\beta_{\rm T}\rangle$, shown in Fig. 5.17.

5.5 Summary

In summary, this chapter explores the applicability of transverse spherocity in heavy-ion collisions, in contrast to reduced flow vectors, which are traditional choices for event-shape engineering in heavy-ion collisions. The study is performed in Pb–Pb collisions at $\sqrt{s_{\rm NN}} = 5.02$ TeV using AMPT. Multi-particle correlations and cumulant methods are used to calculate the anisotropic flow coefficients, which reduce the non-flow correlations substantially. The measurements of elliptic flow coefficients are studied as a function of transverse spherocity and compared with those of reduced flow vectors. Transverse spherocity is further used to study particle correlations, initial eccentricities, anisotropic flow coefficients and their fluctuations. With transverse spherocity, one can choose events with large elliptic flow and small elliptic flow fluctuations, and vice versa, simultaneously. This particular property of transverse spherocity is applied to remove the contribution of elliptic flow from higher-order flow coefficients, which are sensitive to medium response. It is observed that the events with smaller elliptic flow show stronger damping effects with change in centrality, which is similar to that shown in hydrodynamical calculations.

Moreover, this chapter also explores the p_{T}-differential anisotropic flow coefficients. Here, with a unique observable, $p_{\mathrm{T}}^{\mathrm{cross}}$, one can naively quantify the dominance of initial collision geometry versus geometry fluctuations. Further, the kinetic freeze-out parameters, such as the kinetic freeze-out temperature and transverse radial flow velocities, are studied as a function of transverse spherocity, where one observes a significant transverse spherocity dependence. This chapter not only emphasises the applicability of transverse spherocity but also shows some unique applications in heavy-ion collisions, which would certainly help experimentalists understand particle production and flow using event-shape engineering.

Chapter 6

Summary

In this chapter, I summarise the research works discussed in this PhD thesis which have been carried out at Indian Institute of Technology Indore, India within the ALICE collaboration at the LHC, CERN with financial support from University Grants Commission, Government of India and DAE-DST, Government of India, funding under the mega-science project "Indian participation in the ALICE experiment at CERN" bearing Project No. SR/MF/PS-02/2021-IITI(E-37123). This thesis explores the applicability of several event shape classifiers in small to large systems at the LHC energies.

This thesis explores several event shape classifiers to understand the strangeness production in pp collisions at $\sqrt{s} = 13$ TeV. The event shape classifiers are $N_{\rm mpi}$, $N_{\rm ch}^{\rm mid}$, $N_{\rm ch}^{\rm fwd}$, S_0, $S_0^{p_{\rm T}=1}$, $S_{\rm T}$, $R_{\rm T}$ and $\rho_{\rm ch}$. The study has been performed using PYTHIA8 Monash, Monash NoCR and Color Ropes tunes. Strange hadron to pion ratios as a function of these event classifiers have been studied. Moreover, self-normalised yield ratios of strange hadrons to pions as a function of self-normalised charged particle multiplicity at midrapidity based on percentiles of event shape classifiers have also been studied. Among all other tunes of PYTHIA8, Color Ropes is found to provide quantitative agreement of strangeness production observed in the ALICE experiment. The observations of strange and multi-strange hadron production as a function of different event shape classifiers in pp collisions at $\sqrt{s} = 13$ TeV using PYTHIA8 Color Ropes are summarised as follows.

- MPI plays an important role in strange and multi-strange hadron production, where the production increases with an increase in $N_{\rm mpi}$ for PYTHIA8 Color Ropes (RH + QCD based CR). Although RH is responsible for enhanced strange hadron pro-

duction, with $N_{\rm mpi}$, the number of color ropes increases, which leads to enhanced strange hadron production. The study of strange hadron production as a function of $N_{\rm mpi}$ can serve as a benchmark for other event shape classifiers.

- Event classifiers based on multiplicity, such as, $N_{\rm ch}^{\rm mid}$ and $N_{\rm ch}^{\rm fwd}$, although possesses correlation with $N_{\rm mpi}$, are prone to have contributions from hard processes. The strange hadron production as a function of $N_{\rm ch}^{\rm mid}$ and $N_{\rm ch}^{\rm fwd}$ are prone to have contributions from auto-correlation biases, which is significantly large for $N_{\rm ch}^{\rm mid}$.

- Event selection using S_0, $S_0^{p_{\rm T}=1}$, and $S_{\rm T}$ provide least coverage in terms of $\langle N_{\rm mpi}\rangle$ and $\langle \hat{p}_{\rm T}\rangle$ as compared to other event shape classifiers. Among these three, the sensitivity to $N_{\rm mpi}$ is higher for $S_0^{p_{\rm T}=1}$ and smallest for $S_{\rm T}$. Moreover, due to an explicit cut of $N_{\rm ch}^{\rm mid} \geq 10$ in their definitions, the strange hadron production is similar to that of high multiplicity events, however, the variation of strange hadron production as a function of S_0, $S_0^{p_{\rm T}=1}$, and $S_{\rm T}$ is negligibly small.

- Although event selection using $R_{\rm T}$ probes to large values of $\langle N_{\rm mpi}\rangle$, due to the requirement of $p_{\rm T}^{\rm lead} \geq 5$ GeV/c, $R_{\rm T}$ chooses events with large $\langle \hat{p}_{\rm T}\rangle$ (harder events). Moreover, the strange hadron to pion ratio and the double ratio as a function of $R_{\rm T}$ are affected by auto-correlation bias, which is stronger when the measurement is done in the transverse region.

- Event selection with $\rho_{\rm ch}$ or more specifically (1-$\rho_{\rm ch}$) possess significant correlation with $\langle N_{\rm mpi}\rangle$ while selecting events with relatively small $\langle \hat{p}_{\rm T}\rangle$. Moreover, the strange to pion ratio and their self-normalised yield as a function of (1-$\rho_{\rm ch}$) are found to be similar to that of $N_{\rm mpi}$, which are not affected by auto-correlation bias.

This study emphasised that the charged particle flattenicity is one of the best event shape classifiers available at the LHC that can be used to study the QGP-like signatures at the LHC, which include the production of strange hadrons.

Taking the above study as the motivation, this thesis explores the production of neutral strange hadrons, namely, $K_{\rm S}^0$ and $\Lambda + \bar{\Lambda}$ as a function of charged particle flattenicity in pp collisions at $\sqrt{s}$ = 13.6 TeV with ALICE. The thesis shows the first measurement of $K_{\rm S}^0$ spectra in pp collisions at $\sqrt{s}$ = 13.6 TeV. Moreover, this is the first flattenicity

measurement at the LHC Run 3, and the first ever exploration of strangeness production using flattenicity. Both, K^0_S and $\Lambda+\bar{\Lambda}$ p_T-spectra follow a multiplicity-like hierarchy when studied as a function of (1-ρ), where the events having larger (1-ρ) value have higher yield and broader p_T-spectra. The broadening of p_T-spectra is clearly visible for $\Lambda + \bar{\Lambda}$ in contrast to K^0_S. Moreover, the study of $(\Lambda + \bar{\Lambda})/2K^0_S$ shows a bump structure similar to what originates as a consequence of radial flow in heavy-ion collisions. This effect is stronger and the bump structure moves towards larger p_T-value as one moves towards the events with large (1-ρ), indicating that the radial flow-like signals become stronger towards the isotropic events. The study of p_T-differential Q_{pp} for K^0_S and $\Lambda+\bar{\Lambda}$ in different flattenicity classes has also been performed, which suggest that event selection based on (1-ρ) is not affected by auto-correlation biases.

Having explored the application and importance of event shape engineering in small systems, it is equally important to make similar studies in heavy-ion collisions, which would enable the scientific community to compare the effects of system dependence. Moreover, the traditional event classifiers that are used in heavy-ion collisions, such as the reduced flow vectors, are not efficient towards peripheral collisions where the multiplicity is small. We study the collective features, such as radial flow and anisotropic flow in Pb-Pb collisions at $\sqrt{s_{NN}} = 5.02$ TeV using AMPT. Transverse spherocity has been used as an event shape classifier to study the collective effects in heavy-ion collisions. The findings are summarised as follows.

- S_0 shows strong anti-correlation with q_2 and small positive correlation with q_3. Moreover, the study of v_2 as a function of S_0 and q_2 suggests that S_0 shows a broader v_2 coverage as compared to q_2, which emphasises the use of S_0 over q_2 for the studies related to v_2.

- $\langle\epsilon_2\rangle$ and v_2 show anti-correlation with S_0 while $\langle\epsilon_3\rangle$ has no dependence on S_0. A finite positive correlation between v_3 and S_0 is observed, which is attributed to the anti-correlation between v_2 and v_3 observed in experiments.

- Studies of S_0 dependence of v_4 and v_5 shows a anti-correlation behaviour, i.e., both v_4 and v_5 are smaller for high-S_0 events and vice versa. This is expected because of the strong nonlinear contribution of v_2 in the measured values of v_4 and v_5.

- $F(v_2)$ is smaller for mid-central and low-S_0 events, which increases towards the central and peripheral collisions. These effects are observed to have arisen from centrality and S_0 dependence of $F(\epsilon_2)$.

- Studies of $v_2\{2\}/\sqrt{\langle\epsilon_2^2\rangle}$ as a function of S_0 shows that the system response to the transformation of ϵ_2 to v_2 is different for events where the geometry dominates than the events dominated by v_2-fluctuations.

- Studies of $v_2\{n\}/\sqrt{\langle\epsilon_n^2\rangle}$ for $n \geq 4$ show that the isotropic events, where the contribution of v_2 is small, show a stronger damping effect with change in centrality. Low-S_0 events show a saturation behaviour in (0-30)% centrality, which is attributed to the competing effects from damping, which increases towards mid-central collisions, and nonlinear contribution from v_2, which increases towards mid-central collisions.

- The study of kinetic freeze-out parameters as a function of transverse spherocity suggests that the high-S_0 events, where particle density is larger, possess larger average radial flow velocity and smaller kinetic freeze-out temperature as compared to low-S_0 events.

From this study, it is clear that transverse spherocity is an event shape classifier that can be used in both pp and heavy-ion collisions. This is specifically important for O-O, Ne-Ne and p-O collisions at the LHC, which would provide important information on the onset of collective dynamics in small systems. The event-shape engineering methods discussed in this thesis would also be useful in studying other signatures of QGP in order to probe their microscopic origin while exploring multihadron production dynamics in ultra-relativistic hadronic and nuclear collisions.

References

[1] E. D. Bloom et al., Phys. Rev. Lett. **23**, 930 (1969).

[2] M. Breidenbach, J. I. Friedman, H. W. Kendall, E. D. Bloom, D. H. Coward, H. C. DeStaebler, J. Drees, L. W. Mo, and R. E. Taylor, Phys. Rev. Lett. **23**, 935 (1969).

[3] S. Godfrey and N. Isgur, Phys. Rev. D **32**, 189 (1985).

[4] J. Greensite, Lect. Notes Phys. **821**, 1 (2011).

[5] D. H. Perkins (Cambridge University Press, 2000), ISBN: 0-521-62196-8.

[6] Nobel Prize in Physics 2004, [Online; accessed 01-May-2025], https://www.nobelprize.org/prizes/physics/2004/summary/.

[7] A. Deur, S. J. Brodsky, and G. F. de Teramond, Nucl. Phys. **90**, 1 (2016).

[8] S. Acharya et al. (ALICE), Eur. Phys. J. C **84**, 813 (2024).

[9] S. Borsanyi, Z. Fodor, J. N. Guenther, R. Kara, S. D. Katz, P. Parotto, A. Pasztor, C. Ratti, and K. K. Szabo, Phys. Rev. Lett. **125**, 052001 (2020).

[10] A. Andronic, P. Braun-Munzinger, and J. Stachel, Nucl. Phys. A **772**, 167 (2006).

[11] J. Cleymans, H. Oeschler, K. Redlich, and S. Wheaton, Phys. Rev. C **73**, 034905 (2006).

[12] A. Andronic, P. Braun-Munzinger, K. Redlich, and J. Stachel, Nature **561**, 321 (2018).

[13] B. Andersson, G. Gustafson, and B. Soderberg, Z. Phys. C **20**, 317 (1983).

[14] Z.-w. Lin and C. M. Ko, Phys. Rev. C **65**, 034904 (2002).

[15] J. Letessier and J. Rafelski, Cambridge Monographs on Particle Physics, Nuclear Physics and Cosmology (Cambridge University Press, 2002), ISBN: 9780511534997, 10.1017/CBO9780511534997.

[16] R. Sahoo, (2016) arXiv:1604.02651 [nucl-ex].

[17] R. Sahoo (Springer Cham, 2025), ISBN: 978-3-032-09510-7.

[18] A. Kisiel, Phys. Rev. C **84**, 044913 (2011).

[19] A. Menon Kavumpadikkal Radhakrishnan, S. Prasad, S. Tripathy, N. Mallick, and R. Sahoo, Eur. Phys. J. Plus **140**, 110 (2025).

[20] S. Acharya et al. (ALICE), Phys. Rev. C **101**, 044907 (2020).

[21] H. Petersen, G.-Y. Qin, S. A. Bass, and B. Muller, Phys. Rev. C **82**, 041901 (2010).

[22] S. Prasad, N. Mallick, S. Tripathy, and R. Sahoo, Phys. Rev. D **107**, 074011 (2023).

[23] S. Voloshin and Y. Zhang, Z. Phys. C **70**, 665 (1996).

[24] J. Adam et al. (ALICE), Phys. Rev. Lett. **116**, 132302 (2016).

[25] J. Rafelski and B. Muller, Phys. Rev. Lett. **48**, 1066 (1982).

[26] P. Koch, B. Muller, and J. Rafelski, Phys. Rept. **142**, 167 (1986).

[27] J. Rafelski, Phys. Lett. B **262**, 333 (1991).

[28] S. Acharya et al. (ALICE), Eur. Phys. J. C **80**, 693 (2020).

[29] B. B. Abelev et al. (ALICE), Phys. Lett. B **728**, 25 (2014).

[30] B. B. Abelev et al. (ALICE), Phys. Lett. B **726**, 164 (2013).

[31] V. Khachatryan et al. (CMS), Phys. Rev. Lett. **116**, 172302 (2016).

[32] S. Acharya et al. (ALICE), (2024) arXiv:2411.09323 [nucl-ex].

[33] S. Acharya et al. (ALICE), JHEP **05**, 184 (2024).

[34] E. Cuautle, R. Jimenez, I. Maldonado, A. Ortiz, G. Paic, and E. Perez, (2014) arXiv:1404.2372 [hep-ph].

[35] B. Abelev et al. (ALICE), Eur. Phys. J. C **72**, 2124 (2012).

[36] G. Hanson et al., Phys. Rev. Lett. **35**, 1609 (1975).

[37] T. Martin, P. Skands, and S. Farrington, Eur. Phys. J. C **76**, 299 (2016).

[38] G. Bencedi, A. Ortiz, and A. Paz, Phys. Rev. D **104**, 016017 (2021).

[39] P. Palni, A. Khuntia, and P. Bartalini, Eur. Phys. J. C **80**, 919 (2020).

[40] A. Ortiz and G. Paic, Rev. Mex. Fis. Suppl. **3**, 040911 (2022).

[41] S. Acharya et al. (ALICE), Phys. Rev. D **111**, 012010 (2025).

[42] A. Ortiz, A. Khuntia, O. Vázquez-Rueda, S. Tripathy, G. Bencedi, S. Prasad, and F. Fan, Phys. Rev. D **107**, 076012 (2023).

[43] S. Acharya et al. (ALICE), Phys. Lett. B **843**, 137649 (2023).

[44] S. Acharya et al. (ALICE), JHEP **05**, 229 (2024).

[45] B. B. Abelev et al. (ALICE), Phys. Lett. B **728**, [Erratum: Phys.Lett.B 734, 409 (2014)], 216 (2014).

[46] J. Adam et al. (ALICE), Nature Phys. **13**, 535 (2017).

[47] V. Khachatryan et al. (CMS), JHEP **09**, 091 (2010).

[48] V. Khachatryan et al. (CMS), Phys. Lett. B **765**, 193 (2017).

[49] S. Chatrchyan et al. (CMS), Eur. Phys. J. C **72**, 2164 (2012).

[50] J. L. Nagle and W. A. Zajc, Ann. Rev. Nucl. Part. Sci. **68**, 211 (2018).

[51] T. Sjöstrand, S. Ask, J. R. Christiansen, R. Corke, N. Desai, P. Ilten, S. Mrenna, S. Prestel, C. O. Rasmussen, and P. Z. Skands, Comput. Phys. Commun. **191**, 159 (2015).

[52] A. Ortiz Velasquez, P. Christiansen, E. Cuautle Flores, I. Maldonado Cervantes, and G. Paić, Phys. Rev. Lett. **111**, 042001 (2013).

[53] C. Bierlich, G. Gustafson, L. Lönnblad, and A. Tarasov, JHEP **03**, 148 (2015).

[54] C. Bierlich, G. Gustafson, and L. Lönnblad, (2016) arXiv:1612.05132 [hep-ph].

[55] T. Sjostrand, S. Mrenna, and P. Z. Skands, Comput. Phys. Commun. **178**, 852 (2008).

[56] PYTHIA 8, [Online; accessed 31-May-2025], https://pythia.org//latest-manual/Welcome.html.

[57] S. Prasad, B. Sahoo, S. Tripathy, N. Mallick, and R. Sahoo, Phys. Rev. C **111**, 044902 (2025).

[58] S. Prasad, S. Tripathy, B. Sahoo, and R. Sahoo, (2025) arXiv:2506.03782 [hep-ph].

[59] P. Christiansen and P. Van Mechelen, Annu. Rev. Nucl. Part. Sci. **75**, 327 (2025).

[60] B. Andersson, G. Gustafson, G. Ingelman, and T. Sjostrand, Phys. Rept. **97**, 31 (1983).

[61] S. Argyropoulos and T. Sjöstrand, JHEP **11**, 043 (2014).

[62] ATLAS, (2017) http://cds.cern.ch/record/2262253.

[63] P. Skands, S. Carrazza, and J. Rojo, Eur. Phys. J. C **74**, 3024 (2014).

[64] J. Adam et al. (ALICE), Phys. Lett. B **753**, 319 (2016).

[65] S. Prasad, N. Mallick, and R. Sahoo, Phys. Rev. D **109**, 014005 (2024).

[66] S. Acharya et al. (ALICE), Phys. Lett. B **810**, 135758 (2020).

[67] J. Schukraft (ALICE), J. Phys. G **38**, 124003 (2011).

[68] LHC, [Online; accessed 09-July-2025], 2024, http://cds.cern.ch/record/782076.

[69] CERN, [Online; accessed 09-July-2025], https://cds.cern.ch/record/2197559.

[70] S. Acharya et al. (ALICE), JINST **19**, P05062 (2024).

[71] L. Musa, [Online; accessed 10-July-2025], https://cds.cern.ch/record/1475244.

[72] ALICE Collaboration, [Online; accessed 10-July-2025], https://cds.cern.ch/record/1622286.

[73] A. Andronic (ALICE TRD), Nucl. Instrum. Meth. A **522**, 40 (2004).

[74] ALICE Collaboration, [Online; accessed 10-July-2025], https://cds.cern.ch/record/430132.

[75] ALICE Collaboration, [Online; accessed 10-July-2025], https://cds.cern.ch/record/381431.

[76] ALICE Collaboration, [Online; accessed 10-July-2025], https://edms.cern.ch/document/398934/1.

[77] ALICE Collaboration, [Online; accessed 10-July-2025], https://cds.cern.ch/record/932676.

[78] A. Fernández et al. (ACORDE), Nucl. Instrum. Meth. A **572**, 102 (2007).

[79] A. Maevskaya (ALICE), Phys. Atom. Nucl. **84**, 579 (2021).

[80] K. Aamodt et al. (ALICE), JINST **3**, S08002 (2008).

[81] A. Isakov (ALICE), JINST **20**, C07026 (2025).

[82] A. S. Triolo (ALICE), JINST **20**, C01030 (2025).

[83] F. Sauli, Nucl. Instrum. Meth. A **386**, 531 (1997).

[84] L. Rolandi, W. Riegler, and W. Blum, Particle Acceleration and Detection (Springer, 2008), ISBN: 978-3-540-76683-4, 978-3-642-09538-2, 978-3-540-76684-1, 10.1007/978-3-540-76684-1.

[85] H. K. Koley (ALICE), PoS **ICHEP2024**, 639 (2025).

[86] CERN, [Online; accessed 11-July-2025], https://root.cern.ch/.

[87] ALICE, [Online; accessed 11-July-2025], https://github.com/AliceO2Group/AliceO2.

[88] A. Ortiz, A. Paz, J. D. Romo, S. Tripathy, E. A. Zepeda, and I. Bautista, Phys. Rev. D **102**, 076014 (2020).

[89] S. Prasad and R. Sahoo, Analysis Note ID number: ANA-1609 (ALICE Internal), https://alice-notes.web.cern.ch/node/1609.

[90] S. Navas et al. (Particle Data Group), Phys. Rev. D **110**, 030001 (2024).

[91] M. Sharma (ALICE), Springer Proc. Phys. **261**, 1019 (2021).

[92] ALICE, [Online; accessed 01-May-2025], https://aliceo2group.github.io/analysis-framework/docs/gettingstarted/.

[93] S. Prasad and R. Sahoo, Poster Presented in Quark Matter 2025 Conference, https://indico.cern.ch/event/1334113/contributions/6291974/.

[94] R. L. Workman et al. (Particle Data Group), PTEP **2022**, 083C01 (2022).

[95] O. Matonoha, Thesis (2023-05-22, Lund University, Lund U., 2023).

[96] F. Costa, A. Kluge, and P. Vande Vyvre (ALICE), J. Phys. Conf. Ser. **898**, 032011 (2017).

[97] S. Acharya et al. (ALICE), Eur. Phys. J. C **80**, 167 (2020).

[98] C. Adler et al. (STAR), Phys. Rev. C **66**, 034904 (2002).

[99] J. Schukraft, A. Timmins, and S. A. Voloshin, Phys. Lett. B **719**, 394 (2013).

[100] G. Aad et al. (ATLAS), Phys. Rev. C **92**, 034903 (2015).

[101] A. Banfi, G. P. Salam, and G. Zanderighi, JHEP **06**, 038 (2010).

[102] E. Farhi, Phys. Rev. Lett. **39**, 1587 (1977).

[103] S. Acharya et al. (ALICE), Eur. Phys. J. C **79**, 857 (2019).

[104] N. Mallick, S. Tripathy, and R. Sahoo, Eur. Phys. J. C **82**, 524 (2022).

[105] S. Prasad, N. Mallick, D. Behera, R. Sahoo, and S. Tripathy, Sci. Rep. **12**, 3917 (2022).

[106] N. Mallick, R. Sahoo, S. Tripathy, and A. Ortiz, J. Phys. G **48**, 045104 (2021).

[107] S. Tripathy, S. Prasad, and R. Sahoo, (2025) arXiv:2504.09275 [nucl-ex].

[108] S. Prasad, A. M. Kavumpadikkal Radhakrishnan, R. Sahoo, and N. Mallick, Phys. Lett. B **868**, 139753 (2025).

[109] D. Teaney and L. Yan, Phys. Rev. C **90**, 024902 (2014).

[110] F. G. Gardim, F. Grassi, M. Luzum, and J.-Y. Ollitrault, Phys. Rev. C **85**, 024908 (2012).

[111] G. Aad et al. (ATLAS), Phys. Rev. C **90**, 024905 (2014).

[112] S. Acharya et al. (ALICE), Phys. Rev. C **111**, 064913 (2025).

[113] B. Zhang, C. M. Ko, B.-A. Li, and Z.-w. Lin, Phys. Rev. C **61**, 067901 (2000).

[114] Z.-W. Lin, C. M. Ko, B.-A. Li, B. Zhang, and S. Pal, Phys. Rev. C **72**, 064901 (2005).

[115] X.-N. Wang and M. Gyulassy, Phys. Rev. D **44**, 3501 (1991).

[116] D. d'Enterria and C. Loizides, Ann. Rev. Nucl. Part. Sci. **71**, 315 (2021).

[117] B. Zhang, Comput. Phys. Commun. **109**, 193 (1998).

[118] V. Greco, C. M. Ko, and P. Levai, Phys. Rev. Lett. **90**, 202302 (2003).

[119] B.-A. Li and C. M. Ko, Phys. Rev. C **52**, 2037 (1995).

[120] B. Li, A. T. Sustich, B. Zhang, and C. M. Ko, Int. J. Mod. Phys. E **10**, 267 (2001).

[121] B. B. Abelev et al. (ALICE), JHEP **06**, 190 (2015).

[122] N. Mallick, S. Prasad, A. N. Mishra, R. Sahoo, and G. G. Barnaföldi, Phys. Rev. D **107**, 094001 (2023).

[123] N. Mallick, S. Prasad, A. N. Mishra, R. Sahoo, and G. G. Barnaföldi, Phys. Rev. D **105**, 114022 (2022).

[124] A. Adare et al. (PHENIX), Phys. Rev. C **78**, 014901 (2008).

[125] G. Aad et al. (ATLAS), Phys. Rev. C **86**, 014907 (2012).

[126] G. Aad et al. (ATLAS), Phys. Rev. C **101**, 024906 (2020).

[127] A. Bilandzic, R. Snellings, and S. Voloshin, Phys. Rev. C **83**, 044913 (2011).

[128] A. Bilandzic, C. H. Christensen, K. Gulbrandsen, A. Hansen, and Y. Zhou, Phys. Rev. C **89**, 064904 (2014).

[129] A. Bilandzic, PhD thesis (Utrecht University, 2012).

[130] K. Aamodt et al. (ALICE), Phys. Rev. Lett. **107**, 032301 (2011).

[131] K. Aamodt et al. (ALICE), Phys. Rev. Lett. **105**, 252302 (2010).

[132] Y. Zhou (ALICE), Nucl. Phys. A **931**, 949 (2014).

[133] Y. Zhou, X. Zhu, P. Li, and H. Song, Phys. Rev. C **91**, 064908 (2015).

[134] B. B. Abelev et al. (ALICE), Phys. Rev. C **90**, 054901 (2014).

[135] J. Jia, M. Zhou, and A. Trzupek, Phys. Rev. C **96**, 034906 (2017).

[136] M. Aaboud et al. (ATLAS), Phys. Rev. C **97**, 024904 (2018).

[137] M. Aaboud et al. (ATLAS), Eur. Phys. J. C **77**, 428 (2017).

[138] A. Adare et al. (PHENIX), Phys. Rev. C **99**, 024903 (2019).

[139] J.-Y. Ollitrault, A. M. Poskanzer, and S. A. Voloshin, Phys. Rev. C **80**, 014904 (2009).

[140] B. Alver and G. Roland, Phys. Rev. C **81**, [Erratum: Phys.Rev.C 82, 039903 (2010)], 054905 (2010).

[141] P. Filip, R. Lednicky, H. Masui, and N. Xu, Phys. Rev. C **80**, 054903 (2009).

[142] L. Ma, G. L. Ma, and Y. G. Ma, Phys. Rev. C **94**, 044915 (2016).

[143] S. Prasad, N. Mallick, S. Tripathy, and R. Sahoo, Springer Proc. Phys. **304**, 731 (2024).

[144] M. Aaboud et al. (ATLAS), JHEP **01**, 051 (2020).

[145] G. Aad et al. (ATLAS), JHEP **11**, 183 (2013).

[146] G. Aad et al. (ATLAS), Eur. Phys. J. C **74**, 3157 (2014).

[147] S. Chatrchyan et al. (CMS), Phys. Rev. C **89**, 044906 (2014).

[148] D. Teaney and L. Yan, Phys. Rev. C **83**, 064904 (2011).

[149] B. H. Alver, C. Gombeaud, M. Luzum, and J.-Y. Ollitrault, Phys. Rev. C **82**, 034913 (2010).

[150] B. Schenke, S. Jeon, and C. Gale, Phys. Rev. C **85**, 024901 (2012).

[151] E. Schnedermann, J. Sollfrank, and U. W. Heinz, Phys. Rev. C **48**, 2462 (1993).

[152] P. Braun-Munzinger, J. Stachel, J. P. Wessels, and N. Xu, Phys. Lett. B **344**, 43 (1995).

[153] Z. Tang, L. Yi, L. Ruan, M. Shao, H. Chen, C. Li, B. Mohanty, P. Sorensen, A. Tang, and Z. Xu, Chin. Phys. Lett. **30**, 031201 (2013).

[154] K. Adcox et al. (PHENIX), Phys. Rev. C **69**, 024904 (2004).